Research Activities

– Synchrotron Radiation Experiments –

Oxygen Isotope Effects on Sr$_2$RuO$_4$
Studied by High-resolution ARPES

H. Iwasawa[a], Y. Yoshida[b], K. Shimada[a], Y. Aiura[b]

^{a}*Hiroshima Synchrotron Radiation Center, Hiroshima University, Higashi-Hiroshima 739-0046, Japan*
^{b}*National Institute of Advanced Industrial Science and Technology, Tsukuba, Ibaraki 305-8568, Japan*

Single layered ruthenium oxide (ruthenate), Sr$_2$RuO$_4$, is well-known as a representative spin-triplet superconductor with T_c~1.5 K, the pairing mechanism remains unresolved [1, 2]. One of the effective approaches for seeking pairing interaction is to clarify what kinds of interactions are coupling to the electronic states. Previous our ARPES results revealed that a band renormalization or kink in the dispersion is most significant for the γ band derived from two-dimensional Ru $4d_{xy}$ orbital compared with the α and β bands derived from one-dimensional Ru $4d_{zx,yz}$ orbitals [3]. We also found the multiple electron-phonon interactions via kinks in the γ band at around 40, 60, and 80 meV [4]. Besides to phononic interactions, magnetic fluctuations at lower energy less than 10 meV were reported by inelastic neutron scattering experiments [5, 6], though their signature was not observed by ARPES so far. In this work, we have performed high-resolution ARPES on Sr$_2$RuO$_4$, and further, examined oxygen isotope effects on low-energy electronic structures.

High-quality single crystals of Sr$_2$RuO$_4$ were prepared by the floating zone method with a self-flux technique (T_c ~ 1.36 K). Oxygen isotope substitution was performed by annealing, and the oxygen isotope substitution rates were higher than 80% estimated via Raman spectroscopy. ARPES experiments were measured at the linear undulator beamline (BL-1) of Hiroshima Synchrotron Radiation Center (HiSOR) using a Scienta R4000 electron analyzer. Clean and flat surfaces of the samples were obtained by cleaving *in situ* under ultra-high-vacuum conditions (4×10^{-11} Torr) at a low temperature (~12 K). Present ARPES data were taken with the photon energy of 48 eV at 12 K in the *s*-polarization geometry after aging the sample surface to eliminate the surface states [7, 8].

Figures 1(a) and (b) show the ARPES images of Sr$_2$RuO$_4$ for ^{16}O and ^{18}O samples, respectively, taken along the ΓM line as indicated by the red line in Fig. (d). In the *s*-polarization geometry, the γ band derived from Ru $4d_{xy}$ orbital can be dominantly observed. This enables us to accurately determine the band dispersions by fitting the momentum distribution curves (MDCs). Figure 1(c) compares the ^{16}O (blue) and ^{18}O (red) energy-momentum dispersions, where one can see small but finite isotope effects near the Fermi level below 20 meV, while they become almost negligible in the higher energy region. As clearly seen, the ^{18}O sample shows the larger effective mass near the Fermi level, which yields a high density of states in the van Hove singularity near the M point. This is consistent with the reported negative oxygen isotope effect on T_c ($^{18}T_c > {}^{16}T_c$) [9]. Although the reason why the low-energy coupling is enhanced due to the oxygen isotope substitution is unsure, present results clearly indicate that the phonons should play an important role in the very low-lying electronic states of Sr$_2$RuO$_4$.

REFERENCES

1.   A. P. Mackenzie and Y. Maeno, Rev. Mod. Phys. **75**, 657 (2003).
2.   Y. Maeno *et al*. J. Phys. Soc. Jpn. **81**, 011009 (2012).
3.   H. Iwasawa *et al.*, Phys. Rev. B **72**, 104514 (2005).
4.   H. Iwasawa *et al.*, Phys. Rev. Lett. **105**, 226406 (2010).
5.   M. Braden *et al.*, Phys. Rev. B **57**, 1236 (1998).
6.   M. Braden *et al.*, Phys. Rev. B **66**, 064522 (2002).
7.   R. Matzdorf *et al.*, Science **289**, 746 (2000).
8.   K. M. Shen *et al.*, Phys. Rev. B **64**, 180502(R) (2001).
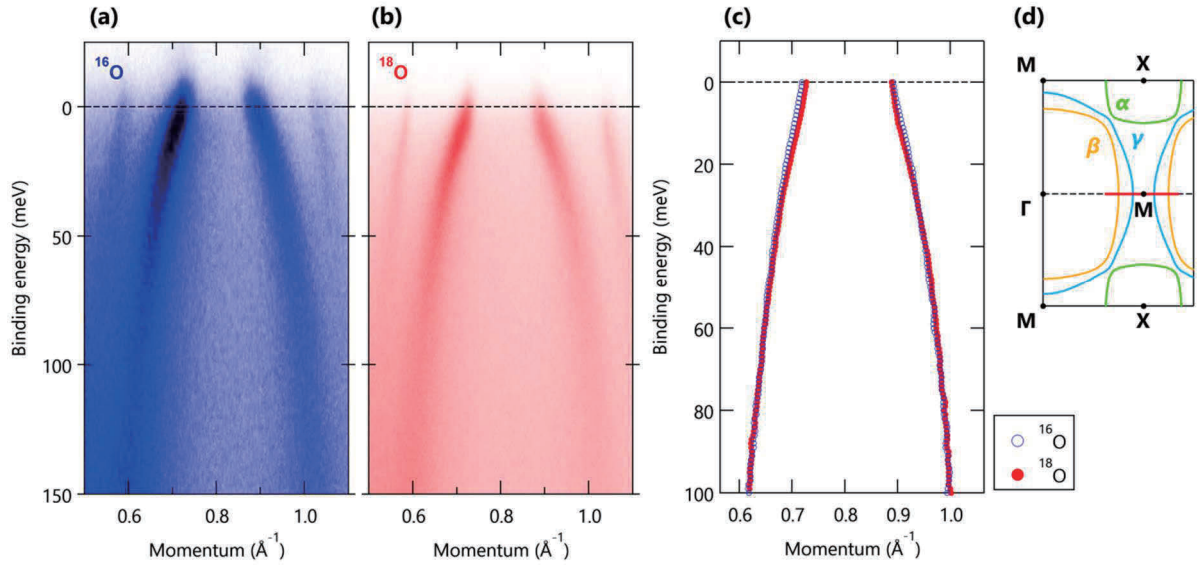9.   Z. Q. Mao *et al.,* Phys. Rev. B **63**, 144514 (2001).

FIGURE 1. (a), (b) ARPES images along the ΓM line for ^{16}O and ^{18}O from Sr_2RuO_4 taken with 48 eV at 12 K in the s-polarization geometry. (c) Energy-momentum dispersion derived from momentum distribution curves (MDCs) for ^{16}O and ^{18}O samples. (d) Schematic Fermi surface of Sr_2RuO_4.

Angle-resolved Photoelectron Spectroscopy Study of Ce(Ru$_{1-x}$Rh$_x$)$_2$Al$_{10}$ II

H. Yamaoka[a], E. F. Schwier[b], Y. Yamamoto[c], F. Tajima[d],
R. Onodera[d], T. Nishioka[d], K. Shimada[b], and J. Mizuki[c],

[a]*RIKEN SPring-8 Center, Sayo, Hyogo 679-5148, Japan*
[c]*Hiroshima Synchrotron Radiation Center, Hiroshima University, Higashi-Hiroshima, Hiroshima 739-0046, Japan*
[b]*Graduate School of Science and Technology, Kwansei Gakuin University, Sanda, Hyogo 669-1337, Japan*
[d]*Graduate School of Science, Kochi University, 2-5-1 Akebono, Kochi 780-8520, Japan*

Ternary intermetallic compounds of CeM_2Al$_{10}$ (M = Ru, Os, Fe) have attracted a lot of interest because of their unusual physical properties [1,2]. In this system Ce atoms are surrounded by Al atoms forming a cage-like structure. Magnetic transition temperatures of the antiferromagnetic state of rare earth compounds can be scaled by the de Gennes factor. The Neel temperatures (T_N) of CeRu$_2$Al$_{10}$ is estimated to be 0.19 K using the measured value of T_N = 16.5 K of GdRu$_2$Al$_{10}$. Most Ce compounds have the Ce-Ce distance more than 5 Å and the magnetic ordering temperature is below 2 K. The shortest Ce-Ce distance is 5.26 Å in CeRu$_2$Al$_{10}$. In CeM_2Al$_{10}$, nevertheless, antiferromagnetic (AFM) order occurs at anomalously high temperature of T_0 = 27.3 K for M = Ru and 28.7 K for M = Os, whereas the AFM order is not observed for M = Fe. The AFM moment below T_0 is 0.42μ_B/Ce for M = Ru and 0.29μ_B/Ce for M = Os. It was suggested that the small magnetic moment was explained by considering the crystal field effect (CEF) level scheme. Anisotropic exchange interaction was considered to reproduce the AFM ordering temperature. However, the magnetic behavior at $T < T_0$ has not yet explained well within the mean-field approximation even taking into account the CEF effect. This deviation of the magnetic moment at $T < T_0$ was attributed to the anisotropic enhancement of the *c-f* hybridization. Paramagnetic susceptibility exhibits large anisotropy in CeMAl$_{10}$, $\chi_a > \chi_c > \chi_b$ at $T > T_0$, where χ_i is the susceptibility along *i*-axis. However, at $T < T_0$ the AFM order occurs along the *c*-axis, not along the easy *a*-axis. Kondo *et al*. suggested that a larger *c-f* hybridization along the *a*-axis could make a magnetization easy axis along the *c*-axis [3]. X-ray diffraction (XRD) study also suggested the importance of the *c-f* hybridization along the *a*-axis [4]. In CeMAl$_{10}$ a detailed study of the complex electronic structure, especially the anisotropy of the hybridization strength, has not been performed yet. By substituting Ru with Rh in Ce(Ru$_{1-x}$Rh$_x$)$_2$Al$_{10}$, the axis of magnetization is flipped from *c*-axis to the *a*-axis between x = 0.03 and x = 0.05 and the magnetic moment increases to 0.8μ_B/Ce. This makes the Rh substitution an ideal method to study the *c-f* hybridization anisotropy.

In our previous experiments the electronic structures of Ce(Ru$_{1-x}$Rh$_x$)$_2$Al$_{10}$ and Ce(Ru$_{1-x}$Fe$_x$)$_2$Al$_{10}$ have been studied by x-ray emission spectroscopy (XES) [5] and photoelectron spectroscopy (PES) as a function of *x*. X-ray diffraction of Ce(Ru$_{1-x}$Rh$_x$)$_2$Al$_{10}$ was also performed. No *x* dependence of the lattice constant were observed up to x = 0.1 in Ce(Ru$_{1-x}$Rh$_x$)$_2$Al$_{10}$. While XES showed a Ce valence transition between x = 0.03 and 0.05. High-resolution PES indicated the increase of the density of state near the Fermi level in the x = 0.05 sample.

In this study, angle-resolved PES was successfully performed for the x = 0.00 and 0.05 samples of Ce(Ru$_{1-x}$Rh$_x$)$_2$Al$_{10}$. We found an anisotropy of the hybridization strength, i.e. the f^1/f^0 ratio, between the ΓA and ΓC directions using the Ce 4*d*-4*f* resonance photoemission spectroscopy taken at $h\nu \sim$ 122 eV. For x = 0.00 the *c-f* hybridization was increased along the ΓA direction compared to the ΓC direction as proposed by Kondo *et al*. (Figure 1a). For x = 0.05 in Ce(Ru$_{1-x}$Rh$_x$)$_2$Al$_{10}$, on the other hand, the situation was reversed and *c-f* hybridization was increased along the ΓA direction over the ΓC direction (Fig. 1(b)). This gives further evidence to the explanation that the *c-f* hybridization anisotropy may drive the axis of magnetization.

To further elucidate the anisotropy of the electronic structure we employed Density Functional Theory (DFT) [6]. Electron localization of the Ce *f*-states was simulated using a Yukawa screening length of 5 a$_B$ which gave a Hubbard *U* equivalent of 1.1 eV and J = 0.4 eV. The magnetic moment was fixed in an AFM state with its direction parallel and antiparallel to the *c*-axis, but its magnitude was free and determined to be 0.49μ_B/Ce atom, which is slightly higher than the experimental value. In Fig. 2(a) we show the bare band structure close to the Fermi energy in the relevant region for the *c-f* hybridization. Already, the anisotropy of the bands can be seen between the ΓA and ΓC high symmetry lines. To further highlight the momentum dependent hybridization we
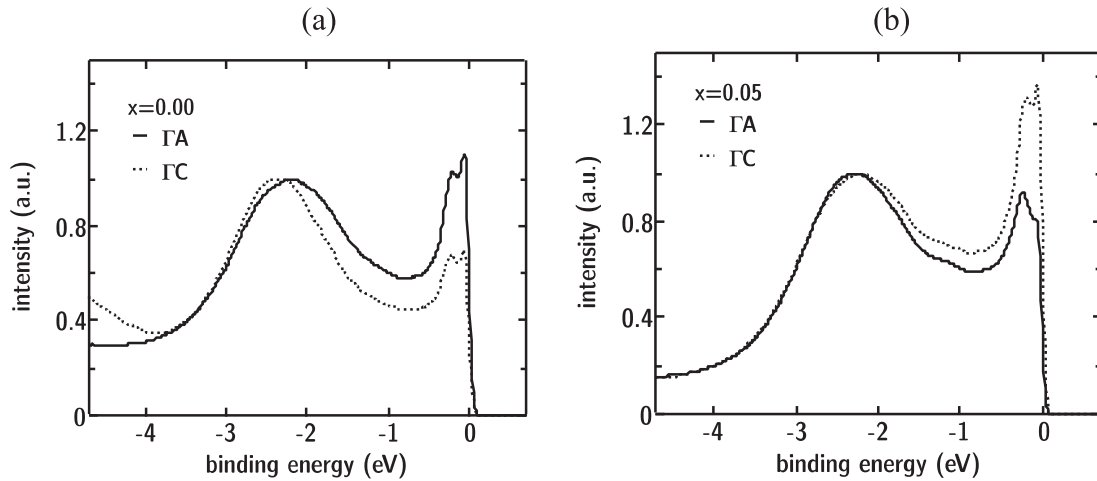
FIGURE 1. Photoemission spectra at Ce d-f resonance at $h\nu = 122$ eV integrated along the ΓA and ΓC high symmetry directions and normalized to the f^0 peak height. (a) Measurement for CeRu$_2$Al$_{10}$ (b) Measurement for Ce(Ru$_{1-x}$Rh$_x$)$_2$Al$_{10}$ ($x=$ 0.05).

have plotted the d- (Fig. 2(b)) and f-orbital weights (Fig. 2(c)). Near the A point, there exist energy bands above and below the Fermi level having both d- and f-weights. Along the ΓC direction, on the other hand, all the bands cross the Fermi level, and f-derived flat bands exist just above the Fermi level near the C point. The differences in the bare band structure (namely the absence of occupied bands at C) could be related to the experimental momentum anisotropy of the f^0/f^1 intensity ratio. However, more accurate theoretical description using a periodic Anderson model is required for the detailed comparison with the ARPES results.
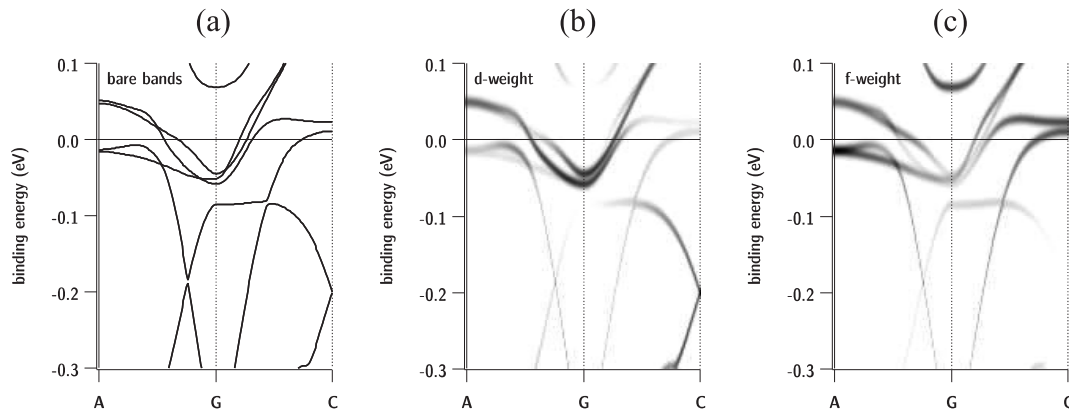

FIGURE 2. Electronic bands close to the Fermi level calculated using LDA + λ method. (a) Bare bands along the AΓC high symmetry path. (b) d-orbital weight (c) f-orbital weight.

References

1. V. M. T. Thiede, T. Ebel, and W. Jeitschko, *J. Mater. Chem.* **8**, 125 (1998).
2. T. Nishioka, Y. Kawamura, T. Takesaka, R. Kobayashi, H. Kato, M. Matsumura, K. Kodama, K. Matsubayashi, and Y. Uwatoko, *J. Phys. Soc. Jpn.* **78**, 123705 (2009).
3. A. Kondo, J. Wang, K. Kindo, Y. Oogane, Y. Kawamura, S. Tanimoto, T. Nishioka, D. Tanaka, H. Taida, and M. Sera, Phys. Rev. B **83**, 180415 (2011).
4. M. Sera, D. Tanaka, H. Tanida, C. Moriyoshi, M. Ogawa, Y. Kuroiwa, T. Nishioka, M. Matsumura, J. Kim, N. Tsuji, and M. Takata, J. Phys. Soc. Jpn. **82**, 024603 (2013).
5. Y. Zekko, Y. Yamamoto, H. Yamaoka, F. Tajima, T. Nishioka, F. Strigari, A. Severing, J.-F. Lin, N. Hiraoka, H. Ishii, K.-D. Tsuei, and J. Mizuki, Phys. Rev. B **89**, 125108 (2014).
6. *elk* version 4.0.16 (http://elk.sourceforge.net)

Helical Structure Observed in the Photoelectron Emission Angular Distribution from the Dirac Cone of the Single-layer Graphene

Shin-ichiro Tanaka[a]

[a] *The institute of Scientific and Industrial Research, Osaka University*

The Dirac cone of the graphene is provided by the π-band whose wavefunction near the K-point of the Brillouin zone can be expressed as $\Phi = N \exp(iq \cdot r) \begin{pmatrix} \exp(-i\frac{\phi}{2}) \\ \exp(+i\frac{\phi}{2}) \end{pmatrix} (\psi_A \quad \psi_B)$, where ψ_A and ψ_B represent the contribution from the atomic sites of A and B in the unit cell for the graphene, and ϕ is the angle from the *x*-axis in the k_x-k_y plane. This means that the wave function of the Dirac cone is simply representable by using the phase term ϕ, which also expresses the pseudo-spin state of the Dirac cone electron. On the other hand, the photoelectron emission intensity is determined by the matrix element $\langle \Phi_f | \vec{E} | \Phi(\varepsilon, \phi) \rangle$ where $\vec{E}$ is the electromagnetic field provided by the photons, and Φ_f is the final state being often regarded as the plane wave of the free electron. $\vec{E}$ is determined by the polarization of the photon when the photon energy is fixed. In the case of the linear polarization, this is expressed by the polarization angle θ. In short, the intensity distribution of the angle-resolved photoelectron spectrum (ARPES) is a complex function of both the two phase terms; those of wavefunction and photon, and since graphene is probably the most simple material, the investigation of the angular distribution of the photoelectron intensity from graphene has been investigated extensively[1,2].

The The experiments were carried out at the BL-1 of HiSOR, where the polarization angle can be varied at any value from the s-pol to p-pol by rotating the analyzer chamber equipped with the electron analyzer. The single-layered epitaxial graphene on SiC substrate was used and temperature during the measurement was 30K.
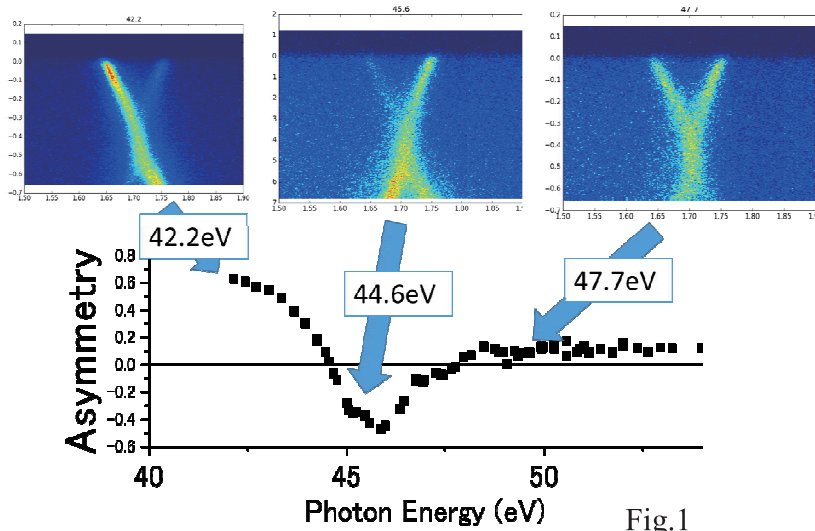
Fig. 1 shows the ARPES spectrum along the Γ-K-M line at indicated photon energies when the polarization angle is 80deg (nearly s-pol), and the intensity asymmetry defined as $(I_p - I_s) \big/ (I_p + I_s)$ where I_p is the intensity of the branch near to the Γ-point at the Fermi edge (left one at the Fermi edge) and I_s denotes that at the the other branch. By assuming a simple photoelectron excitation scheme under the Dipole approximation, the intensities of the I_p and I_s are proportional to

Fig.1

$I_s = |E| \mu_y \sin^2 \theta$ and $I_p = |E| \mu_x \cos^2 \theta$, where $|E|$ is the magnitude of the photon, and μ_x and μ_y are the the transition-dipole moments (excitation matrix element) along x and y axis. Surprisingly, this quantity drastically changes as a function of the photon energy. Few eV's is enough to make the +0.6 to -0.45. Since the initial state is constant, and μ can only perturbed by the final state, the experimental results clearly demonstrate that the final state of the photoelectron excitation drastically changes in its properties as a function of the energy. It is impossible to explain if the plane wave is assumed as a final state. Thus, even in the 45eV above the Fermi level, the wave function related to the photoexcitation process is not the plane wave but that of the graphene itself.

Left part of the Fig.2 shows the asymmetry similarly to the lower part of the Fig.1, and the right part shows the intensity distribution of the ARPES at binding energy. The intensity distribution in the ARPES spectra shows the drastic change as a function of the binding energy, and rotates around the K-point with the binding energy; forming a peculiar helical structure. The right of the vertical line corresponds the photon energy used in the ARPES, and the width of the horizontal arrow is the same as the region of the binding energy used in the ARPES. It is well established that the electronic property of the Dirac cone electron is nearly the same along the binding energy when the linear dispersion relation is satisfied in the small binding-energy region. Thus, the change in the intensity distribution as a function of the binding energy is considered to be due to the effect of the change in the final state. This is consistent with the drastic change in the asymmetry in intensities along the Γ-K-M line at the Fermi level. However, it is impossible to represent the intensity distribution around the K-point by linear combination of the angular distribution with s-polarized light and p-polarized light which give $\sin^2\theta$ and $\cos^2\theta$ dependences, suggesting that the above interpretation where only the s- and p- components contribute the intensity is not incomplete. Instead, it is necessary to introduce the contribution from the circularly polarized light whose angular distribution which gives $\sin^2(\theta+\delta)$ intensity dependence where δ is the phase-angle at which the intensity vanishes. The contribution from the circularly polarized light is considered partly due to the photoelectron excitation by the reflected photons. It is commonly known that the linearly light which has a tilted polarization angle from the high-symmetry line gives the ellipsoidally polarized light as a result of the reflection on the solid surface. This is due to the difference in the phase-shift of the photons of s- and p- polarization at the reflection, and thus the polarization state of the reflected light is very sensitive to the dielectric properties (complex refractive index or dielectric function) of both the substrate and the adsorbed layer. More quantitative analysis is now under progression for a deeper understanding this interesting phenomenon.
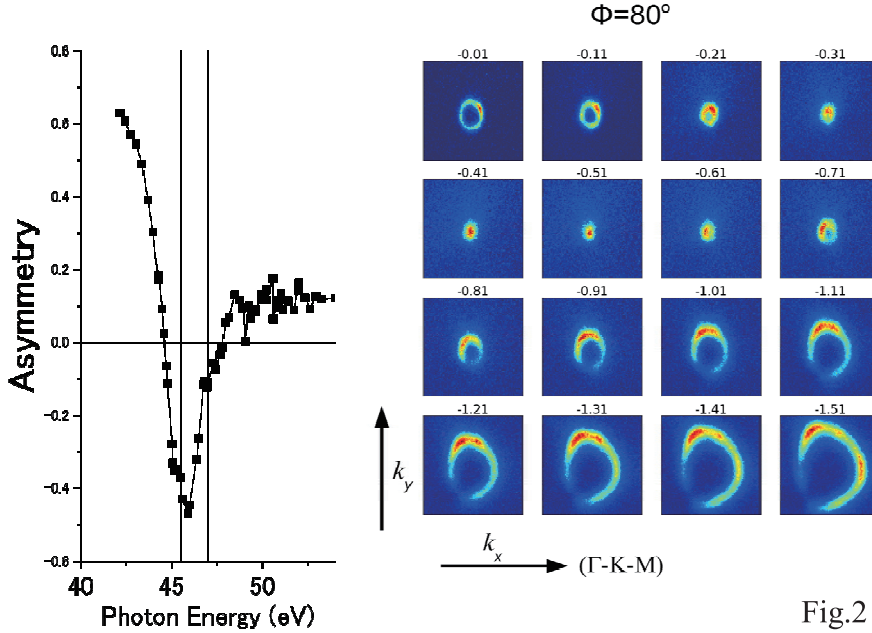

Fig.2

References
1. M. Mucha-Kruczyński et al., Phys. Rev. B 77, 195403 (2008); Y. Liu et al. Phys. Rev. Lett. 107 166803 (2011); I. Gierz et al. Phys. Rev. B 83 121408(R) (2011) ; C. Hwang et al., Phys Rev. B 84 125422 (2011); I. Gierz et al., Nano Lett. 12 3900 (2012).
2. P. Porya et al, Phys. Rev. B. 92 (2015) 195148.

Observation of *d* electron quantum-well states in Pd(100) ultrathin films

Shunsuke Sakuragi[a], Hidetake Tanabe[a], Eike F. Schwier[b],
Kenya Shimada[b], and Tetsuya Sato[a]

[a]*Department of Applied Physics and Physico-Informatics, Keio University, Hiyoshi, Yokohama 223-0061, Japan*
[b]*Hiroshima Synchrotron Radiation Center, Hiroshima University, Higashi-Hiroshima 739-0046, Japan*

Keywords: Pd, ultrathin film, quantum-well states

Quantum-well states, which is appeared in metal ultrathin films establish the quantum-well subband near the Fermi energy of the metal, and modify the physical properties in an oscillatory manner depending on the film thickness [1]. Recently, the spontaneous magnetization appearing in Pd(100) ultrathin films, which is nonmagnetic in bulk form has been reported [2, 3]. The magnetization of the Pd(100) films oscillate dependent on the film thickness, and the period of oscillation is consistent with the *d* electron quantum-well states in Pd. From the stand point of Stoner's criterion, this phenomenon is explained that the increase in the density of states near Fermi energy occurs by nanoscaling in metals. Because of its potential for the development of novel magnetic nanoscale materials whose magnetism can be controlled, this matter is of great technological interest [4].

Angle-resolved photoelectron spectroscopy (ARPES) measurement visualizes the band dispersion of the substances. The quantitative analyses of the quantum-well states in the metal thin films have been performed by ARPES measurement, and the subbands of quantum-well states in the metals are well understood by the phase accumulation model [5]. In this study, we performed the ARPES measurement for Pd(100) ultrathin films in order to observe the *d* electron quantum-well states of Pd(100) ultrathin films. From this measurement, we tried to discuss the relationship between the magnetism and quantum-well states directly.

All experiments were performed at the HiSOR beamline BL-1. To prevent charged up, Cu(100) single crystal was used as a substrate. Cu(100) was prepared by 1-2 keV Ar^+ sputtering and subsequent annealing at ~900 K in the ultra-high vacuum chamber, and Pd was deposited on this substrate at room temperature. The thickness of the Pd was estimated by the reflected high-energy electron diffraction (RHEED) oscillation measurement [Fig. 1 (a)]. Fig. 1 (b) shows low-energy electron scattering (LEED) image of Pd film on Cu(100) substrate. The four-fold streaky spots were observed. This indicates that Pd grew epitaxially on Cu(100) surface but Pd had a lot of islands and/or the crystallinity of the film was low.
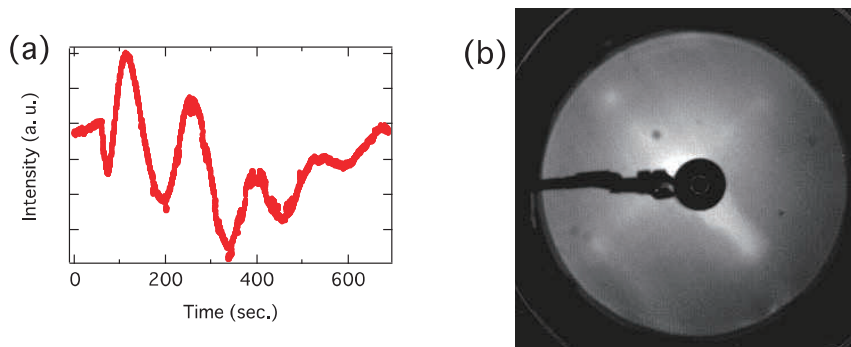

FIGURE 1. (a) RHEED oscillation during the deposition of Pd on Cu(100) substrate. The oscillatory manner of the RHEED intensity was observed, and the film thickness was estimated from the period of this oscillation. (b) LEED image of Pd film on Cu(100) substrate. The streaky spots were observed. This indicates that low crystallinity Pd(100) films grew on Cu(100).

Figure 2 (a) shows the results of ARPES measurement of the 7 monolayers Pd(100) ultrathin film. This measurement was performed at 30 K and the 25 eV of excitation light with p-polarization was used. The band dispersions were observed, however the bands were broad, and we performed the smoothing of the data using second order differential. In Fig. 2 (a), the band dispersion, which was different with the bulk band, was observed around the -1 eV in the ΓM line. The binding energy of this band was changed dependent on the film thickness. In order to evaluate the dimensionally of this band, we performed the energy of excitation light dependent energy distribution curves measurement around the Γ point [Fig. 2 (b)]. There was no energy dependence, i.e., k_z dependence in this band dispersion. Thus, this band dispersion is originated from the two dimensional electrons.

Previously, the scanning tunnel spectroscopy measurement and first-principle calculation were reported in the same system as our present study [6], and the existence of the band dispersions originated from the quantitazing of the $d_{xz,yz}$ character of Pd around -1 eV was shown. Our present ARPES measurement is consistent with these results. Because present sample had low crystallinity, the experimentally observed band dispersions were broad. Thus, we cannot detail discuss of the quantum-well states from present ARPES measurement result. Measuring the ARPES with high crystallinity sample is required to analyze the quantum-well states using phase accumulation model.

In this beam time, we succeeded the observation of the d electron quantum-well states in Pd(100) ultrathin films by the ARPES measurement. In the future, we will prepare the high crystallinity sample, and discuss the relationship between the quantum-well states and magnetism of the Pd(100) ultrathin films. This will clarify the origin of the appearance of ferromagnetism in nanosized Pd.
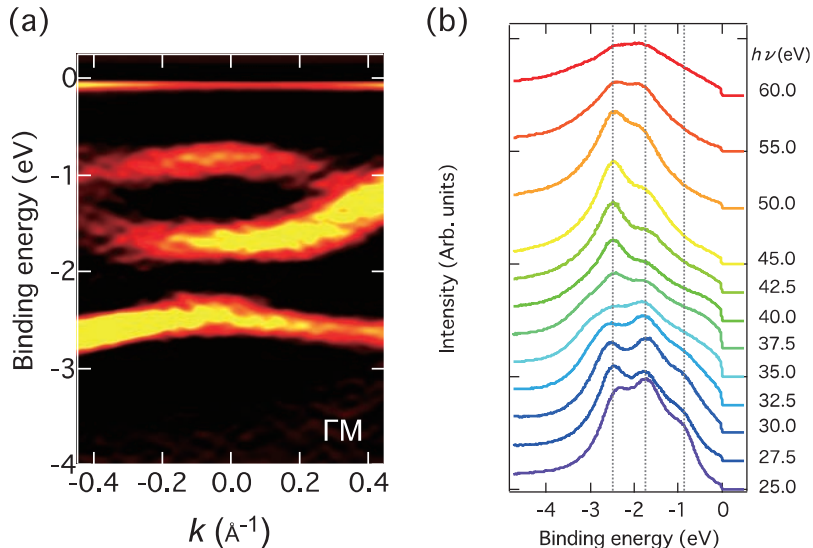

FIGURE 1. (a) Band dispersion of the 7 monolayer Pd(100) ultrathin film. The incidence light is the 25 eV with p-polarization. (b) Excitation light energy dependent energy distribution curves around the Γ point.

REFERENCES

1.   T.-C. Chiang, Surface Science Reports **39**, 181 (2000).
2.   S. C. Hong, J. I. Lee, and R. Wu, Phys. Rev. B **75**, 172402 (2007).
3.   S. Sakuragi, *et al.*, Phys. Rev. B **90**, 054411 (2014).
4.   S. Aihara, H. Kageshima, T. Sakai, and T. Sato, J. Appl. Phys. **112**, 073910 (2012).
5.   J. E. Ortega, F. J. Himpsel, G. J. Mankey, and R. F. Willis, Phys. Rev. B **47**, 1540 (1993).
6.   S. K. Saha, S. Manna, M. Przybylski, V. S. Stepamyuk, and J. Kirschner, Phys. Rev. B **90**, 081404(R) (2014).

Polarization-Dependent ARPES Study of the Antiferromagnetic Phase of Ba(Fe$_{1-x}$Co$_x$)$_2$As$_2$

H. Takita[a], **N. Kishimoto**[a], **Y. Nakashima**[a,b], **W. Mansuer**[a], **A. Ino**[a,b], **M. Arita**[c], **H. Namatame**[c], **M. Taniguchi**[a,c], **Y. Aiura**[b,d], **I. Hase**[b,d], **H. Eisaki**[b,d], **K. Kihou**[b,d], **C. H. Lee**[b,d], **A. Iyo**[b,d], **M. Nakajima**[b,e], and **S. Uchida**[b,e]

[a]*Graduate School of Science, Hiroshima University, Higashi-Hiroshima 739-8526, Japan*
[b]*JST, Transformative Research-Project on Iron Pnictides (TRIP), Chiyoda, Tokyo 102-0075, Japan*
[c]*Hiroshima Synchrotron Radiation Center, Hiroshima University, Higashi-Hiroshima 739-8526, Japan*
[d]*National Institute of Advanced Industrial Science and Technology, Tsukuba 305-8568, Japan*
[e]*Department of Physics, University of Tokyo, Tokyo 113-0033, Japan*

In iron-pnictide superconductors, it has been argued that various kinds of degree of freedom like spin, orbital and phonon can play an important role in mechanism of superconductivity. Such rich ingredients are considered to be important also for the electronic structure in other phases, which is adjacent to the superconducting phase. For example, Ran *et al* showed that Dirac electron could appear in the magnetically ordered phase [1]. An ARPES study in fact showed the presence of Dirac cone in the antiferromagnetic phase of BaFe$_2$As$_2$ [2]. However, mechanism of occurrence of the Dirac cone is still unclear because of the lack of experimental input. Specifically, the role of the orbital degree of freedom is unclear since most of experimental methods can probe physical quantities, which is integrated for all the orbitals.

Here we performed a polarization-dependent ARPES study of the antiferromagnetic phase of Ba(Fe$_{1-x}$Co$_x$)$_2$As$_2$ (x = 0.02) to study the role of orbital degree of freedom in the electronic structure. Owing to the dipole-selection rule, polarization-dependent ARPES is a powerful tool to investigate the symmetry of electronic structure. The experiment was performed at BL1 of Hiroshima synchrotron radiation center. In BL1, whole of the experimental chamber is rotatable without changing incident light axis. From the viewpoint of the sample, polarization angle of the photon can be continuously changed. The photon energy was set to 80 eV and the polarization angles of the photon were set to 0°, 45° and 90°. In the ARPES geometry of BL1, the polarization angle of 0° and 90° corresponds to the p- and s-polarization, respectively.

Figure 1(a)-(c) shows momentum distribution of photoemission intensity around the X point in the AF phase of Ba(Fe$_{0.98}$Co$_{0.02}$)$_2$As$_2$. The angle of the polarization vector is 0°, 45° and 90° with respect to the Γ-X line, respectively. Since the reflection symmetry about the Γ-X line is conserved in the AF phase of Ba(Fe$_{0.98}$Co$_{0.02}$)$_2$As$_2$, one would expect that the band dispersion is also symmetric with respect to the Γ-X line. As seen in Fig. (a) and (c), the intensity distribution taken with p- and s-polarization is symmetric about the Γ-X line, indicating that the band structure indeed is symmetric about the Γ-X line. However, in contrast to this, as seen in Fig. (b), intensity distribution taken with 45°-polarization, which is an admixture of the p- and s-polarization, is asymmetric with respect to the Γ-X line. This implies that the relative phase between p- and s-polarization plays a certain role in the intensity distribution. Here we focus on the intensity distribution around (k_x, k_y) = (0, 3.03) Å$^-$

[1], in which the Dirac-cone band dispersion has been observed [ref]. With p-polarization, the intensity is distributed in the side of $k_x > 3.03$ Å^{-1}. This indicates that band dispersion in near-X side has an even parity with respect to the Γ-X line by assuming the dipole-selection rule. In a same sense, the band dispersion in the side of $k_x > 3.03$ Å^{-1} has an odd parity $k_x > 3.03$ Å^{-1}. With 45°-polarization, the intensity is distributed in the side of $k_x > 3.03$ Å^{-1}. The intensity variation with rotating the polarization vector angle can be explained by a scenario that the Dirac cone is formed by hybridization between two bands with d_{xy} and d_{yz} orbital character.

In summary, we performed an ARPES study of Ba(Fe$_{0.98}$Co$_{0.02}$)$_2$As$_2$ in the antiferromagnetic phase to study the role of orbital degree of freedom in electronic structure. We have observed that the intensity distribution around $(k_x, k_y) = (3.03, 0)$ Å^{-1}, in which the Dirac cone is expected to be present, varies by changing the polarization angle of the incident photon from 0° to 90°. This result implies that the Dirac cone in iron pnictides is formed by hybridization of two bands with d_{xy} and d_{yz} orbital character.
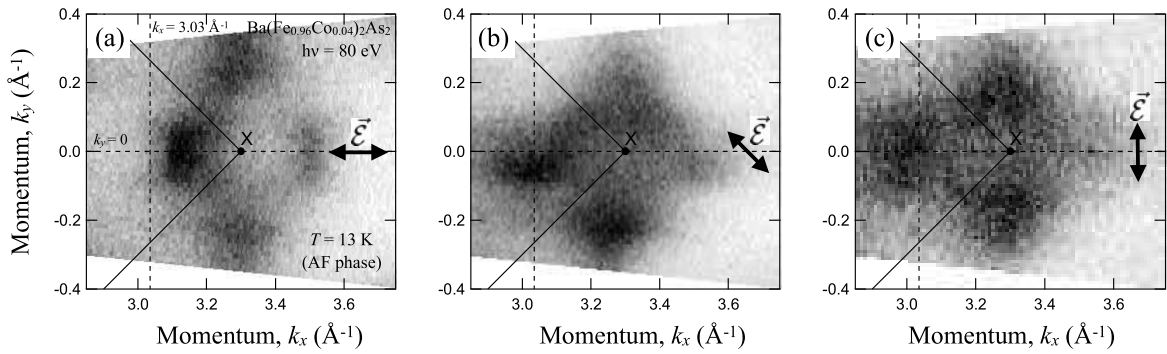

FIGURE 1 Momentum distribution of ARPES intensity at the Fermi energy for the AF phase of Ba(Fe$_{0.96}$Co$_{0.04}$)$_2$As$_2$, taken with $hv = 80$ eV at $T = 13$ K using (a)p-polarization, (b)45° -polarization and (c)s-polarization. The black area denotes high spectral intensity. The intensity was integrated over an energy window of 10 meV.

REFERENCE

1. Y. Ran *et al.*, *Phys. Rev. B*, **79,** 014505 (2009).
2. P. Richard *et al*, *Phys. Rev. Lett.* **104**, 137001 (2010).

The electronic structure at the interface between a metal thin films and a topological insulator

M. Nakanishi[a], E. F. Schwier[b], K. Shimada[b]

[a] *Graduate School of Science, Hiroshima University, Higashi-Hiroshima 739-8526, Japan*
[b] *Hiroshima Synchrotron Radiation Center, Hiroshima University, Higasi-Hiroshima 739-0046, Japan*

Keywords: topological insulator, Angle Resolved Photoelectron Spectroscopy, in-situ deposition, band-bending

The surfaces of topological insulators (TI) exhibit a strongly spin-polarized robust surface state, so called the Dirac Cone. This makes them a promising candidate for application in spintronics devices. In order to realize such devices, it is necessary to attach electrodes to TI in order to integrate them into the circuits. In view of this, it is essential to know what kind of influence the contacting electrode has on the Dirac Cone, which is then being situated at the newly formed TI-metal interface. For this reason, we examine the behavior of the Dirac Cone of the model topological insulator Bi_2Se_3 upon deposition of thin Au films, by means of Angle Resolved Photoemission Spectroscopy (ARPES). At the same time, we probed Bi 5d and Se 3d core level peaks by means of Photoemission Spectroscopy (PES).

ARPES measurements were carried out at the endstation of the linear undulator beamline (BL-1) at HiSOR. The Au thin films were deposited on the Bi_2Se_3 *in situ* during the ARPES measurements. By monitoring the evolution of the Dirac Point (DP) as well as the Bi 5d and Se 3d core-level shifts [2] during the deposition (T =15 K), it was possible to resolve the change of the lineshape and binding energy of the PES spectral features as a function of the amount of Au deposition (Fig. 1). Due to the high time sampling rate, it was possible to fit the evolution of the core level binding energy and energy splitting of the surface- and bulk-derived components (surface-core-level shift) as a function of deposition time (Fig. 2).
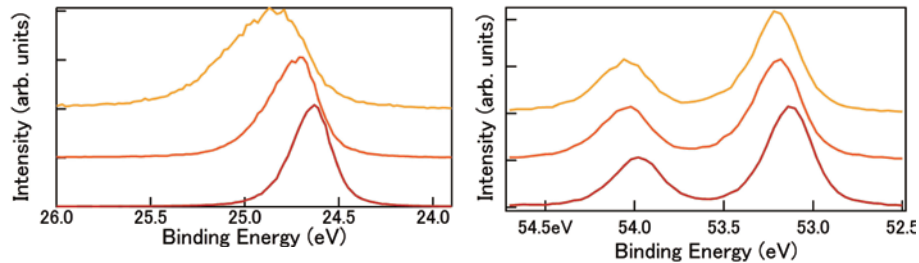

FIGURE 1 (a) The change of the $Bi5d_{5/2}$ peak as a function of different Au coverage (b) Se3d peak as a function of different Au coverage. The FWHM (Full Width Half Maximum) of the $Bi5d_{5/2}$ peak became larger due to the increased surface-core-level-splitting. It suggests that chemical bonding states are different between surface and bulk. However, The FWHM of Se3d peak did not change significantly compared with the Bi5d peak.

During the deposition of Au, the Bi 5d core-levels are shifted to higher binding energies and the surface-core-level shift is increased after an initial rigid-band-like shift of the electronic structure (DP binding energy up to 0.35 eV). The Se 3d, on the other hand, does not exhibit any change of its shape indicating the absence of surface core-level shifts.
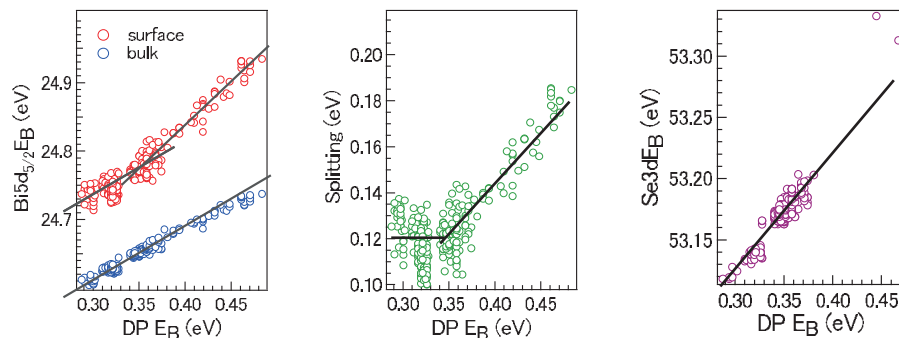

FIGURE 2 Left: Bi 5d bulk, surface core-level binding energy with respect to the Dirac Point chemical shift
Middle: The splitting of bulk peak and surface peak shift Right: Se 3d shift.

Bi_2Se_3 is a layered material with a Se - Bi - Se - Bi - Se quintouple layer structure, and naturally an n-type semiconductor. The surface state appears as a linear energy dispersion inside the bulk band gap. It is considered that there exists band bending toward higher binding energy due to the electron doping in a few atomic layers near the surface, which is responsible for the emergence of a Rashba-type two-dimensional electron gas (2DEG) [1,3,4].

The different shift between surface and bulk Bi 5d, *i.e.* the change of the magnitudes of the surface-core-level shift, is consistent with a standard band-bending model. Here the atoms closer to the surface will be affected more strong, by the increased band bending. The absence of a Se 3d surface core-level however casts question on the nanoscopic validity of the band-bending description as well as the presence of the "kink" in the splitting between Bi 5d species. As there are no detectable surface-core-level shifts for Se atoms at the surface and in the deeper region, we assume that the band bending would be more like the sketch in Fig. 3, which is different from a smooth variation assumed in the standard band-bending model.
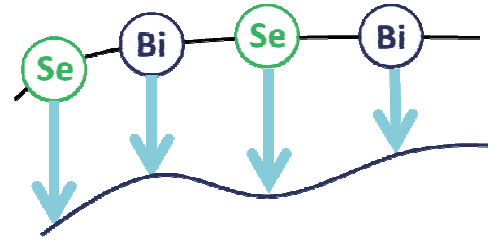

FIGURE 3 The schematic diagram of band bending model

REFERENCES

[1] M. Bianchi et al., Nature Comunications **1**, 128 (2010).
[2] E. F. Schwier, unpublished work under HiSOR proposal 14-A-41 (2014).
[3] M.S. Bahramy, P.D.C. King Nature Communications **3**, 1159 (2012).
[4] Marco Bianchi, PhD thesis, Electronic structure and electron dynamics of the topological insulator Bi_2Se_3 (2013).

Angle-resolved photoemission spectroscopy study of Yb$_2$Pt$_6$Ga$_{15}$

A. Rousuli[1], H. Sato[2], T. Ueda[3], Y. Matsumoto[3], S. Ohara[3],
T. Nagasaki[1], E. F. Schwier[2], M. Zheng[1], K. Shimada[2], M. Arita[2],
H. Namatame[2] and M. Taniguchi[2]

[1]Graduate School of Science, Hiroshima University, Higashi-Hiroshima 739-8526, Japan
[2]Hiroshima Synchrotron Radiation Center, Hiroshima University, Higashi-Hiroshima 739-0046, Japan
[3]Graduate School of Engineering, Nagoya Institute of Technology, Nagoya 466-8555, Japan

Keywords: heavy Fermion, effective mass, Kondo temperature, c-f hybridization energy

Among strong correlation electron systems, Yb-based heavy Fermions has been attracted by very interesting physical phenomena such as heavy fermion behavior, valence fluctuation, superconductivity. The specific-heat coefficient is a characteristic parameter of the heavy Fermion compounds, which is related to the electron effective mass (m^*). Formation of the heavy Fermion has been believed to be derived by the competition between the inter-site Ruderman-Kittel-Kasuya-Yosida (RKKY) interaction and on-site Kondo effect, both are due to the hybridization between $4f$ state and conduction band (c-f hybridization). When RKKY interaction is dominant, the $4f$ electrons indirectly interact with each other and leading antiferromagnetic magnetic ground state. On the other hand, when Kondo effect is dominant, the $4f$ moment is screened with conduction electrons and non-magnetic Fermi liquid behavior is observed. Recently, we performed hard x-ray photoemission spectroscopy (HAXPES) measurement on the Kondo lattices Yb$_2$Pt$_6$X$_{15}$ (X=Al, Ga) [1]. The Kondo temperature (T_K) estimated from magnetic susceptibility measurements is ~60 K for Yb$_2$Pt$_6$Al$_{15}$ [2], while higher than 1000 K for Yb$_2$Pt$_6$Ga$_{15}$. The Yb valences estimated from Yb $3d$ HAXPES spectra is ~2.89 for Yb$_2$Pt$_6$Al$_{15}$ at 250 K and decreases to 2.83 at 20 K, while that of Yb$_2$Pt$_6$Ga$_{15}$ is ~2.34 at 300 K with almost no temperature dependence. These results indicate strong c-f hybridization of Yb$_2$Pt$_6$Ga$_{15}$ [1]. In this study, to directly see the c-f hybridization and the Fermi surface, we performed high resolution angle-resolved photoemission spectroscopy (ARPES) on Yb$_2$Pt$_6$Ga$_{15}$ at BL-1 and BL-9A of HiSOR. The sample was cleaved in situ and kept in ultra-high vacuum level better than ~10^{-9} Pa at 20 K during measurement.

Figure 1(a) shows two-dimensional Fermi surface image of Yb$_2$Pt$_6$Ga$_{15}$ measured at 20 K with an incident photon energy of $h\nu$=35 eV. We can see the Fermi surface with six-fold symmetry and the first Brillouin zone is mainly dominated by three ellipse shape structures, which overlap with each other at around Γ point and forms almost circular shape structure. The electronic band structure along the Γ-M direction taken by ARPES at 20 K with $h\nu$=35 eV is shown in Fig. 1(b). The parabolic dispersive conduction bands cross with the flat Yb $4f_{7/2}$ band at ~0.2 eV and $4f_{5/2}$ band at 1.48 eV.

The enlarged image of Fig. 1(b) is shown in Fig. 2. The localized flat $4f$ band at 0.19 eV hybridizes with the dispersive conduction band at around 1.5 Å^{-1} and forms c-f hybridization, and the band-bending feature clearly observed at the cross point. Since the T_K is given by using $T_K = \varepsilon_f / k_B$, where ε_f is the renormalized $4f$ band energy and k_B is the Boltzmann constant, the evaluated T_K from the present experiments is ~2200 K, which is not contradict with the magnetic susceptibility measurement results [2].

The spectra were analyzed by using periodic Anderson model in which the energy dispersion is expressed by

$$E = (k) \quad \frac{\varepsilon_f + \varepsilon_k \pm \sqrt{(\varepsilon_f - \varepsilon_k)^2 + 4|V_k|^2}}{2},$$

where ε_k and V_k are the k-dependent (momentum-dependent) energy of the conduction-band and c-f hybridization energy, respectively. We assumed that V_k takes the constant value of V, independent of k. The estimated c-f hybridization enethat$V$~0.13 eV, which is comparable to that for YbAl$_2$ for the outer band (0.186

eV) [3]. The mass enhancement factor was estimated from the ratio of the bare conduction-band velocity (v) to the hybridized band velocity (v^*) at the Fermi level by the relation

$$\frac{m^*}{m} = \frac{v}{v^*} = \frac{\partial \varepsilon_f}{\partial k} \Big/ \frac{\partial E}{\partial k},$$

where m is the bare band mass and E^+ is the energy of the c-f hybridization band. From the analysis of the ARPES results, the m^*/m-value was estimated to be ~1.59, implying that the band renormalization effect is not so strong. In our future work, we will perform ARPES measurement on $Yb_2Pt_6Al_{15}$ for comparison.

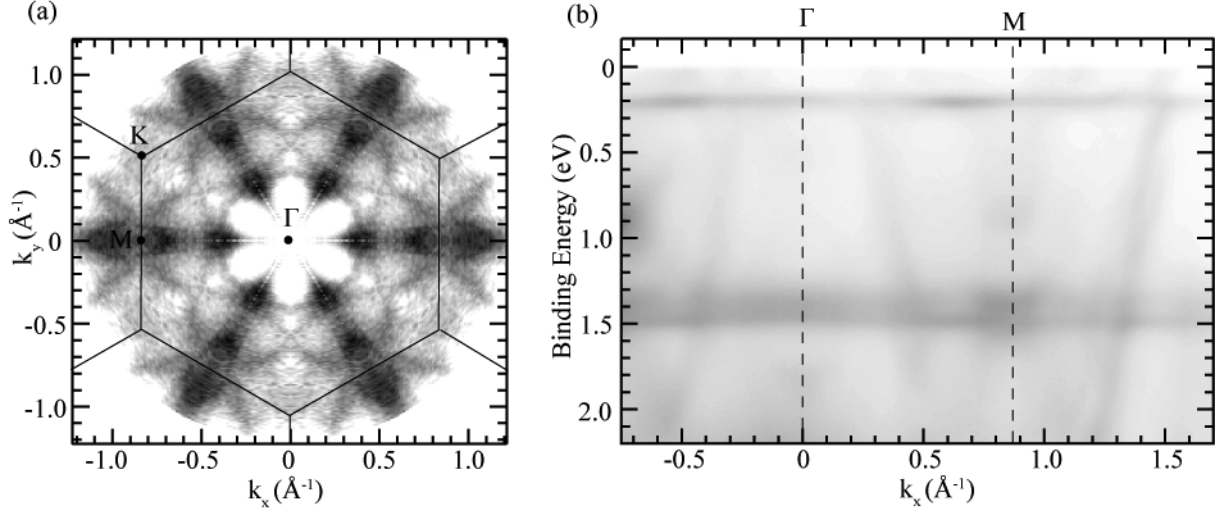FIGURE 1. Intensity plot of ARPES spectra of $Yb_2Pt_6Ga_{15}$ measured at 20 K with $h\nu$=35 eV. (a) two-dimensional Fermi surface mapping and (b) band dispersion along Γ-M direction.

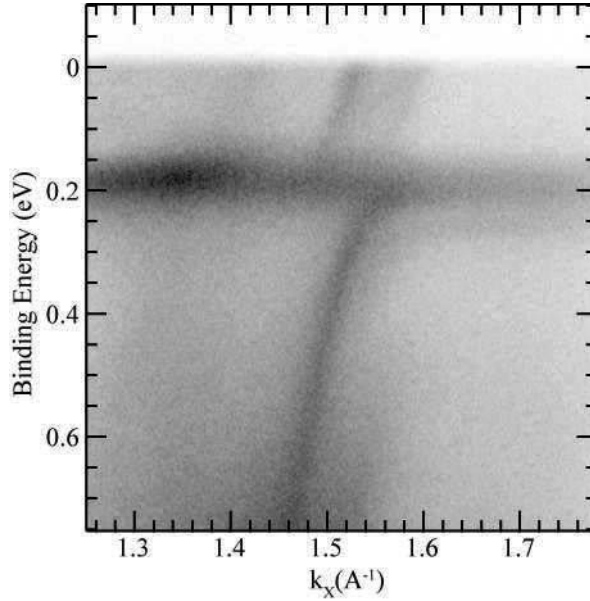FIGURE 2. Intensity plot of ARPES spectra of $Yb_2Pt_6Ga_{15}$ along Γ-M direction at 20 K with $h\nu$=35 eV.

REFERENCES

1. A. Rousuli *et al.*, to be submitted to Phys. Rev. B
2. M. Deppe *et al.*, New J. Phys. **10**, 093017 (2008).
3. M. Matsunami *et al.*, Phys. Rev. B **87**, 165141 (2013).

Indication of the Energy Gap at the Dirac Point in Graphene/Pt(111) by Gd deposition

A. G. Rybkin[a], E. F. Schwier[b], K. Shimada[b,c], A. Kimura[c], A. M. Shikin[a]

[a] *Saint Petersburg State University, Ulyanovskaya 1, Saint Petersburg 198504, Russia*
[b] *Hiroshima Synchrotron Radiation Center, University of Hiroshima, 2-313 Kagamiyama Higashi-Hiroshima 739-0047, Japan*
[c] *Graduate School of Science, Hiroshima University,1-3-1 Kagamiyama, Higashi-Hiroshima 739-8526, Japan*

Graphene is one of the most promising materials for nanoelectronics due to its unique Dirac cone-like dispersion of the electronic state and high mobility of the charge carriers. In particular, being a nonmagnetic material with a weak spin-orbit coupling, graphene opens the prospects for the modification of the electronic spin structure and appearance of exotic phenomena and novel applications.

Recently a possibility of topological energy gap formation of ~200 meV at the Dirac point in graphene synthesized on Pt(111) with intercalated Pb atoms was shown theoretically and experimentally [1]. Similar effect of the topological opening of the energy gap was theoretically calculated directly for pristine graphene synthesized on Pt(111) [2] due to the substrate-induced enhanced spin-orbit interaction. So, the system graphene/Pt(111) attracts considerable interest and allows to modify the properties of graphene in the required direction.

However the Dirac point in the graphene/Pt(111) system is located above the Fermi level (Fig. 1 (a,c)) that does not allow the test the gap opening by direct photoemission. The effective way to modify the electronic structure and to shift the Dirac point can be adsorption of Gd adatoms atop of graphene. Among possible adsorbates, rare-earth metals and Gd in particular are interesting and unexplored candidates. On the one hand, according to Ref. [3] adsorption of Gd on top of graphene on different metal substrates leads to strong *n*-doping of graphene without modification of the Dirac cone dispersion at the K point in opposite to the case of adsorption of alkali metals followed by their intercalation underneath a graphene with the Dirac point gap opening already at room temperature. On the other hand, in contrast to transition metals, Gd has a large local magnetic moment, which is preserved in nearly all environments. Therefore, it is expected that adsorption of Gd (as a magnetic metal) on top of graphene should be followed by opening of the energy gap at the Dirac point due to hybridization between the graphene π and metal d states in the region of the K point of the Brillouin zone and the time reversal symmetry breaking that results in formation of the topological-like phase [4,5]. Therefore, partial deposition of Gd atop a graphene/Pt(111) will be followed by interaction between exchange magnetic (provide by Gd) and spin-orbit (provided by Pt) coupling that assumes to modify the topological phase and corresponding modification of electronic structure of the formed topological phase.

Aim of this work was to study a shift of the Dirac point in graphene/Pt(111) below the Fermi level by deposition of Gd atoms and detailed study of the electronic structure of the graphene π states in the region of the Dirac point by angle-resolved photoemission.

The graphene monolayer was synthesized at Pt(111) by cracking of the propylene (C_3H_6) at a pressure of 1×10^{-7} mbar and a sample temperature of 1200 K during 60 min [2]. All ARPES dispersion measurements were performed on the BL-1 HiSOR beamline at the temperature of 30 K.

Figures 1(a-c) show the electronic structure of graphene π states near the Dirac point for graphene synthesized on Pt(111). Dispersion relations were measured at the photon energy of 40 eV in two orthogonally related direction of the surface Brillouin zone: along $\overline{\Gamma K}$ and perpendicular to $\overline{\Gamma K}$. It has been observed that for graphene on Pt(111) the Dirac point is located above the Fermi level of about 180 meV. The kinks in graphene π states distinguished in the ARPES dispersion map at the 0.5-0.6 eV of binding energy below the Fermi level is formed due to hybridizations between the graphene π and Pt *d* states.

After Gd deposition atop of graphene followed by annealing of the system up to 600ºC the energy shift of the Dirac point below the Fermi level is observed and π* states are clearly visible (Fig. 1 (d,e)). Moreover a large energy gap is opened at the Dirac point (Fig. 1e).
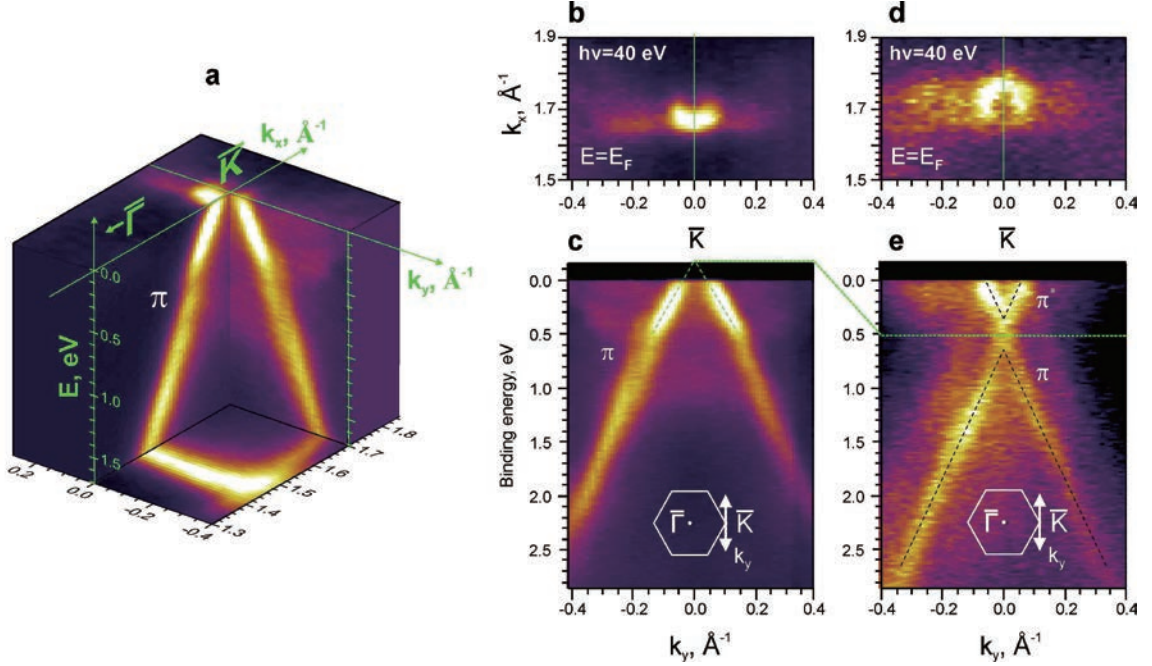

FIGURE 1. ARPES data: (a) – Overview of the Dirac cone dispersion map for graphene/Pt(111) both in (k_x) and (k_y) directions, (b) – The k_x, k_y energy cut of the Dirac cone at the Fermi level for graphene/Pt(111). (c) – The ARPES dispersion map for graphene π states for graphene/Pt(111) measured in the direction orthogonal to $\overline{\Gamma K}$. (d) – The k_x, k_y energy cut of the Dirac cone at the Fermi level measured for graphene/Pt(111) after Gd deposition. (e) – The ARPES dispersion map for graphene π states for Gd+graphene/Pt(111) measured in the direction orthogonal to $\overline{\Gamma K}$. The photon energy is 40eV. All ARPES data were measured at the temperature of 30 K.

As a result, we can conclude that the Gd deposition on top of graphene/Pt(111) and annealing of the system leads to effective *n*-doping of graphene with the energy shift of the Dirac point below the Fermi level, and the energy gap is observed at the Dirac point. The character and causes of the gap formation require an additional investigation for analysis of the nontrivial structure and topological phase in graphene.

REFERENCES

1. I. I. Klimovskikh, M. M. Otrokov, V. Yu. Voroshnin, D. Sostina, L. Petaccia, G. Di Santo, S. Thakur, E. V. Chulkov, and A. M. Shikin *"Spin–Orbit Coupling Induced Gap in Graphene on Pt(111) with Intercalated Pb Monolayer"* ACS Nano, **11** (1), pp 368–374 (2017)
2. I. I. Klimovskikh, S. S. Tsirkin, A. G. Rybkin, A. A. Rybkina, M. V. Filianina, E. V. Zhizhin, E. V. Chulkov, and A. M. Shikin *"Nontrivial spin structure of graphene on Pt(111) at the Fermi level due to spin-dependent hybridization"* Physical Review B **90**, 235431 (2014)
3. A. Varykhalov, M. R. Scholz, Timur K. Kim, and O. Rader *"Effect of noble-metal contacts on doping and band gap of graphene"* Physical Review B **82**, 121101(R) (2010)
4. Z. Qiao, S. A. Yang, W. Feng, W.-K. Tse, J. Ding, Y. Yao, J. Wang, and Q. Niu *"Quantum anomalous Hall effect in graphene from Rashba and exchange effects"* Physical Review B 82, 161414(R) (2010)
5. J. Ding, Z. Qiao, W. Feng, Y. Yao, and Q. Niu *"Engineering quantum anomalous/valley Hall states in graphene via metal-atom adsorption: An ab-initio study"* Physical Review B 84, 195444 (2011)

Investigation of the Electronic Structure of Te(0001), Determination of the Band Structure, Surface States and Topological Order

F. Titze[a] and M. Mulazzi[a]

[a]Humboldt-Universität zu Berlin, Institut für Physik, Newtonstr. 15, D12489 Berlin, Germany

Keywords: Electronic structure, ARPES, topological order, Tellurium.

The aim of the experiment was the determination of the electronic structure of Te(0001). Previous measurements on cleaved and sputter/annealed samples allowed us to measure the electronic structure on another face of Tellurium, namely the (10-10). However, it is known that different terminations of the same crystal can have different properties, for instance one can show a surface reconstruction and/or surface states while the other not. Therefore, to have a complete picture of the electronic structure of a material experiments on several low-Miller indices surfaces have to be done.

On BL1, we undertook the measurement of the electronic structure of Te(0001) on a single crystal grown by the Czochralski method of 99.999% purity. Particular care has been dedicated to the sample preparation, which we chose to be sputtering and annealing. We sputtered the sample at an ion energy of about 500 eV and annealed at progressively higher temperatures up to about 350°C. This procedure has been adopted to avoid the known risk accompanying heating Te, namely sublimation in UHV, which can pollute the vacuum chamber. By this procedure we made sure that no Te sublimated during the experiment.

After the surface preparation, we measured photoemission and Auger spectra to make sure that the surface was free from contaminants. While at the beginning of the experiment a Carbon peak could be clearly measured, after 5 preparation cycles the Carbon level was below the detection limit, as well as other possible contaminants, like Sulfur and Oxygen, and only the Te Auger transition were measured.

Contrary to the ARPES spectra on the (10-1) surface, the spectra of the (0001) surface showed very broad peaks, as shown in Fig. 1.
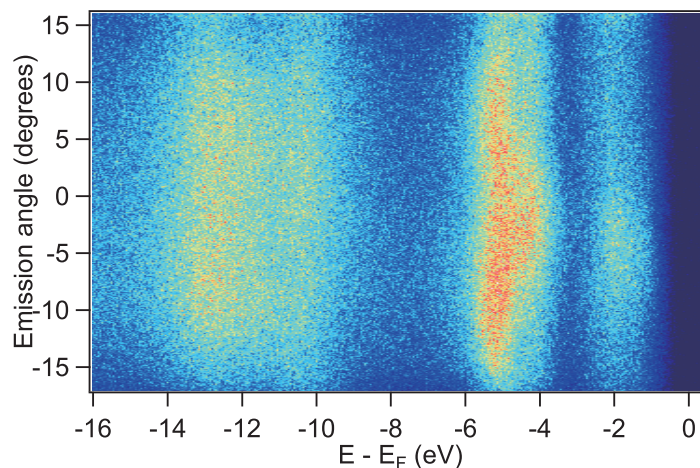

FIGURE 1. ARPES spectrum at normal emission taken with a photon energy of 60 eV. While a band dispersion can be observed, especially in the band manifold between -4 and -6 eV, the photoemission peaks are broad and inconsistent with the (10-1) peak widths.

The experiment was carried on for three of the four days of beamtime available to us, but despite the high number of surface preparation cycles carried out, the quality of the ARPES peaks did not improve. Therefore, we changed to the Te(10-10) sample to measure the dispersion of the bands perpendicular to the surface normal.

After two successful preparation cycles we could observe well-defined spectra with narrow widths. The dispersion along k_z was measured with photons of different energy ranging from 41.5 to 90 eV. From each angle-resolved spectrum a slice about normal emission was extracted and merged with the others. The data, presented in Fig. 2, allowed an independent determination of the inner potential, which we evaluated to be about 6 eV, consistent with the theoretical prediction by Murakami et. al [1] (as the bottom of valence band reference to vacuum level), but lower than the experimental data of Refs. 2 (10 eV) and Ref. 3. (13 eV)
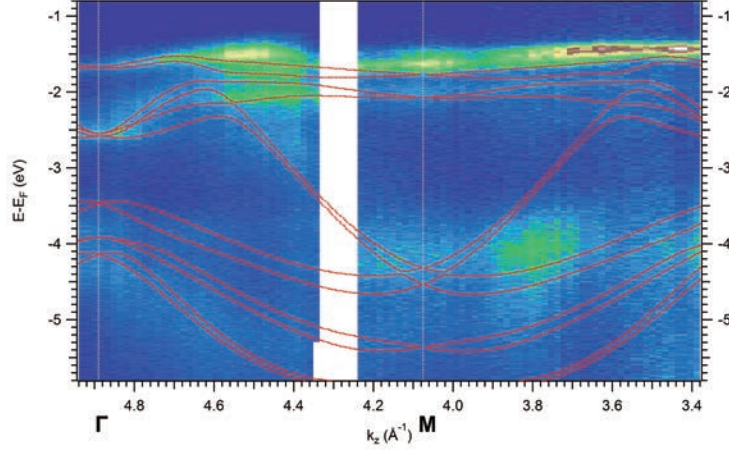

FIGURE 2. k_z-dispersion of Te along $\Gamma M \Gamma$ within the photon energy range 41.5 - 90 eV. The free electron final state approximation using an inner potential of $V_0 = 6$ eV was used to convert the photon energy to k_z-axis. Red lines represent band structure calculations from [1]. For aligning our ARPES data with the calculations along the binding energy axis, the topmost measured and the topmost calculated band were matched.

In Fig. 2 the experimental band dispersion is compared to the theoretical calculations of Murakami et al. [1] and the agreement between the two is fairly good. This is an indication that electronic correlations in Tellurium are weak and can be treated within the framework of the local-density and the GW approximation.

From the dispersion along k_z it is not possible to draw conclusions about the topological nature of Tellurium, since the states involved in the topological phase are located at the H point of the Brillouin zone, which is away from the ΓM direction mapped by the k_z dispersion measurements.

REFERENCES

1. *Weyl Node and Spin Texture in Trigonal Tellurium and Selenium,* Phys. Rev. Lett. 114, 206401 (2015)
2. *Clean Te surface studied by LEED*, Surf. Sci. Vol. 12, Issue 2 (1968)
3. *Surface structure of Te(10¯10) as determined from the analysis of low-energy-electron-diffraction intensities* Phys. Rev. B. 21, 4542 –(1980)

Evaluation of matrix element effects and extraction of spectral function in Sr_2RuO_4 by high-resolution ARPES

H. Iwasawa[a], Y. Yoshida[b], K. Shimada[c], Y. Aiura[b]

[a]*Diamond Light Source, Harwell Science and Innovation Campus, Didcot OX11 0DE, UK*
[b]*National Institute of Advanced Industrial Science and Technology, Tsukuba, Ibaraki 305-8568, Japan*
[c]*Hiroshima Synchrotron Radiation Center, Hiroshima University, Higashi-Hiroshima 739-0046, Japan*

Single layered ruthenium oxide (ruthenate), Sr_2RuO_4, is well-known as a representative spin-triplet superconductor (T_c~1.5 K) [1, 2]. Fermi surface (FS) of Sr_2RuO_4 consists of three cylindrical FS sheets, two electron-like β and γ sheets centered at the Γ point, one hole-like α sheet centered at the X point [see Fig. 1(a)], as established by different techniques such as de Haas van Alphen, ARPES, and LDA band-structure calculations. Surprisingly, the effective mass of Sr_2RuO_4 is strongly anisotropic as m_γ^*=5.5, $m_{\alpha,\beta}^*$=3-3.5 [1], and furthermore, it is not consistent with the fact that the α and β sheets are mainly derived from narrow Ru $4d_{yz,zx}$ bands and the γ sheet is from wide Ru $4d_{xy}$ band. It is, therefore, significantly important to examine the effective mass of each FS sheets experimentally. In our previous ARPES studies on the β and γ sheets of Sr_2RuO_4, we found that the electron-electron interaction is essential to understand not only the large-energy scale band renormalization but also the low-energy scale one due to the electron-boson interaction [3, 4]. In this work, we have performed high-resolution ARPES on the α sheet of Sr_2RuO_4 to fully understand the many-body effects on this material.

High-quality single crystals of Sr_2RuO_4 were prepared by the floating zone method with a self-flux technique (T_c ~ 1.36 K). ARPES experiments were measured at the linear undulator beamline (BL-1) of Hiroshima Synchrotron Radiation Center (HiSOR) using a Scienta R4000 electron analyzer. Clean and flat surfaces of the samples were obtained by cleaving *in situ* under ultra-high-vacuum conditions (2×10^{-10} Torr) at a low temperature (~30 K). Present ARPES data were taken with the photon energy of 65 eV at 30 K in the *p*-polarization and *s*-polarization geometries. Note that the photon energy was selected to observe the bottom of the Ru $4d_{yz}$ band.

Figures 1(b) and (c) show the ARPES images of Sr_2RuO_4 taken along the XMX line [red line in Fig. (a)] in the *p*-polarization and *s*-polarization geometries, respectively. In the *p*-polarization geometry, three electronic features can be observed; two bulk and surface derived α bands (α_B and α_S), and a flat band near the M point (k_x=0) just below the Fermi level. The α_S and flat bands can be well reproduced by the band structure calculations including the surface reconstruction that yields the rotations of the RuO_6 surface octahedral by ~6° [5]. In contrast, the *s*-polarization geometry, the α_S band disappear and the α_B can be observed selectively, especially in the negative k_x region. To estimate the band renormalization effects due to the electron-electron interaction, the energy distribution curves (EDCs) were extracted as shown in Fig. 1(d). The energy of the band bottom is independent of the polarization, and can be estimated as ~0.41 eV. This is almost the half-width compared with one of LDA band-structure calculations (~0.84 eV). The effective mass enhancement factor was thus estimated as 2.05 due to the electron-electron interaction with the coupling strength of λ_{el-el}~1.05. Present results may indicate an anisotropic large energy-scale mass enhancement as the large energy-scale mass enhancement was estimated to be ~3.0 for the β and γ bands. We will further examine the electron-boson interaction on the α band by performing a detailed self-energy analysis considering the present large energy-scale band renormalization effects.

REFERENCES

1. A. P. Mackenzie and Y. Maeno, Rev. Mod. Phys. **75**, 657 (2003).
2. Y. Maeno *et al.* J. Phys. Soc. Jpn. **81**, 011009 (2012).
3. H. Iwasawa *et al.*, Phys. Rev. Lett. **109**, 066404 (2012).
4. H. Iwasawa *et al.*, Sci. Rep. **3**, 1930 (2013).
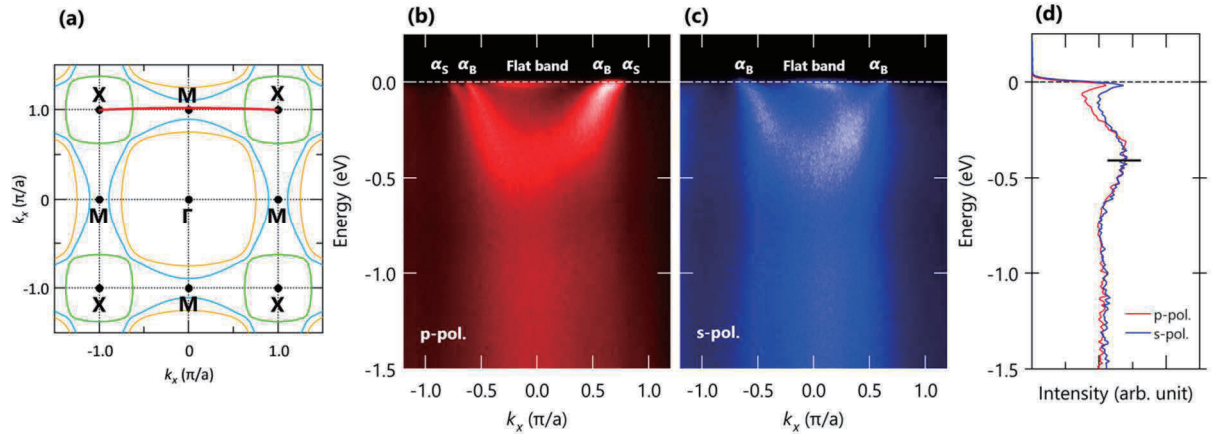5. K. M. Shen *et al.*, Phys. Rev. B **64**, 180502(R) (2001).

FIGURE 1. (a) Schematic Fermi surface of Sr_2RuO_4. (b) and (c) ARPES image along the XMX line [red line in panel (a)] from Sr_2RuO_4 taken with 65 eV at 30 K in the (b) *p*-polarization and (c) *s*-polarization geometries, respectively. (d) Energy distribution curves at the M point ($k_x = 0$).

Searching for topological quantum states in compounds in analogue to HgTe

Aiji Liang[a], Shengtao Cui[a], Zhongkai Liu[a] and Yulin Chen[a,b,c,d]

[a] *School of Physical Science and Technology, ShanghaiTech University, Shanghai, P. R. China*
[b] *Department of Physics, University of Oxford, Oxford, OX1 3PU, UK*
[c] *State Key Laboratory of Low Dimensional Quantum Physics, Department of Physics and Collaborative Innovation Center of Quantum Matter, Tsinghua University, Beijing 100084, P. R. China*
[d] *Hefei Science Center, CAS and SCGY, University of Science and Technology of China, Hefei, P. R. China*

The investigation on novel topological quantum states has become one of the most intensively studied topics in condensed matter physics [1-3]. HgTe, an inverted band gap semiconductor, is one of the starting materials for some topological insulators [1-5] gives hints to researchers to discover new topological quantum states via adiabatic transformation or isostructural consideration [6-8]. It was theoretically proposed recently, that a series of stable compounds which are isostructural to HgTe, host exotic topological quantum states with intriguing properties [8].

With high quality crystalline samples which are in analogue to HgTe as proposed [8], we carried out systematic Angle-resolved photoemission spectroscope (ARPES) on these compounds and obtained their electronic structures as demonstrated in Figure 1. A large scale of Fermi surface is shown in Fig. 1a. The symmetry and the size of the surface Brillouin zone determined by the Fermi surface patterns agree well with the proposed crystal structure [8]. A typical cut across Γ is extracted and shows that the Fermi surface pocket at Γ in Fig. 1a is hole like. The overall band structures in Fig. 1b show similarity to that of HgTe as expected. However, their hole dosing hampers the searching for exotic topological quantum states that reside above the present Fermi level [8]. Therefore, more electron dosed samples, acquired by subtle growth methods or *in situ* electron dosing techniques are needed to advance the exploring.
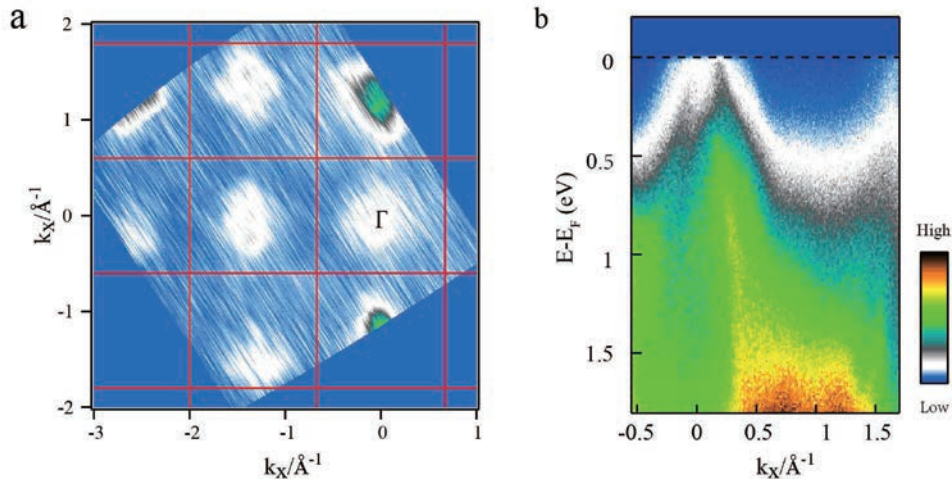

FIGURE 1. Basic Electronic structure of the HgTe analogue candidate compound. (a) Fermi surface covering several surface Brillouin zones with an integrated window of ±50 meV. The incident photon energy is 150 eV. (b) A typical cut crosses Γ along k_x direction. The incident photon energy is 80 eV.

In summary, we carried out systematic ARPES study on one of the proposed compounds which are in analogue to HgTe and host topological quantum states. The basic electronic structures are obtained and in good

agreement with calculation [8]. The more electron doped samples are needed to unveil the proposed topological quantum states which would be the route for future study.

REFERENCES

1. M. Z. Hasan & C. L. Kane, *Reviews of Modern Physics*, **82**, 3045-3065 (2010).
2. X. L. Qi & S. C. Zhang, *Reviews of Modern Physics*, **83**,1058-1105 (2011).
3. C. L. Kane & E. J. Mele, *Phys. Rev. Lett.* **95**, 146802 (2005).
4. B. A. Bernevig, T. L. Hughes & S.-C Zhang, *Science* **314**, 1757 (2006).
5. M. Konig *et al.*, *Science* **318**, 766 (2007).
6. E.-G. Moon *et al.*, *Phys. Rev. Lett.* **111**, 206401 (2013).
7. G. Xu *et al.*, *Phys. Rev. Lett.* **107**, 186806 (2011).
8. In preparation.

Observation of a k_z-dependent bulk electronic structure in ReSe$_2$

P. Eickholt[a], J. Noky[b], E.F. Schwier[c], K. Miyamoto[c], Ch. Datzer[a], M. Drüppel[b], P. Krüger[b], K. Shimada[c], M. Rohlfing[b], and M. Donath[a]

[a]*Westfälische Wilhelms-Universität Münster, Physics Institute, 48149 Münster, Germany*
[b]*Westfälische Wilhelms-Universität Münster, Institute of Solid State Theory, 48149 Münster, Germany*
[c]*Hiroshima Synchrotron Radiation Center Hiroshima University, Higashi-Hiroshima 739-0046, Japan*

Transition metal dichalcogenides (TMDCs) are heavily studied due to their fascinating optical and electronic properties and possible technical applications. ReSe$_2$ is a new material of the TMDC family which grows, unlike the well-known MoS$_2$, in a distorted 1T structure. Therefore, ReSe$_2$ is a triclinic system, which has only inversion symmetry and thus the lowest possible symmetry. Consequently, it has unique anisotropic properties which can be useful in future applications [1].
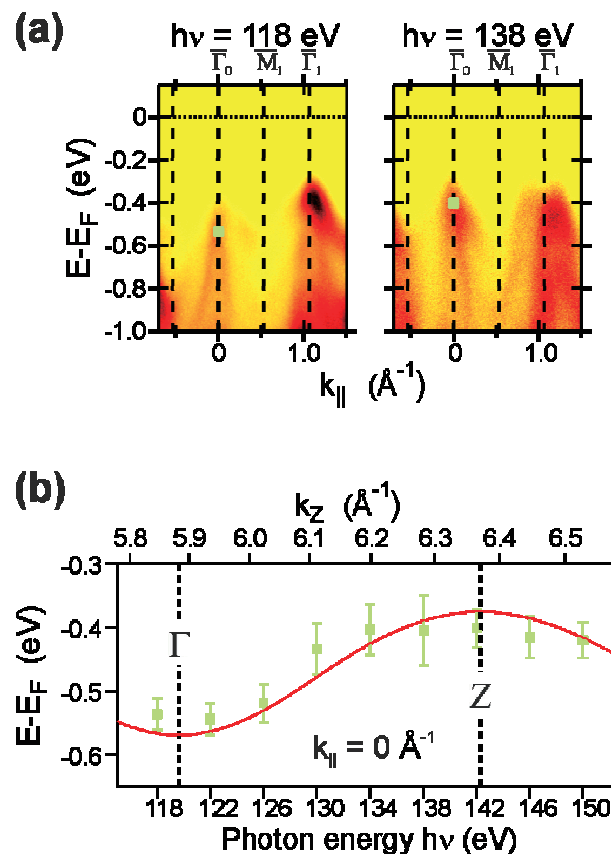

FIGURE 1. (a) ARPES measurements along the $\Gamma_0 M_1$-direction for photon energies of $h\nu$ =118 eV and $h\nu$ =138 eV. (b) Dispersion of the highest valence band at $k_\parallel$ = 0 Å^{-1} and along ΓZ. The determined positions are shown as green rectangles in (a). The red solid line is the calculated dispersion using a quasiparticle calculation.

One of the key features of popular TMDCs (MoS_2, WS_2, $MoSe_2$ and WSe_2) is their band gap, which leads to optical transitions in the visible range [2]. However, for optical transitions, a direct band gap is needed which these materials only have as a single layer. In contrast, $ReSe_2$ might be a direct-band-gap semiconductor even as a bulk material [3], though there is still an ongoing discussion about that [4]. Especially the position of the valence band maximum (VBM) is subject of current debate. Band structure calculations with and without quasiparticle corrections [5] show the VBM at different positions [3] in **k**-space, while the conduction band minimum is found at the Z point in both types of calculations.

In order to clarify the position of the VBM, we performed a photon-energy-dependent angle-resolved photoemission (ARPES) study of the occupied electronic structure. Together with inverse photoemission measurements, which gives us the information about the conduction band minimum, we will be able to show the size and type of the band gap of bulk $ReSe_2$. Additionally to the information about the band gap, ARPES allows us to probe the anisotropic properties of the electronic structure.

In Figure 1(a), ARPES measurements along the $\Gamma_0 M_1$-direction of the quasi-hexagonal surface Brillouin zone with two different photon energies are shown. We found the $\Gamma_0 M_1$-direction to be a distinctive direction within **k**-space with significantly flatter band dispersion than along other directions. This can be understood by the formation of so-called "diamond chains" along the a axis [6] of bulk $ReSe_2$, which makes this axis distinguishable within the atomic structure. The $\Gamma_0 M_1$-direction is perpendicular to that axis. Due to the low symmetry of the system, the measured electronic structure is asymmetric even around $k_{\parallel} = 0$ Å^{-1}. We find two possible VBMs, one for normal electron emission and another at a non-special point along the $\Gamma_0 M_1$-direction, which are separated by just a few meV.

Measurements with different photon energies are clearly showing k_z-dependent dispersion. This is presented in Figure 1(b), where the position of the highest valence band at $k_{\parallel} = 0$ Å^{-1} along ΓZ is displayed as a function of the used photon energy. With the assumption of nearly-free-electron final states, we estimate k_z [7] and compare our results with the calculated dispersion. While the quasiparticle calculation (red line in Figure 1 (b)) is in excellent agreement with our data, a calculation without quasiparticle calculation (not shown) predicts a dispersion of only a few meV along ΓZ in contrast to our data. Thus, the dispersion of the highest valence band along ΓZ is a strong indication of the importance of quasiparticle corrections in calculations for this system and consequently for the VBM located at the Z-point.

REFERENCES

1. S. Yang *et al.,* Nanoscale **6**, 7226 (2014)
2. A. Splendiani *et al.,* Nano Lett. **10**, 1271 (2010)
3. A. Arora *et al.,* Nano Lett. **17**, 3202 (2017)
4. D. Wolverson *et al.,* ACS Nano **8**, 11154 (2014)
5. M. Rohlfing, Phys. Rev. B **82**, 205127 (2010)
6. H.-J. Lamfers *et al.,* J Alloys Compd. **241**, 34 (1996)
7. A. Damascelli *et al.,* Physica Scripta **T109**, 61 (2004)

The diluted magnetic semiconductor $Ba_{1-x}K_x(Zn_{1-y}Mn_y)_2As_2$ studied byangle-resolved photoemission spectroscopy

Yong HU[a], shaolong HE[b] and Xingjiang ZHOU[a]

[a]*National Lab for Superconductivity, Beijing National Laboratory for Condensed Matter Physics, Institute of Physics, Chinese Academy of Sciences, Beijing100190, China*
[b] *Ningbo Institute of Materials Technology and Engineering, Chinese Academy of Sciences, Ningbo, Zhejiang 315201, China*

Keywords: dilute ferromagnetic semiconductor

Over the decade, the field of diluted magnetic semiconductors (DMSs) has evolved into an important branch of materials science[1]. The remarkable features and functionalities, for instance, the presence of spin current (e.g., spin injection devices[2][3], current-induced domain displacement [4], the control of magnetism by electric fields[5][6] and electric currents[7][8], are expected to be beneficial for future spintronic devices[9][10]. In spite of extensive studies on these compounds combining of the properties of ferromagnets and semiconductors, however, the mechanism behind the ferromagnetism is still vigorously debated[11].

A representative event was the report on carrier-mediated ferromagnetism of manganese-doped II-II-V DMSs compounds, which is isostructural to '122' iron-based superconductors. In the $Ba_{1-x}K_x(Zn_{1-y}Mn_y)_2As_2$ systems, holes and spin doping are induced separately, which simplifies the theoretical understanding and experimental treatment of carrier-induced ferromagnetism in DMSs for three interrelated reasons. First, Mn ions isovalent substituted for Zn that avoids trouble of mixed charged states for Mn. Second, charge is induced by doping potassium into the Ba sublayer, which makes it's possible to independently control the concentration of charge carriers and magnetic elements. Third, interstitial Mn is absent in this case so that antiferromagnetical coupling between interstitial and substitutional position Mn can be natural ruled out in this DMSs systems. Furthermore, high quality single crystals of the $Ba_{1-x}K_x(Zn_{1-y}Mn_y)_2As_2$ systems provide an advantageous platform for experimental study.

We have obtained systemic ARPES data on dilute magnetic semiconductor of $Ba_{1-x}K_x(Zn_{1-y}Mn_y)_2As_2$ and $Ba_{1-x}K_xZn_2As_2$ at BL-1 last year, in order to systemically compare the electronic of the new family of the dilute magnetic semiconductor. Besides the results on $Ba_{1-x}K_x(Zn_{1-y}Mn_y)_2As_2$ and $Ba_{1-x}K_xZn_2As_2$, it's also necessary to further study the newly grown high-quality single crystals $Ba(Zn_{1-y}Mn_y)_2As_2$ and $BaZn_2As_2$. Currently, we are working closely with theoretical group to explain the ARPES results on these new dilute magnetic semiconductors.
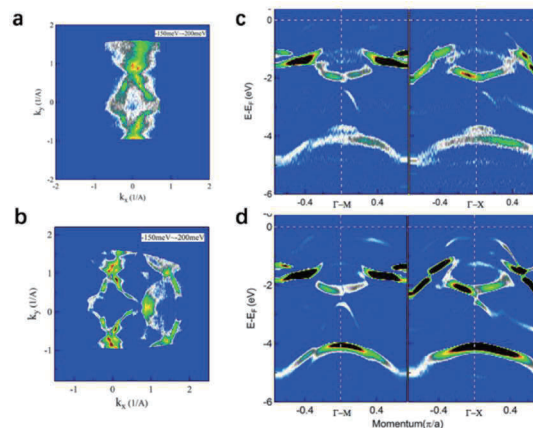

FIGURE 1. Constant energy contour and band structure of $Ba(Zn, Mn)_2As_2$ and $BaZn_2As_2$ taken with hv=34eV. (a),(b) Integrated spectral intensity as a function of momentum for$Ba(Zn, Mn)_2As_2$ and $BaZn_2As_2$, respectively. The images are obtained by integrating the spectral weight over a small energy window [-150meV, 200meV]. (c), (d) The corresponding electronic structures of$Ba(Zn, Mn)_2As_2$ and $BaZn_2As_2$ along Γ-M and Γ-X. The images are obtained by the second derivative of the original data with respect to the energy.

Figure 1 shows ARPES spectra taken with hv=34eV. Figure 1(a), (b) show the "Fermi surface" of Ba(Zn, Mn)$_2$As$_2$ and BaZn$_2$As$_2$, respectively, which are obtained by integrating over a small energy window ranging from -150meV and -200meV. The band dispersions taken at temperature of 30K along the high symmetry directions labeled as Γ-M and Γ-X in figure 1 (c) and (d).
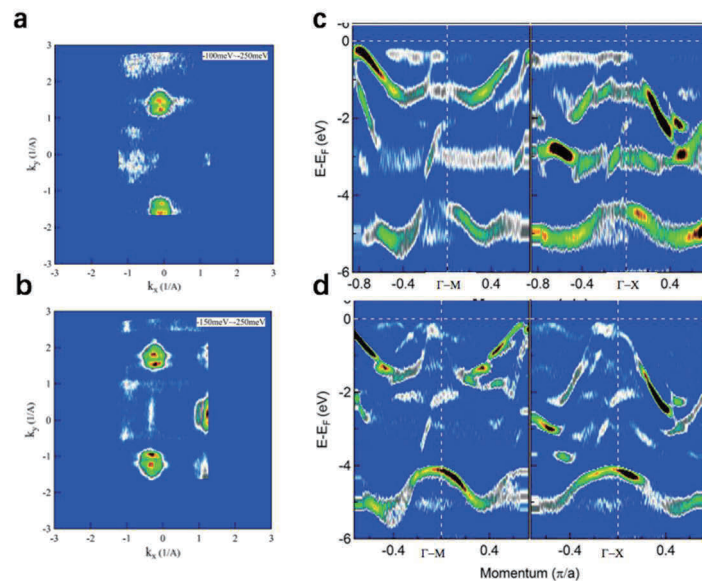

FIGURE 2. Constant energy contour and band structure of Ba(Zn, Mn)$_2$As$_2$ and BaZn$_2$As$_2$ taken with hv=95eV. (a), (b) Integrated spectral intensity as a function of momentum forBa(Zn, Mn)$_2$As$_2$ and BaZn$_2$As$_2$, respectively. The images are obtained by integrating the spectral weight over a small energy window [-150meV, 250meV]. (c), (d) The corresponding electronic structures ofBa(Zn, Mn)$_2$As$_2$ and BaZn$_2$As$_2$ along Γ-M and Γ-X. The images are obtained by the second derivative of the original data with respect to the energy.

In order to clarify the Mn 3d-derived states, we try to change photon energy. Figure 2 shows ARPES results taken with, hv=95eV, keeping the sample temperature at 30K during the measurements. Constant energy mapping at E$_F$ is shown in Fig. 2 (a) and (b), which are obtained by integrating over a energy window ranging from -150meV and -250meV for Ba(Zn$_{1-y}$Mn$_y$)$_2$As$_2$and BaZn$_2$As$_2$, respectively. Comparing with figure 2(c) and (d), we observe an nondispersive intensity due to Mn 3d states around 3eV blew fermi level in Ba(Zn$_{1-y}$Mn$_y$)$_2$As$_2$, which is similar with our previous results inBa$_{1-x}$K$_x$(Zn$_{1-y}$Mn$_y$)$_2$As$_2$.

REFERENCES

1.Dietl, T. A ten-year perspective on the diluted magnetic semiconductors and oxides. Nature Mater. 9, 965-974 (2010).

2. Ohno, H. et al. Electrical spin injection in a ferromagnetic semiconductor heterostructure. Nature 402, 790-792 (1999)

3. Mattana, R. et al. Electrical detection of spin accumulation in a p-type GaAs quantum well. Phys. Rev. Lett. 90, 166601 (2003)

4. Yamanouchi, M., Chiba, D., Matsukura, F. \& Ohno, H. Current-induced domain-wall switching in a ferromagnetic semiconductor structure. Nature 428, 539-542 (2004)

5. Ohno, H. et al. Electronic-field control of ferromagnetism. Nature 408, 944-946 (2000)

6. Chiba, D. et al. Magnetization vector manipulation by electric field. Nature Phys. 455, 525-518 (2008)

7. Watanabe, M. Okabayashi, J., Toyao, H., Yamaguchi, T & Yoshino, J. Current-driven magnetization reversal at extremely low threshold current in (Ga,Mn)As-based double-barrier magnetic tunnel junctions. Appl. Phys. Lett. 92, 082506 (2008)

8. Chernyshov, A. et al. Evidence for reversible control of magnetization in a ferromagnetic material by means of spin-orbit magnetic field. Nature Phys. 5, 656-659 (2009)

9. Žutić, I., Fabian, J. & Sarma, S. D. Spintronics: Fundamentals and applications. Rev. Mod. Phys. 76, 323-410 (2004)

10. Jungwirth, T. et al. Spin-dependent phenomena and device concepts explored in (Ga,Mn)As. Rev. Mod. Phys. 86, 855-896 (2014)

11. Jungwirth, T. et al. Character of states near Fermi level in (Ga,Mn)As: Impurity to valence band crossover. Phys. Rev. B 76, 125206 (2007)

12. Ohno, H. et al. (Ga,Mn)As: A new diluted magnetic semiconductor based on GaAs. Appl. Phys. Lett. 69, 363-365 (1996)

Resonant photoemission and inverse photoemission studies of electronic ferroelecctricity YbFe$_2$O$_4$

T. Fukura[a], T. Wakita[a,b], K. Fujiwara[a], N. Ikeda[a], H. Okazaki[c], T. Nagata[d],
H. Sato[e], H. Namatame[e], M. Taniguchi[e], K. Terashima[a,b],
Y. Muraoka[a,b] and T.Yokoya[a,b]

[a]*Graduate School of Natural Science and Technology, Okayama University, Okayama 700-8530, Japan*
[b]*Research Institute for Interdisciplinary Science, Okayama University, Okayama 700-8530, Japan*
[c]*Japan Synchrotron Radiation Research Institute, SPring-8, Hyogo, 679-5198, Japan*
[d]*College of Science and Technology, Nihon University, Chiba 274-8501, Japan*
[e]*Hiroshima Synchrotron Radiation Center, Hiroshima University, Hiroshima 739-0046, Japan*

Keywords: Resonant photoemission spectroscopy, Resonant inverse photoemission spectroscopy, Charge-order,
Electronic ferroelectricity

Electronic ferroelectrics have spontaneous polarization induced by breaking inversion symmetry of charge or electrons. This kind of materials has attracted much attention because the origin of ferroelectricity is different from that of conventional displacive type ferroelectricity.

YbFe$_2$O$_4$ is a member of RFe$_2$O$_4$ (R:Y, Dy-Lu) family that is known as the mixed valence compound[1]. This material exhibits several interesting physical properties, for example, electronic ferroelectricity, ferrimagnetism, magnetoelectoric effect and so on. These originate from charge- and spin-orderings in double Fe-O layers. Though electronic correlation of this system is known to play a key rule, its electronic structure associated with charge-ordered (CO) state has not been clarified, yet[2].

In this study, we examined Fe $3d$-derived occupied and unoccupied states of YbFe$_2$O$_4$ using resonant photoemission and resonant inverse photoemission spectroscopy (RIPES) across the Fe $3p(2p)$-$3d$ threshold at room temperature. In comparison with Fe $M_{2,3}(L_3)$-edge XAS, we could identify Fe^{2+} and Fe^{3+} $3d$-derived resonant enhancement, and provide the iron-valence dependent energy diagram of YbFe$_2$O$_4$.

Figure 1 shows Fe $3d$ partial density of states (pDOS) obtained from RIPES and the results of XAS O K-edge[3] and GGA+U (U_{eff} = 4.61 eV) calculation[4]. XAS measurement, with the help of cluster calculation, and GGA+U calculation reported that Fe^{3+} $3d$ pDOS locates near the Fermi level. However, The present RIPES shows that Fe^{2+} $3d$ pDOS, as well as Fe^{3+} $3d$ pDOS, constitutes the lowest unoccupied state. We attribute the inconsistent to the lack of essential interaction in GGA+U calculation. We found that our results can be explained successfully by introducing inter-site Coulomb interaction and a proper CO model. The present spectroscopic studies lead to further understanding of the physical properties of YbFe$_2$O$_4$ and the origin of the CO state.

REFERENCES

1. N. Iekeda *et al*., Nature **436**, 1136 (2005).
2. J. de Groot *et al*., Phys. Rev. Lett. **108**, 187601 (2012).
3. K. –T. Ko *et al*., Phys. Rev. Lett. **103**, 207202 (2009).
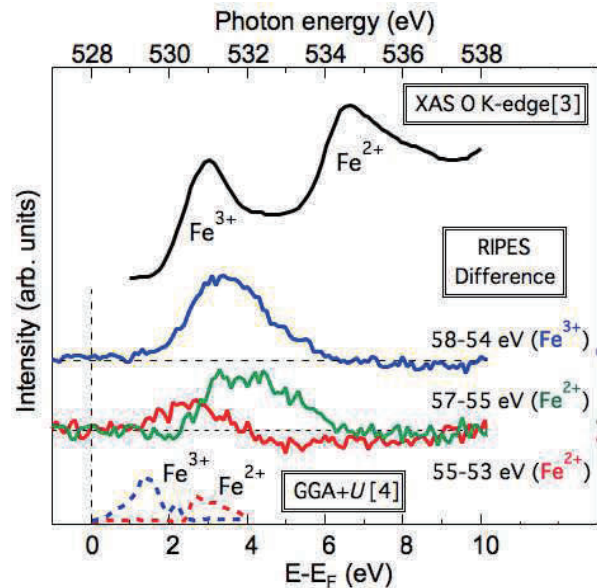4. H. J. Xiang and M. -H. Whang, Phys. Rev. Lett. **98**, 246403 (2007).

FIGURE 1. The Fe $3d$ pDOS obtained from RIPES and the results of XAS O K-edge[3] and GGA+U (U_{eff}= 4.61 eV) calculation[4].

Current activities of research and education on BL-5 (FY2016)

T. Yokoya[a,b,c], T. Wakita[a], K. Terashima[a] and Y. Muraoka[a,c]

[a]*Research Institute for Interdisciplinary Science (RIIS), Okayama University*
[b]*Graduate School of Natural Science and Technology, Okayama University*
[c]*Research Laboratory for Surface Science (RLSS), Okayama University*

Keywords: photoemission spectroscopy, photoelectron emission microscopy

Beamline 5 (BL5) and the experimental stations were installed in order to promote research on condensed matter physics, especially for surface science, with the bilateral agreement between Okayama University and Hiroshima University. Here, we present an overview of our recent research and educational activities on BL5.

Our beamline has two experimental stations in a tandem way. The first station is equipped with an angle-resolved photoemission spectrometer (ARPES), a low energy electron diffraction (LEED) apparatus and an X-ray source. The hemispherical analyzer of ARPES spectrometer (HA54, VSW) has a mean radius of 50 mm and is mounted on a twin axis goniometer in ultra-high vacuum chamber. Using this goniometer, one can perform ARPES and photoelectron diffraction (PED) measurements. It is also possible to perform resonant photoemission spectroscopy (RPES) measurements by using photon energy tunability of synchrotron radiation with X-ray absorption spectroscopy (XAS) measurement. With the X-ray source (XR2E2, FISONS), we can perform an X-ray photoelectron spectroscopy (XPS) measurement for the chemical state analysis and the PED. At the second station, we have installed a photoelectron emission microscope (PEEM, 'PEEM III', Elmitec). PEEM provides a magnified image of lateral intensity distribution of photo-emitted electrons from a sample surface. The spatial resolutions are several ten nanometers with Hg lamp and a few micrometers with synchrotron radiation. The sample is transferred between the ARPES and the PEEM chamber *in-situ*, and one can perform measurements at both stations for the same sample.

In the recent researches on BL-5, we have concentrated our attention on functional materials, most of which has been synthesized by groups of Okayama University. For examples, we have studied the electronic structure of potassium doped aromatic molecule (K_x picene) [1], iron-based superconductor ($FeSe_xTe_{1-x}$) [2], transition metal di-oxide films such as VO_2 thin films which exhibits a first-order metal-to-insulator transition at 340 K [3], CrO_2 thin films which are known as a half-metallic material [4], and TaO_2 film which is stabilized with a new technique developed in our group [5]. We are also studying the electronic structures of a high quality boron doped diamond film which shows a signature of the highest superconducting transition temperature of 25 K [6] and a high quality single crystal of $YbFe_2O_4$ which is one of multiferroic materials [7], by utilizing RPES at B-K and Fe-$M_{2,3}$ edges, respectively. The photoemission studies of boron doped diamond and the multiferroic material will be presented separately.

We have used the BL-5 for education activity as well, for example, practical education for undergraduate students of Okayama University. The students have an opportunity to study the synchrotron radiation mechanism and to experience XPS measurement tha is very useful for the surface science research. From 2014, we have been in charge of the practical lecture/experiment course using the beamline-end stations in HiSOR for both graduate school students of Hiroshima and Okayama Universities.

REFERENCES

1. H. Okazaki *et al.*, *Phys. Rev* **82**, pp. 195114 (5 pp.) (2010).
2. Y. Yoshida *et al.*, *J. Phys. Soc. Jpn* **78**, pp. 034708 (4 pp.) (2009).
3. K. Saeki *et al.*, *Phys. Rev* **80**, pp. 125406 (5 pp.) (2009).
4. Y. Muraoka *et al.*, *MRS Proceedings* **1406** (2012).
5. Y. Muraoka *et al.*, *Thin Solid Films* **599**, pp. 125-132 (2016).
6. H. Okazaki *et al.*, *Appl. Phys. Lett* **106**, pp. 052601 (5 pp.) (2015).
7. K. Fujiwara *et al.*, *Trans. Mater. Res. Soc. Jpn.* **41**, pp. 139-142 (2016).

XPS study of TaO$_2$ thin films

Y. Muraoka[a], Y. Fujimoto[b], M. Kameoka[c], Y. Matsuura[b], M. Sunagawa[a],

K. Terashima[a], T. Wakita[a], T. Yokoya[a]

[a]*Research Institute for Interdisciplinary Science, Okayama University,*
[b]*Graduate School of Natural Science and Technology, Okayama University*
[c]*Faculty of Science, Department of Physics, Okayama University*

Keywords: XPS, TaO$_2$, Thin film

X-ray photoemission spectroscopy (XPS) is a powerful tool to study the oxidation states of constituent metal ions in transition oxides. One of target compounds for the XPS study may be TaO$_2$ thin films which are recently prepared using rutile-type NbO$_2$ template layers on Al$_2$O$_3$(0001) substrates [1]. TaO$_2$ has attracted attention in connection with VO$_2$ and NbO$_2$, which show a metal-insulator transition at 67 and 807 ºC, respectively [2-4]. Before performing the detailed study of physical properties, it is beneficial to characterize this film, especially oxidation state of Ta ions. In this work we perform the XPS measurements of TaO$_2$ thin films to examine the oxidation state of Ta ions in the film.

TaO$_2$ thin films were prepared using NbO$_2$ template layers on Al$_2$O$_3$(0001) by a pulsed laser deposition (PLD) technique. The films were found from four-circle XRD measurements to be a (100)-oriented tetragonal TaO$_2$ epitaxially grown on the NbO$_2$ template layers. XPS measurements were carried out on the beamline BL-5, at the Hiroshima Synchrotron Radiation Center in Hiroshima University with non-monochromatic Mg Kα X-ray source ($h\nu$ = 1253.6 eV). For XPS samples, very thin amorphous NbO$_x$ (2-3 nm) films were coated at 25 ºC in the PLD chamber to prevent the oxidation of the film surface. Ta 4f core-level spectra were measured under an ultrahigh vacuum of ~10^{-7} Pa using a VSW hemispherical analyzer. The total energy resolution was about 1.1 eV. The binding energy of the films was corrected using the peak position of Ta 4f core-level spectra, which were measured with synchrotron radiation and whose Fermi level position was determined by measuring the molybdenum spectra. Before measurements, the films were annealed at 120 °C under ultrahigh vacuum (~10^{-6} Pa) for 10 min to obtain a clean surface.

Figure 1 shows the Ta 4f core-level spectrum of the film. The spectrum shows the peak structure at a binding energy of ~ 27 eV and a shoulder around 25 eV, suggesting the presence of at least two kinds of valence states of Ta ions in the film. A fit of the spectral was performed and the results are shown in Figure 1 (solid line). The fit of the experimental spectrum was achieved with two components. One component at a lower binding energy (around 25 eV) originates from the Ta^{4+} valence state [5,6], thus supporting the formation of TaO$_2$ in the film. The other component at around 27 eV was attributed to the Ta^{5+} valence state [5,6]. This indicates the presence of not only TaO$_2$ but also Ta$_2$O$_5$ in the film. The amount of Ta^{4+} and Ta^{5+} states was estimated from the peak areas to be 14 and 86 %, respectively.

The results from the XPS measurements do not seem to be consistent with those from the XRD measurements, where only the epitaxial grown TaO$_2$ was
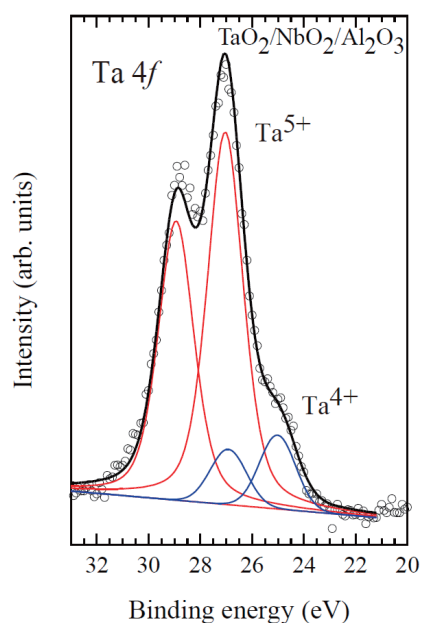

FIGURE 1. Ta 4f core-level spectrum for TaO$_2$/NbO$_2$/Al$_2$O$_3$. The solid line through the data is the fit resulting from the sum of the two-labeled components.

observed. A possible interpretation for this inconsistency is that an amorphous Ta_2O_5 layer is formed at the surface of the film, and the amount of Ta_2O_5 decreases on going toward the innermost portion of the film. The results of XPS and XRD measurements suggest that the film is composed of TaO_2 with an amorphous Ta_2O_5 layer at the surface as shown in Figure 2.
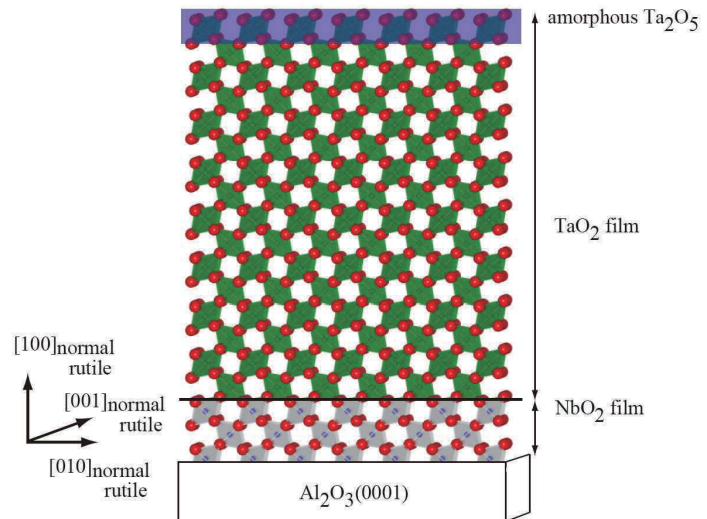

FIGURE 2. Schematic illustration of $TaO_2(100)/NbO_2(100)/Al_2O_3(0001)$.

REFERENCES

[1] Y. Muraoka et al., Thin Solid Films **599,** 125 (2016).
[2] F. J. Morin, Phys. Rev. Lett. **3,** 34 (1959).
[3] G. Bélanger, J. Destry, and G. Perluzzo, Can. J. Phys. **52,** 2272 (1974).
[4] T. Sakata, K. Sakata, and I. Nishida, Phys. Stat. Sol. **20,** K155 (1967).
[5] J. G. S. Moo, Z. Awaludin, T. Okajima, and T. Ohsaka, J. Solid State Electrochem. **17,** 3115 (2013).
[6] H. Demiryont, J. R. Sites, and K. Geib, Appl. Opt. **24,** 490 (1985).

Developments of helium path apparatus using a thin film window: soft x-ray spectroscopy of samples under atmospheric pressure

Makina Kamiyama[a], Noriko Yoshimura[a], Hiroaki Yoshida[b,c], Yuka Horikawa[a, d] and Takashi Tokushima[d]

[a]*Physics and Informatics, Faculty of Science, Yamaguchi University*
1677-1 Yoshida, Yamaguchi, Yamaguchi, Japan 753-8512
[b]*Department of Physical Science, Graduate School of Science, Hiroshima University*
1-3-1 Kagamiyama, Higashi-Hiroshima, Hiroshima, Japan 739-8526
[c]*Hiroshima Synchrotron Radiation Center, Hiroshima University*
2-313 Kagamiyama, Higashi-Hiroshima, Hiroshima, Japan 739-0046
[d]*RIKEN/SPring-8 center, 1-1-1 Koto, Sayo, Hyogo, Japan 679-5148*

Soft x-ray absorption experiments are normally performed in a vacuum environment to avoid light attenuation by air. Because of a strong absorption by nitrogen and oxygen atoms, transmission intensity of soft x-rays in air is less than 1 % for 5 mm of light path from N 1s absorption edge (around 400 eV) to around O1s absorption edge (around 530eV). However, transmission for 5mm reach over 90% by exchanging air by helium gas. This technique is well known and so called helium path and is frequently used in hard x-ray experiments. Although there are many possible applications on measurements of wet samples, applications of helium environments in soft x-rays (around 100-1000 eV) are still small in number.

For experiments at synchrotron light sources, we need to connect helium environments and high vacuum condition of the beamline. Simple way is putting separator window between them. However, It was not easy because soft x-ray need thin film thinner than several hundred nanometers for high transparency. Recently, high quality silicon nitride (SiN) membrane made from Si wafer, which is around 100nm in thickness and applicable to widow for soft x-rays, is available commercially. High temperatures cell, which use silicon nitride window, aims to observe catalytic reaction by x-ray absorption and emission spectroscopy were reported [1, 2]. There is also windowless approach using a differential pumping system [3].

Over the past decade, we have developed a liquid flow cell, which use thin film window to separate vacuum and liquid samples, and studied electronic structure of liquids by means of soft x-ray spectroscopy [4-6]. Because we recognized the effectiveness of this thin film as a separator window between vacuum and atmosphere through joint research of high temperature cell [2], we have also started developments of simple helium path apparatus for soft x-ray measurements of samples under atmospheric pressure. Here we report designs and developments of simple helium path apparatus for soft x-ray measurements of samples under atmospheric pressure
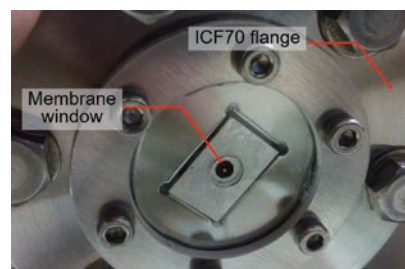

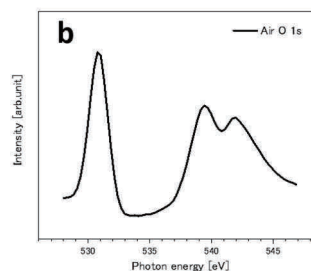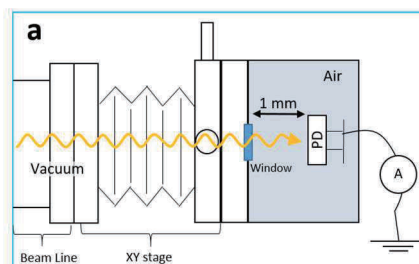**FIGURE 1.** Picture of a membrane window and a window holder.

FIGURE 2. (a) Schematic drawing of the window holder connected to the experimental chamber of BL6. (b) O1s absorption spectra of oxygen in air.

using SiN membrane as a window. We also report results of test measurements performed at HiSOR BL6 beamline[7].

Fig.1 shows a picture of 1st prototype of window holder (type 1). We have used 100nm thick membrane window with 0.5mm×0.5mm opening on φ3mm Si frame made by silicon nitride (NT050C, Norcada, Canada). The membrane window chip was glued on metal plate with center hole and mount on holder made on ICF70 flange. Fig.2(a) shows schematic drawing of the window holder connected to the experimental chamber of BL6[7]. To adjust window position to beam axis, the window holder was connected with XY stage to move vertically and horizontally. By placing photodiode (Opto diode Corp, AXUV100G) in the downstream of the beam after the window, one can easily find beam axis by checking current from photodiode. This setup is also useful to observe absorption of gas by transmittance measurement. Fig.2(b) shows absorption spectra of O1s region for oxygen in the air.

Fig.3(a) shows schematic drawing of setup for x-ray absorption measurement. A powder sample was put on the sample plate by carbon conductive adhesive tape, and was connected to picoammeter to measure sample currents. Photodiode (Opto diode Corp, AXUV100G) to detect soft x-ray fluorescence was placed near the sample. Incident beam reaching sample position is expected to be about 90% of intensity at surface of the window for soft x-rays of O1s absorption region by considering length of light path form window to sample in helium was about 14mm. Fig.3(b) and (c) shows obtained signal for powder glycine by sample current and fluorescence yield respectively. Although intensity of signal is quite low, edge structure of absorption in O1s region was observed.

Since development of the window holder (type 1) was completed successfully, revised version of window holder (type 2) was developed. We have used the same silicon nitride window, but was glued on a metal pipe with φ3mm outer diameter. Since the window is placed on the tip of pipe, one can use free space around tube to mount detectors and the sample. Fig.4(a) shows picture of window holder (type 2). Fig.4(b) shows fluorescence yield spectra of powder glycine measured using the type 2 window holder. For the type 2 holder, sample is possible to locate within a few millimeters from the window. In addition, photodiode detector is also located near the sample. Signal to noise ratio becomes better compared to type 1 setup.

We have successfully measured O1s FY spectra of solid sample under atmospheric helium environment using newly developed helium path apparatus. We are planning further investigation of samples under atmospheric pressure using this apparatus.
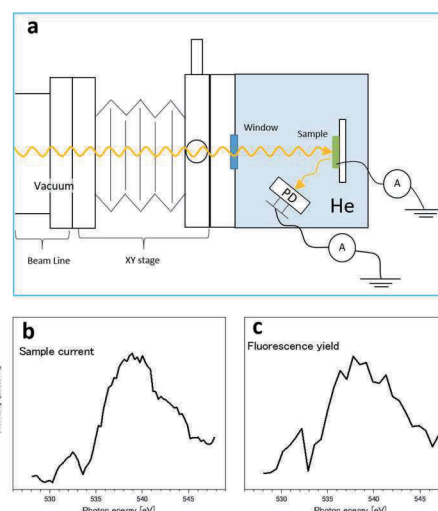

FIGURE 3. (a) Schematic drawing of setup for x-ray absorption measurements. (b) Obtained spectra for powder glycine by sample current. (c) Obtained spectra by fluorescence yield.
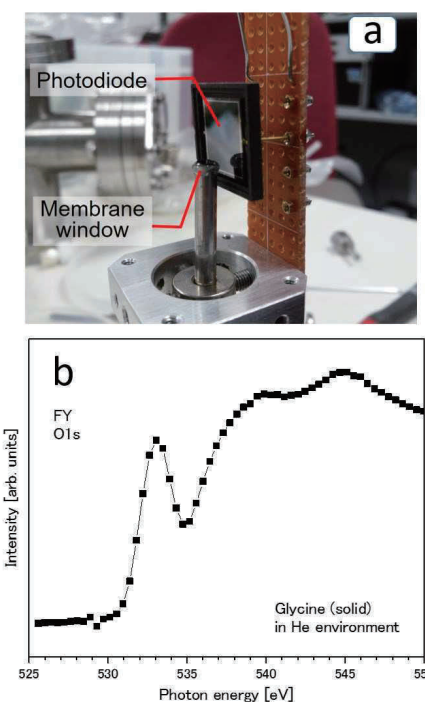
FIGURE 4. (a) Picture of window holder (type 2). A membrane window and a photodiode for detection of fluorescence yield are indicated by labels. (b)Obtained fluorescence yield spectra of solid glycine.

REFERENCES

1. H. Zhang, W.C. Wang, P.A. Glans *et al.*, J. Elec. Spectrosc. Relat. Phenom. **197**, 118 (2014).
2. R. Oike, Y. Okamoto, T. Tokushima *et al.*, Electrochemistry **84**, 793 (2016).
3. Y. Tamenori, Journal of Synchrotron Radiation **17**, 243 (2010).
4. Y. Horikawa, T. Tokushima, Y. Harada *et al.*, Phys. Chem. Chem. Phys. **11**, 8676 (2009).
5. T. Tokushima, Y. Harada, O. Takahashi *et al.*, Chem. Phys. Lett. **460**, 387 (2008).
6. 徳島高, 原田慈久, 辛埴, 日本物理学会誌 **63**, 852 (2008).
7. H. Yoshida, Y. Senba, T. Goya *et al.*, J. Elec. Spectrosc. Relat. Phenom. **144–147**, 1105 (2005).

Soft x-ray absorption measurements under helium environment at HiSOR BL6

Noriko Yoshimura[a], Makina Kamiyama[a],
Hiroaki Yoshida[b,c], Yuka Horikawa[a,d] and Takashi Tokushima[d]

[a]*Physics and Informatics, Faculty of Science, Yamaguchi University*
1677-1 Yoshida, Yamaguchi, Yamaguchi, Japan 753-8512
[b]*Department of Physical Science, Graduate School of Science, Hiroshima University*
1-3-1 Kagamiyama, Higashi-Hiroshima, Hiroshima, Japan 739-8526
[c]*Hiroshima Synchrotron Radiation Center, Hiroshima University*
2-313 Kagamiyama, Higashi-Hiroshima, Hiroshima, Japan 739-0046
[d]*RIKEN/SPring-8 center, 1-1-1 Koto, Sayo, Hyogo, Japan 679-5148*

Keywords: ambient pressure, helium environment, soft x-rays, x-ray absorption spectroscopy

As demonstrated in modern experiments of solid state physics like photoemission spectroscopy, electronic state observation is useful tool to understand material properties. Information of electronic state is also important for chemistry since chemical reaction can be considered to connect closely to variation in molecular orbitals, i.e. electronic structure. However, photoemission is normally not applicable to the samples under atmospheric pressure. There are large demands on measurements of samples under atmospheric pressure, and many attempts to develop new method or technology are ongoing recently. We have also developed a liquid flow cell, which uses thin film window to separate vacuum and liquid samples under atmospheric pressure, and studied electronic structure of liquid and solutions by means of soft x-ray spectroscopy over the past decade [1-3].

Except for experiments using liquid cells such as mentioned above, the absorption experiments of soft x-ray region are normally performed under vacuum environments to avoid absorption of air. Because of strong K-edge absorption of nitrogen and oxygen, 5 mm of light path in air is enough to decay less than 1% in intensity for soft x-rays from N 1s absorption (around 400eV) above O 1s absorption (around 530eV). However, transmission is expected to be improves to over 90% by exchanging air by helium gas in the same situation. This technique is well known and so called helium path, and frequently used in experiments in much higher energy x-ray region compared to soft x-rays.

Although there are many possible applications on measurements of wet samples, applications using helium environments for soft x-ray region (around 100-1000eV) are still small in number. Recently, high quality silicon nitride membrane made from Si wafer, which is around 100nm in thickness and applicable to window for soft x-rays, is commercially available. High temperatures cell, which uses the silicon nitride window, aims to observe catalytic reaction by using x-ray absorption and emission spectroscopies were developed [4, 5]. Because we recognized the effectiveness of the thin film as a separator window between vacuum and atmosphere through joint research of high temperature cell [5], we have started developments of simple helium path apparatus for soft x-ray measurements of samples under atmospheric pressure. Here we report a preliminary results obtained using the new helium path apparatus.

Experiments were performed at soft x-ray beamline BL6 in HiSOR[6]. Fig.1 shows window holder with a photodiode (Opto diode Corp, AXUV100G) to
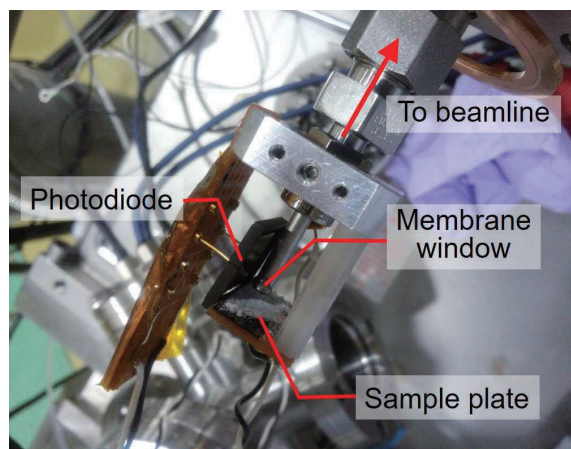

FIGURE 1. Picture of sample setup including a window holder, a photodiode to detect fluorescence yield and a sample plate.

detect fluorescence yield and a sample plate to mount the sample. We have used 100 nm thick membrane window with 0.5 mm × 0.5 mm opening on φ3mm Si frame made of silicon nitride (NT050C, Norcada, Canada). The membrane window chip was glued on a tip of metal pipe with φ3mm outer diameter, and the pipe was connected by tube fitting to an ICF70 flange. Sample was mounted on the copper plate using a carbon conductive adhesive tape and the plate was placed near the tip of window holder. Then, this set up was covered with a chamber to fill helium gas. Exchange of air by helium gas was performed by flowing helium gas from gas inlet placed on the top of the chamber. Output signal of photodiode was amplified by a preamplifier circuit placed near the photodiode in chamber filled with helium gas, and measured by a combination of voltage to frequency converter and frequency counter.

We have chosen solid benzoic acid and sodium benzoate as test samples. Vapor pressure of benzoic acid is 0.16 Pa (25 °C), hence it is not possible to measure this sample in vacuum condition due to its vaporization. Fig. 2 shows O 1s fluorescence yield spectra of powder benzoic acid and sodium benzoate under helium environment. It took about 10min to obtain each spectra. Absorption spectra of acetic acid (gas phase [7] and liquid phase [8]) are also plotted as

FIGURE 2. Preliminary result of FY spectra of benzoic acid and sodium benzoate in oxygen 1s region under helium gas at atmospheric pressure.

references. Clearly, energy resolution is not good because of widely opening slit of the beamline. However a peak structure assignable to π* orbital of carboxyl group is observed.

Difference between benzoic acid and sodium benzoate is appeared as a peak shift of lowest excitation. Sodium benzoate is the sodium salt of benzoic acid. Therefore evident difference between two sample concerning oxygen site is protonation and deprotonation of carboxyl group, i.e. -COOH and -COO⁻. Energy shift of π* peak of carboxyl group was reported for pH dependence of aqueous glycine [9] and acetic acid [1]. Hence, peak energy shift can be explained by deprotonation of carboxyl group in benzoic acid.

We have successfully measured O1s FY spectra of solid benzoic acid and sodium benzoate under atmospheric helium environment. Since measurements were successful, we are planning further investigation with higher resolution on this system and investigation on other system such as wet samples.
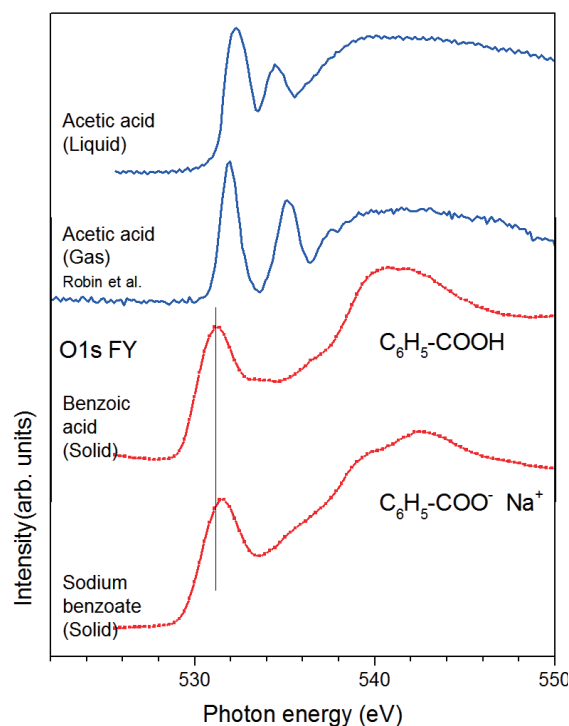
REFERENCES

1.   Y. Horikawa, T. Tokushima, Y. Harada *et al.*, Phys. Chem. Chem. Phys. **11**, 8676 (2009).
2.   T. Tokushima, Y. Harada, O. Takahashi *et al.*, Chem. Phys. Lett. **460**, 387 (2008).
3.   徳島高, 原田慈久, 辛埴, 日本物理学会誌 **63**, 852 (2008).
4.   H. Zhang, W.C. Wang, P.A. Glans *et al.*, J. Elec. Spectrosc. Relat. Phenom. **197**, 118 (2014).
5.   R. Oike, Y. Okamoto, T. Tokushima *et al.*, Electrochemistry **84**, 793 (2016).
6.   H. Yoshida, Y. Senba, T. Goya *et al.*, J. Elec. Spectrosc. Relat. Phenom. **144–147**, 1105 (2005).
7.   M. B. Robin, I. Ishii, R. Mclaren *et al.*, J. Elec. Spectrosc. Relat. Phenom. **47**, 53 (1988).
8.   T. Tokushima, Y. Horikawa, Y. Harada *et al.*, Phys. Chem. Chem. Phys. **11**, 1679 (2009).
9.   B. M. Messer, C. D. Cappa, J. D. Smith *et al.*, J. Phys. Chem. B **109**, 5375 (2005).

Electronic structure of Mg LPSO alloys

Shinya Hosokawa,[a] Jens Rüdiger Stellhorn,[a] Kenji Maruyama,[b]
Kentaro Kobayashi,[b] and Hitoshi Sato[c]

[a]*Department of Physics, Kumamoto University, Kumamoto 860-8555*
[b]*Graduate School of Science and Technology, Niigata University, Niigata 950-2181*
[c]*Hiroshima Synchrotron Radiation Center, Hiroshima University, Higashi-Hiroshima 739-0046*

Recently, a new series of Mg alloys [1] with the microstructures containing a synchronized long-period stacking ordered (LPSO) structure, the so-called KUMADAI Magnesium, has been attracted considerable attention owing to the excellent mechanical properties. By adding a small amount of Zn and rare-earth (Y or Gd) impurities, the soft, flammable, and light-weighted Mg metal becomes much strong and non-flammable. By taking such excellent properties, the new Mg alloys can be used for body materials of subways and even aircrafts.

For the microstructure, a scanning transmission electron microscope image was obtained by Abe et al. [2], which revealed that impurity atoms are enriched at the changes in the stacking order, i.e., the concentrations of the impurities are synchronized with the modulation of the lattice stacking order. Excellent mechanical properties of the LPSO phases were understood owing to such interesting microstructures, i.e., kink bands in the LPSO structures produce the hardness and durability of the Mg alloys.

In this study, we investigate electronic structures of the polycrystalline $Mg_{85}Zn_6Y_9$ and $Mg_{97}Zn_1Y_2$ LPSO alloys together with the reference pure polycrystalline Mg using photoemission and inverse-photoemission spectroscopy (PES and IPES). Core-level PES measurements were also carried out to study the chemical nature of the constituent Mg, Zn, and Y elements.

The Mg LPSO samples were manufactured at Magnesium Research Center, Kumamoto University using a usual slow cooling method in a cylindrical carbon crucible. The composition of the sample was confirmed to be nominal value by an electron-probe micro-analysis equipment. The PES measurements were carried out using high-resolution PES spectrometer installed at BL-7 of HiSOR. The measurements were performed in the incident photon energy range of 30-400 eV to obtain valence-band DOS. We also measured core-level PES spectra for the Mg $2s$ (88.7 eV) and $2p$ (49.50-49.78 eV), Zn $3p$ (88.6-91.4 eV), and Y $3d$ (155.8-157.7 eV) levels to examine the chemical states around each constituent element. The IPES spectra were also obtained using the RIPES spectrometer at HiSOR to measure the conduction-band DOS.

Figure 1 shows PES and IPES spectra of polycrystalline $Mg_{85}Zn_6Y_9$ and $Mg_{97}Zn_1Y_2$ alloys together with the reference pure polycrystalline Mg from tom to bottom. The PES spectra were measured at the incident photon energy, $h\nu$, of 100 eV. The magnitudes of the PES spectra are normalized to the maximum values at about -6 eV of each spectrum, and the IPES spectra are scaled so as to match the DOS at the Fermi energy, E_F, for pure Mg. The curves are shifted each other by 1 for the clarity. In the PES spectra of Mg LPSO alloys, the Zn $3d$ core level peaks are seen at about -10 eV.

The main peaks in the PES spectra are located at about -6 eV, which seem to be unchanged by adding the Zn/Y impurities. The most remarkable change in the PES spectra is observed in the magnitudes of the DOS near E_F, which is much reduced for the heavily doped $Mg_{85}Zn_6Y_9$ alloy. On the other hand, the features of the IPES spectra are very different between the $Mg_{85}Zn_6Y_9$ alloy and the reference pure Mg. For the understandings of these spectral features, a theoretical calculation using, e.g., density functional theory, is necessary.

Figure 2 shows Y $3d$ core-level PES spectra of polycrystalline $Mg_{85}Zn_6Y_9$ and $Mg_{97}Zn_1Y_2$ alloys measure at $h\nu = 230$ eV. For the $Mg_{85}Zn_6Y_9$ alloy having 100% of the LPSO phase, the Y $3d$ core spectra are mainly composed of the $3d_{5/2}/3d_{3/2}$ pair at -158.6/-160.8 eV, and a small contribution is seen at the shallower energies. For the $Mg_{97}Zn_1Y_2$ alloy having only 20% of the LPSO phase, on the other hand, large second pair is observed at about -156.2/-158.4 eV, and at least two chemical states coexist in the lightly doped Mg LPSO alloy. A possible explanation is that the deeper pair corresponds to the Y atoms in the Zn_6Y_8 $L1_2$ clusters embedded in the stacking fault [3], and the shallower one is related to the Y atoms independently located in the Mg host. Detailed analysis is now in progress.
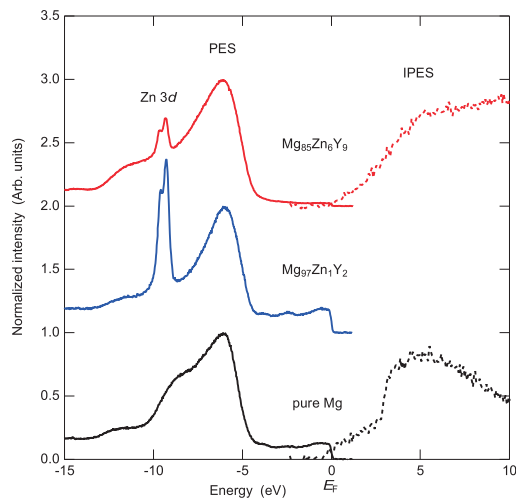
FIGURE 1. PES and IPES spectra of polycrystalline $Mg_{85}Zn_6Y_9$ and $Mg_{97}Zn_1Y_2$ alloys together with the reference pure polycrystalline Mg.
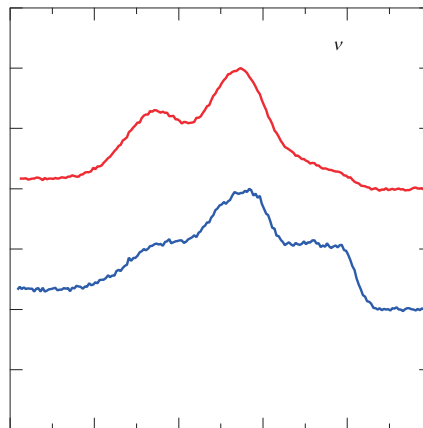

FIGURE 2. Y $3d$ core-level PES spectra of polycrystalline $Mg_{85}Zn_6Y_9$ and $Mg_{97}Zn_1Y_2$ alloys.

REFERENCES

1. Y. Kawamura et al., *Mater. Trans*. **42**, 1172 (2001).
2. E. Abe et al., *Philos. Mag. Lett*. **91**, 690 (2011).
3. D. Egusa and E. Abe, *Acta Mater*. **60**, 166 (2012).

Photoemission and X-ray Absorption Spectroscopic Studies of Sr2-1-4 compounds

S. Tsuda[a], H. Yamaoka[b], H. Sakurai[c], M. Sawada[d], H. Sato[d], R. Awabaikeli[d], M. Arita[d], and K. Shimada[d]

[a]National Institute for Materials Science 3-13 Sakura, Tsukuba 305-0003, Japan
[b]RIKEN SPring-8 Center, Sayo, Hyogo 679-5148, Japan
[c]National Institute for Materials Science 1-1 Namiki, Tsukuba 305-0044, Japan
[d]Hiroshima Synchrotron Radiation Center, Hiroshima University, Higashi-Hiroshima, Hiroshima 739-0046, Japan

Keywords: Photoemission spectroscopy, X-ray absorption spectroscopy, transition metal oxides

α-Sr_2VO_4 is a compound with K_2NiF_4 structure. Because of the electronic configuration (V $3d^1$), α-Sr_2VO_4 has attracted many researchers as a counterpart of $3d^9$ system such as La_2CuO_4. Very recently, the sample quality has improved significantly and three transitions (T_N = 10 K, T_1 = 101 K, T_2 = 127 K) are identified [1].

α-Sr_2CrO_4 is also a compound with K_2NiF_4 structure. The electronic configuration is V $3d^2$. The high quality sample shows two-phase transitions (T_N = 112 K, T_s = 140 K) [2]. Conventional crystal field theory suggests that the energy levels of $d_{yz,zx}$ orbitals have lower energy than that of the d_{xy} orbital. However, an *ab-initio* calculation predicted the inversion of those energy levels [3]. This anomalous situation appears only in Sr_2CrO_4; within the same frame work, the d_{xy} orbtail of Sr_2VO_4 has higher energy than $d_{yz,zx}$ orbitals. These expectations have not been evaluated from experimental point of view.

We perfomed x-ray photoemission and x-ray absorption spectroscopy studies of Sr_2VO_4 and Sr_2CrO_4. Figure 1 shows x-ray absorption spectra of (a) Sr_2VO_4 and (b) Sr_2CrO_4. Those compounds show very small temperature dependence across the transitions. The spectra of the Sr_2VO_4 are very similar to the spectra of V^{4+} compounds and the spectra of the Sr_2CrO_4 are very similar to the spectra of Cr^{4+} compounds. These values of the valences are consistent with the formal valency by supposing Sr^{2+} and O^{2-}.
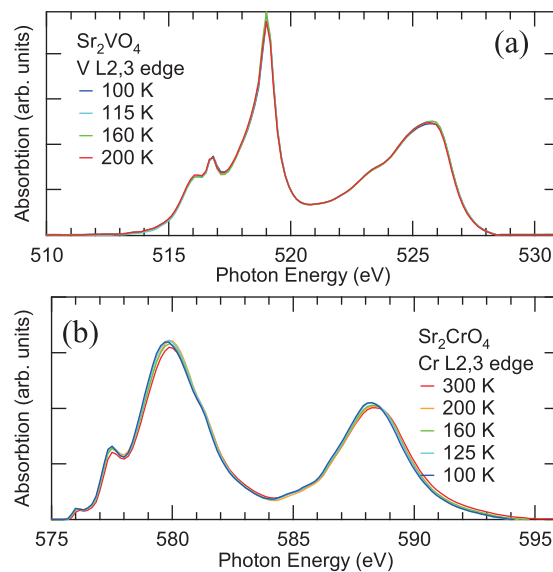

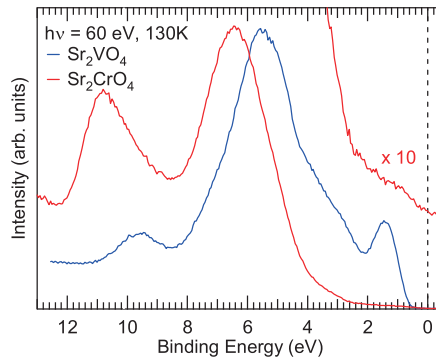**FIGURE 1.** X-ray absorption spectra of (a) Sr_2VO_4 and (b) Sr_2CrO_4 at $L_{2,3}$ edge.

FIGURE 2. Valence band photoemission spectra of Sr₂VO₄ and Sr₂CrO₄.

Figure 2 shows valence band photoemission spectra of Sr₂VO₄ and Sr₂CrO₄. Sr₂VO₄ (blue in fig. 2) has four features at 9.8 eV, 5.5eV, 3.5 eV and 1.7 eV. The feature around 5.5 eV and 3.5 eV can be ascribed to O $2p$ states and the feature around 1.7 eV can be ascribed to V $3d$ states. The origin of the feature around 9.8 eV is unknown. Sr₂CrO₄ (red in fig. 2) has three features at 10.8 eV, 6.4 eV and 1.0 eV. The feature around 6.4 eV can be ascribed to O 2p states and the origin of the feature around 10.8 eV is unknown. The feature around 1.0 eV will be attributed to Cr $3d$ states. However, compared to conventional Cr^{3+} compounds, the spectral intensity of the Cr 3d state is too small. The spectral shape is rather similar to Cr^{6+} ($3d^0$). This is inconsistent with x-ray absorption results, which indicates Cr^{3+}. One possible origin of this discrepancy is surface state. Further investigation is required.

REFERENCES

1. H. Sakurai, *Physics Procedia* **75**, 829 (2015).
2. H. Sakurai, *J. Phys. Soc. Jpn.* **83**, 123701 (2014).
3. T. Ishikawa *et al.*, *J. Phys. Soc. Jpn.* **86**, 033701 (2017).

ARPES measurements on mixed crystal films of topological crystalline insulator SnTe

Ryota Akiyama[a] Yusuke Otaki[b], Ryosuke Nakanishi[a], Di Fan[a], Ryo Ishikawa[b], Tomonari Yamaguchi[b], Hitoshi Sato[c], Akio Kimura[d], Eike F. Schwier[c], Koji Miyamoto[c], Kenya Shimada[c], Shuji Hasegawa[a], and Shinji Kuroda[b]

[a]*Department of Physics, The University of Tokyo, Tokyo, Japan*
[b]*Institute of Materials Science, University of Tsukuba, Tsukuba, Japan*
[c]*Hiroshima Synchrotron Radiation Center, Hiroshima University, Hiroshima, Japan*
[d]*Department of Physics, Hiroshima University, Hiroshima, Japan*

Keywords: Topological insulator, Topological crystalline insulator, Spin-orbit interaction, 2D material, Thin film

Topological insulators (TIs) are the new class of materials and attract much attention these days because of their abundant interesting and novel properties such as spin-momentum locking, spin-split band, Dirac Fermion, and Majorana Fermion. In 3-dimensional TIs, the surface is metallic whereas the bulk is insulating. Such surface state is called the topological surface state (TSS), and the spin of carriers split except for the Kramers degeneracy points ($k = 0$). The TSS is protected by the time-reversal symmetry and induced by the band inversion due to the strong spin-orbit interaction.

Topological crystalline insulators (TCIs) are the family of TIs, but the TSS of TCIs is protected by the crystal mirror symmetry instead of the time-reversal symmetry. As the TCI material, SnTe[1], SnSe[2], $Pb_xSn_{1-x}Te$[1], $Pb_xSn_{1-x}Se$[3] have been proposed and confirmed. The band characteristics of the TSS in SnTe were demonstrated experimentally by the angle-resolved photoemission spectroscopy (ARPES) with bulk crystals of (001) and (111) orientation in 2012 and 2013, respectively[1,4]. On the other hand, the electrical transport was measured in the thin films so far[5-8]. However, it has been difficult to obtain the TSS of SnTe directly because SnTe tends to be heavily doped p-type. Especially, the TSS of the thin film $Pb_xSn_{1-x}Te$ (111) is unclear so far because there is no systematic investigation with changing the incident photon energy (PE).

We have confirmed the 2-dimentional band characteristic around Γ point in As doped $Pb_xSn_{1-x}Te$ so far. However, the detail structure around the Dirac cone was not clarified because the Fermi level still overlaps with the bulk valence band in the $Pb_xSn_{1-x}Te$:As. Thus we selected more effective compensation atom, Sb.

In this research, we aim to observe the surface band, particularly Dirac point, directly by tuning the Fermi level. In TCIs, there is almost no work to check the change of the Dirac cone by doping magnetic atoms. This is mainly because we can not see the surface band around the Dirac point clearly due to heavily p-type nature. Thus, the mechanism of the gap opening in TCI is still unknown experimentally. The band inversion of the valence and conduction band at L point occurs in SnTe, and it is required to realize the TSS. According to the previous reports,
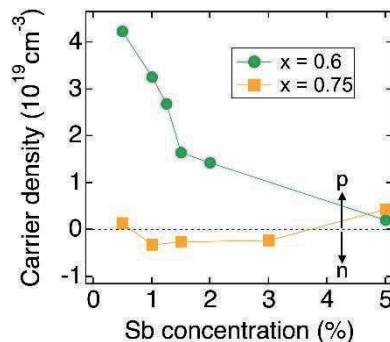

FIGURE 1. The Sb concentration dependence of the carrier density in $Pb_{0.6}Sn_{0.4}Te$ and $Pb_{0.75}SnTe$. $Pb_{0.75}Sn_{0.25}Te$ becomes both p and n-type corresponding to the Sb concentration.

the band inversion of $Pb_xSn_{1-x}Te$ occurs and the TSS persists with doping Pb up to $x \sim 0.75$. We confirmed that the carrier compensation can be realized with doping Sb by electrical transport measurements as shown in Fig.1. The carrier density is changed with changing Sb concentration. Especially, $Pb_{0.6}Sn_{0.4}Te$ can be tuned to both p and n-type conduction. As p-type sample, Sb 5% doped $Pb_{0.6}Sn_{0.4}$ is the most bulk insulating within the range shown in Fig.1. Since we aim to observe the surface band, the sample of $Pb_{0.6}Sn_{0.4}Te$:Sb 5% was adopted for ARPES measurements.

To check the dimension of the band, we changed the incident PE from 65 – 120 eV at 15 K. At 65 eV, the inversed V-shaped bulk valence band was seen whereas such band disappear at the incident PE = 105 eV as shown in Figs. 2 (a) and (b). The bulk valence band changes its shape to the V-shaped band at the PE = 105 eV (blue dashed curve) as shown in Fig. 2(b). Instead, the band which does not change with the incident PE becomes visible at 105 eV (white dashed line and circle). This band is hindered by the bulk valence band at the PE = 65 eV whereas it locates at k_x, $k_y = 0$ and around E_F. The energy-contour maps sliced at the energy of i, ii, and iii as indicated in Fig 2(b) are shown in Fig. 2(c). The white circles correspond to the white lines in Fig. 2(b) and these are unchanged band with the PE. According to the theoretical calculation there is no bulk band around E_F at k_x, $k_y = 0$. These facts suggest that this band has the 2-dimensional nature and it is the surface band. We performed this experiment using the homemade potable chamber which can transport samples with keeping the ultrahigh vacuum environment and transfer to the ARPES measurement chamber without exposing samples to the air.

In this study, we investigated electronic properties about $Pb_xSn_{1-x}Te$ systematically with electrical transport

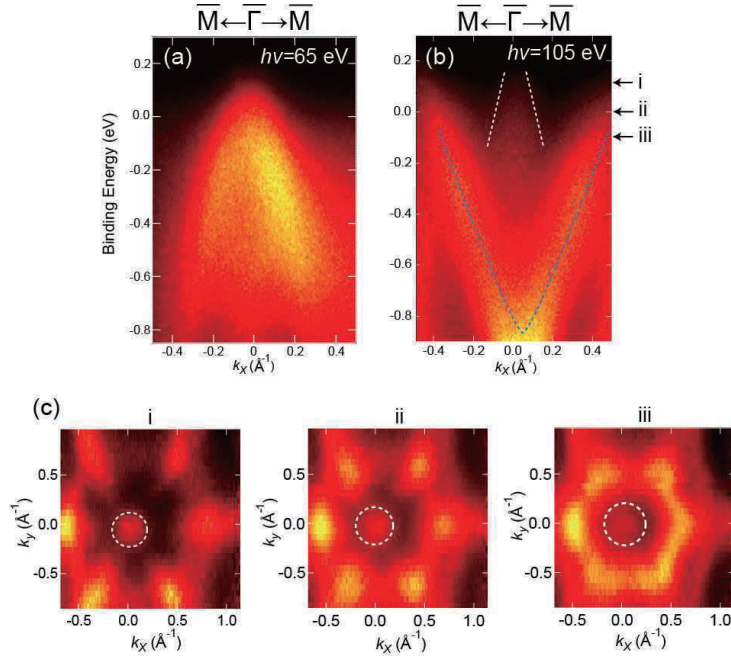**FIGURE 2.** The band dispersion along the direction of $\overline{\Gamma} - \overline{M}$ at the incident photon energy of (a) 65 eV and (b) 105 eV at 15 K, respectively. The white (blue) dashed line (curve) represents the surface band (bulk valence band). (c) The Energy-contour maps sliced at the energy of i, ii, and iii indicated in (b). The white circles correspond to the surface band.

measurements and ARPES measurements. Particularly, the 2-dimensional surface band in $Pb_xSn_{1-x}Te(111)$ was confirmed for the first time. The detail observation around the Dirac point is required for clarifying whether the gap exists or not in $Pb_xSn_{1-x}Te$ with $x > 0.75$ or the TCI/ferromagnetic material junction. The former will reveal the condition of gap-opening in the thin film case of $Pb_xSn_{1-x}Te$, and the latter will pave the way to understand the recent open discussion matter, namely, the relation between the TSS and the (ferro)magnetic interaction.

REFERENCES

1. Y. Tanaka, Zhi Ren, T. Sato, K. Nakayama, S. Souma *et al.*, Nat. Phys. **8**, 800 (2012).
2. Z. Wang, J. Wang, Y. Zang, Q. Zhang, J.-A. Shi *et al.*, Adv. Mater. **27**, 4150 (2015).
3. P. Dziawa, B. J. Kowalski, K. Dybko, R. Buczko, A. Szczerbakow *et al.*, Nat. Mat. **11**, 1023 (2012).
4. Y. Tanaka, T. Shoman, K. Nakayama, S. Souma, T. Sato *et al.*, Phys. Rev. B **88**, 235126 (2013).
5. A. A. Taskin, F. Yang, S. Sasaki, K. Segawa, and Y. Ando, Phys. Rev. B **89**, 121302 (2014).
6. B. A. Assaf, F. Katmis, P. Wei, B. Satpati, Z. Zhang *et al.*, Appl. Phys. Lett. **105**, 102108 (2014).
7. M. Safdar, Q. S. Wang, M. Mirza, Z. X. Wang, K. Xu, J. He, Nano Lett. **13**, 5344 (2013).
8. R. Akiyama, K. Fujisawa, T. Yamaguchi, R. Ishikawa, and S. Kuroda, Nano Research **9**, 490 (2016).

Valence-band structure of organic radical p-CF$_3$PNN investigated by angle-resolved photoemission spectroscopy

H. Anzai[a], R. Takakura[a], Y. Ono[a], S. Ishihara[a], H. Sato[b], H. Namatame[b], M. Taniguchi[b], T. Matsui[a], S. Noguchi[c], and Y. Hosokoshi[c]

[a] *Graduate School of Engineering, Osaka Prefecture University, Sakai 599-8531, Japan*
[b] *Hiroshima Synchrotron Radiation Center (HSRC), Hiroshima University, Higashi-Hiroshima 739-0046, Japan*
[c] *Graduate School of Science, Osaka Prefecture University, Sakai 599-8531, Japan*

Stable organic-based magnetic compounds have been the focus of intense multidisciplinary efforts in view of their possible use in applications for material science and electronics. The p-trifluoromethylphenyl nitronyl nitroxide (p-CF$_3$PNN), which exhibits antiferromagnetic interactions at low temperature, is a well-known stable organic radical [1]. In this system, the molecular arrangement of the radicals that bear an unpaired electron in the singly occupied molecular orbital (SOMO) is responsible for the exchange interaction between electron spins. Their arrangement has therefore been studied extensively over the past decades for many nitronyl nitroxide radicals [2]. In contrast, the details of the fundamental electronic structure remain unexplored.

Photoemission spectroscopy is a direct probe to measure the electronic structure. A previous photoemission spectroscopy study of the nitronyl nitroxide radicals reported that the electronic structure near the Fermi level (E_F) consists of multiple bands and orbitals [3]. Consequently, the multiband nature is closely related to the antiferromagnetic interaction in p-CF$_3$PNN, and it is important to reveal the electronic structure near E_F and identify the orbital characters of bands. Here, we report the valence band of p-CF$_3$PNN using angle-resolved photoemission spectroscopy (ARPES), which has a unique ability to image the electronic structure in energy-momentum space.

Single crystals of p-CF$_3$PNN with triclinic structure were grown by recrystallization from benzene, hexane, and diethyl [4]. The chemical structure is shown in Fig. 1(a). The ARPES measurements were performed at BL-7 of Hiroshima Synchrotron Radiation Center. All the data were collected at $T = 300$ K with $h\nu = 50$ eV. Total energy resolution was set to 62 meV. The samples were kept under a high vacuum of 4.7×10^{-9} Torr during the measurements. We have taken all precautions necessary, for instance short beam exposure and short acquisition time, to avoid the radiation damage. No beam-induced degradation of the samples was observed in our experiments.

Figure 1(c) shows the ARPES spectra taken along a green line of the two-dimensional Brillouin zone in Fig. 1(b). The nondispersive bands were observed clearly at $|\omega| \sim 4.5$, 7.6, and 10 eV for the first time. The dispersive valence bands are not visible in the energy range of $2 < |\omega| < 18$ eV. These results imply the localized electronic states of p-CF$_3$PNN.

To simplify the data analysis, we integrated energy distribution curves over the momentum region shown in Fig. 1(c) and exemplified the result in Fig. 1(d). We found that the 4.5 eV peak has a shoulder structure at ~ 2.0 eV, as indicated by an arrow in Fig. 1(d). This first band blow E_F is can be assigned to the SOMO. The energy of the SOMO with respect to the vacuum level is ~ 6.5 eV, which is consistent with the first vertical ionization potential reported in the previous study of phenyl α-nitronyl nitroxide [3].

The energy of singly unoccupied molecular orbital (SUMO) is not accessed experimentally but can be roughly estimated by two times of the SOMO-E_F energy, because E_F is located at the center of SOMO-SUMO band gap. The onset of the leading edge of the SOMO is at $|\omega| \sim 1$ eV below E_F, and thus the band gap is approximately ~ 2 eV.
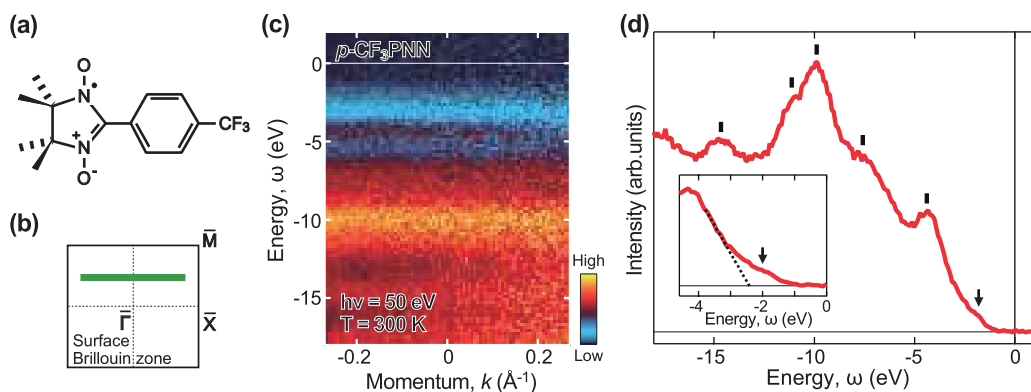
Figure 1. (a) Chemical structure of *p*-CF₃PNN. (b) The two-dimensional Brillouin zone of the triclinic crystal. (c) ARPES spectra taken along a momentum cut slightly off the $\overline{\Gamma}$-$\overline{X}$ direction, as marked green line in (b). (d) Valence-band spectra, where energy distribution curves are integrated over the momentum region in (c). The vertical bars and arrows indicate the peak positions. Inset shows the enlarged view of the valence-band spectra near E_F. Dashed line represents a linear background.

The orbital characters of bands are deduced from the theoretical calculations of molecular orbitals in this system [3,5]. The SOMO is assigned to the antibonding combination between the π* orbitals of the NO groups, making a node at the α-carbon atom. The 4.5 eV peak is composed of the two NO π* orbitals, the α-carbon p_z orbital, and the phenyl π orbital. In the results of the photon energy dependence of pyrrolidine nitroxyl radicals, the intensities over an energy range of $6 < |\omega| < 12$ eV increase with decreasing the photon energies [6]. The spectral photoionization cross-section of N $2p$ orbital increases more rapidly than that of C $2p$ with decreasing photon energy [7]. Thus, we assigned the broad bands around 10 eV to the N $2p$ orbitals. Further experiments in wide momentum ranges are required to provide the detailed evolution of the electronic state in *p*-CF₃PNN.

In conclusion, we investigated the valence band structure in *p*-CF₃PNN using ARPES. We find for the first time that the SOMO is located at $|\omega| \sim 2.0$ eV and originates from the antibonding conbination between the π* orbitals of the NO groups. These findings suggest that the NO π* orbital is likely to play an important role in the antiferromagnetic interaction between neighboring spins.

REFERENCES

1. K. Nozawa *et al.*, Synthetic Metals **55**, 3323 (1993).
2. Y. Hosokoshi *et al.*, Physica B **201**, 479 (1994).
3. K. Awaga *et al.*, Mol. Cryst. Liq. Cryst. **232**, 27 (1993).
4. E. F. Ullman *et al.*, J. Org. Chem. **35** 3623 (1970).
5. I. Morishima *et al.*, Chem. Phys. Lett. **16**, 336 (1972).
6. B. Kovac *et al.*, Phys. Chem. Chem. Phys., **16**, 10734 (2014).
7. J. J. Yeh Gordon and Breach, Langhorne, PA, (1993).

Electronic structure of amorphous $Mg_{85}Zn_6Y_9$ alloy

Shinya Hosokawa,[a] Jens Rüdiger Stellhorn,[a] Kenji Maruyama,[b]
Kentaro Kobayashi,[b] and Hitoshi Sato[c]

[a]*Department of Physics, Kumamoto University, Kumamoto 860-8555*
[b]*Graduate School of Science and Technology, Niigata University, Niigata 950-2181*
[c]*Hiroshima Synchrotron Radiation Center, Hiroshima University, Higashi-Hiroshima 739-0046*

Keywords: Amorphous metal, LPSO structure, Impurities, Electronic structure, Chemical states

Recently, a new series of Mg alloys [1] with the microstructures containing a synchronized long-period stacking ordered (LPSO) structure, the so-called KUMADAI Magnesium, has been attracted considerable attention owing to the excellent mechanical properties. By adding a small amount of Zn and rare-earth (Y or Gd) impurities, the soft, flammable, and light-weighted Mg metal becomes much strong and non-flammable. By taking such excellent properties, the new Mg alloys can be used for body materials of subways and even aircrafts.

For the microstructure, a scanning transmission electron microscope image was obtained by Abe et al. [2], which revealed that impurity atoms are enriched at the changes in the stacking order, i.e., the concentrations of the impurities are synchronized with the modulation of the lattice stacking order. Excellent mechanical properties of the LPSO phases were understood owing to such interesting microstructures, i.e., kink bands in the LPSO structures produce the hardness and durability of the Mg alloys.

Recently, Okuda et al. [3] investigated the transformation process of amorphous-to-crystal in $Mg_{85}Zn_6Y_9$ LPSO alloy using small angle x-ray scattering. They found a novel hierarchical phase transformation that the clustering of the impurity atoms occurs first, and the spatial rearrangement of the clusters induces a secondary transformation leading to two-dimensional ordering of the clusters. From their results, we expect that the seeds of the impurity clusters are already implanted even in the amorphous phase.

Core-level photoemission spectroscopy (PES) is a powerful tool to investigate the chemical nature of the constituent elements. In this study, we measured Mg $2s$ and $2p$ Zn $3p$, and Y $3d$ core-level PES spectra of amorphous and polycrystalline $Mg_{85}Zn_6Y_9$ alloys together with the reference pure polycrystalline Mg. An $Mg_{85}Zn_6Y_9$ sample was manufactured at Magnesium Research Center, Kumamoto University by a normal melt-spinning technique. The amorphous phase of the obtained ribbons was examined by x-ray diffraction and transmission electron microscopy. The composition of the sample was confirmed to be nominal value by an electron-probe micro-analysis equipment.

The PES measurements were carried out using high-resolution PES spectrometer installed at BL-7 of HiSOR. The measurements were performed in the incident photon energy range of 30-400 eV to obtain valence-band density of states (DOS). We also measured core-level PES spectra for the Mg $2s$ (88.7 eV) and $2p$ (49.50-49.78 eV), Zn $3p$ (88.6-91.4 eV), and Y $3d$ (155.8-157.7 eV) levels to examine the chemical states around each constituent element. The IPES spectra were also obtained using the RIPES spectrometer at HiSOR to measure the conduction-band DOS.

Figure 1 shows the results of (a) Mg $2s$ and Zn $3p$, (b) Mg $2p$, and (c) Y $3d$ core-level PES spectra of amorphous and polycrystalline $Mg_{85}Zn_6Y_9$ alloys, and pure polycrystalline Mg from top to bottom. The magnitudes of the spectra are normalized to the maximum value of each spectra, and the curves are shifted each other by 1 for the clarity. The peak energies are given in Table 1. As regards the Mg core levels, the features of the spectra shown in Fig. 1(a) and (b) are very similar to each other, indicating that no heterogeneous trends are realized even though a large fraction of the host atoms are located adjacent to the Zn or Y impurities. Small shifts are, however, observed towards the shallower energies in the peak positions as shown in Table 1. These shifts intuitively indicate a small electron charge transfer to Mg^{2+} to form $Mg^{(2-\delta)+}$ ions.

For the difference between the amorphous and crystalline phases, on the other hand, no changes are observed in the energy positions of all of the core levels beyond the experimental errors. This result highly suggest that the local atomic configurations are not so different from each other, and the crystal-like seeds of the impurity clusters may be implanted in the amorphous phase.
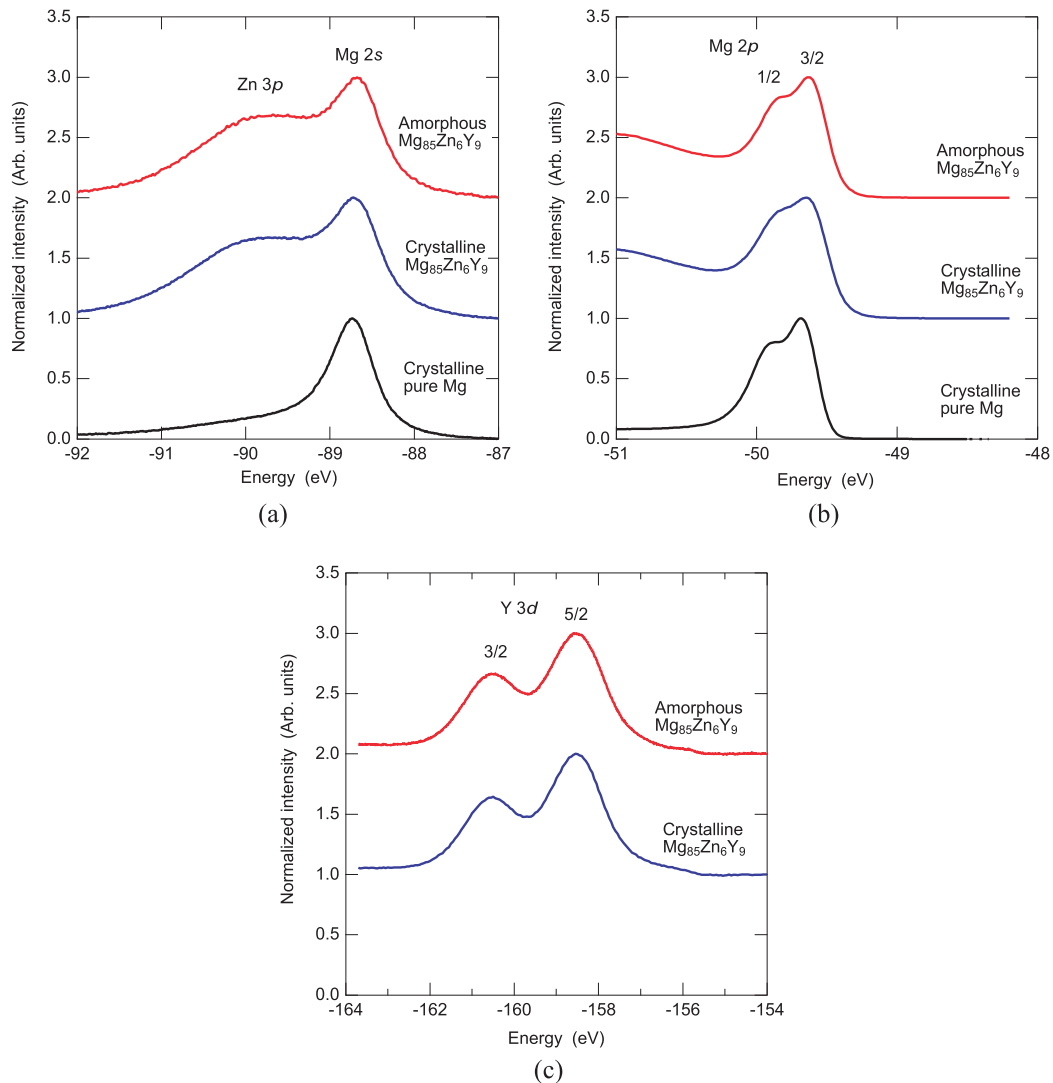
FIGURE 1. (a) Mg $2s$ and Zn $3p$, (b) Mg $2p$, and (c) Y $3d$ core-level PES spectra of amorphous and polycrystalline $Mg_{85}Zn_6Y_9$ alloys together with the reference pure polycrystalline Mg.

TABLES 1). The peak energies of Mg $2s$ and $2p_{3/2}$, Zn $3p$, and Y $3d_{5/2}$ core-level PES spectra of amorphous and polycrystalline $Mg_{85}Zn_6Y_9$ alloys together with the reference pure polycrystalline Mg.

Core level	Amorphous $Mg_{85}Zn_6Y_9$	Crystalline $Mg_{85}Zn_6Y_9$	Pure crystalline Mg
Mg $2s$	−88.66	−88.72	−88.73
Mg $2p_{3/2}$	−49.64	−49.65	−49.69
Zn $3p$	−89.8	−89.9	−
Y $3d_{5/2}$	−158.55	−158.55	−

REFERENCES

1. Y. Kawamura et al., *Mater. Trans.* **42**, 1172 (2001).
2. E. Abe et al., *Philos. Mag. Lett.* **91**, 690 (2011).
3. H. Okuda et al., *Sci. Rep.* **5**, 14186 (2015).

Interface Electronic State between ZnO Thin-Film with Oxygen Defects and Cu Electrode

Sumera Shimizu, Hideo Asai, Shinichi Ito, and Toshihiko Miyakawa

DENSO Corp. Materials Eng. R & D Div., 1-1, Showa-cho, Kariya, Aichi 448-8661, Japan

Recently, environmental restrictions and requests accelerate electrification of in-vehicle equipment. One of the key-factors for the electrification is to control simultaneously multiple interface properties. For example, an electric motor should have both "low friction" and "low electric resistance" at the electrode interface.

Previously, we have been observed that zinc oxide (ZnO) generates on a copper electrode, based on Zn-K edge X-ray absorption fine structure (XAFS) [1]. This comes from that some parts in the motor include zinc compounds. Since the ZnO is harder than original electrode-materials [2], it might affect friction coefficient between the electrodes. Additionally, the ZnO is possibly an n-type semiconductor material because our XAFS measurement showed that it includes oxygen defects [1]. This indicates formation of a Schotkky contact on the ZnO/Cu electrode interface, leading to increase the electric resistance of the motor.

In this study, we carried out ultraviolet photoelectron and inverse photoelectron spectroscopies (UPS/IPES) for ZnO thin-films deposited on a Cu substrate by pulse laser deposition (PLD). The results provided the hole and electron-injection barriers" at the ZnO/Cu interface, to discuss and optimize the interface electronic properties of the motor.

ZnO thin-films were prepared on tough-pitch copper substrate (99.9 %) by using PLD method. The films were deposited under UHV at room temperature from a calcined ZnO target (99.99 %). This deposition-condition was selected to introduce oxygen defects to the film. The thicknesses were set to 5 nm and 20 nm. The UPS measurement was carried out on BL-7 at HiSOR, and the IPES measurement was done by using another on-site apparatus at room temperature. The incident photon energy and pass energy for UPS were selected to 200 eV and 10 eV. The primary electron energy for IPES was done to 50 eV. The binding energy was calibrated to the Fermi level (E_F) of Au reference.

Fig. 1 shows the combined UPS and IPES spectra of the ZnO films on the Cu substrate. The lower and upper spectra correspond to the thicknesses of 5 nm and 20 nm, respectively. In the UPS spectrum of 20 nm ZnO, the peaks at 4 eV and 10 eV are assigned to O 2p and Zn 3d, respectively [3]. The coexistence of their peaks shows the co-deposition of zinc and oxygen. Since the intensity of Zn 3d is much higher than that of O 2p, the film should include some oxygen defects as our intension The onset of the O 2p band, the valence band maximum (VBM), is found at 2.36 eV below the E_F. Meanwhile, in the UPS spectrum of 5 nm ZnO, the small Zn 3d peak exists at around 10 eV. The O 2p peak is possibly around 2.3 eV, hiding in the Cu 3d band of the substrate. Also, the spectrum has another structure at ~1 eV, which is not observed for a clean copper surface as shown in Fig. 1 [4]. We speculate that it corresponds to a reduced state of zinc (= 4s electrons of $Zn^{<2+}$). In the IPES spectra of 20 nm and 5 nm ZnO, the onsets, the conduction band minimum (CBM), exist at 0.49 eV and 0.94 eV above the E_F, respectively. The density of state consists of unoccupied Zn 4s and O 2p states [5].

Based on the results in Fig. 1, we discuss the following three properties about the ZnO film: band gap energy, Fermi level position, and degree of band bending. Firstly, the band gaps for the 20 nm and 5 nm films are calculated as 2.85 eV and ~3.2 eV, respectively, from summation of the VBM and CBM. These values are slightly smaller than and the same as the previous report [3]. This assures that ZnO deposits on the Cu substrate. Secondly, the Fermi levels of the ZnO films are close to the CBM, showing that they have n-type semiconductivity. This n-type characteristic should originate from the oxygen defects ($Zn^{<2+}$) acting as electron donor. Finally, the degree of band bending from 5 nm to 20 nm is estimated as 0.35-0.47 eV because the Zn 3d peak and the IPES-onset shift down to the values as decreasing thickness. This indicates that a Schottky barrier is formed at the ZnO/Cu interface.

To investigate more specifically the band bending in the ZnO film, photoelectron yield spectroscopy (PYS) and IPES (Bremsstrahlung Isochromat Spectroscopy (BIS) mode, E_k = 5-20 eV) were measured for the 5 nm ZnO film at Japan Advanced Institute of Science and Technology (JAIST). These measurements become more surface sensitive than our acquired UPS and IPES spectra at HiSOR: We cannot see the Cu substrate and the ZnO/Cu interface, but can clearly do the film itself. As a result, the VBM and CBM were observed at 2.32 eV and 0.51 eV below/above the E_F, respectively, and here the in-gap state from the reduced Zn was obviously done at 0.77 eV as indicated in the UPS spectrum in Fig. 1 (The PYS and BIS-IPES spectra are not shown).

Fig. 2 shows the energy diagram proposed by the above results. Here, the electron-injection barrier is obviously lower than the hole-injection barrier, even though there exist upward band bending due to the Schottky junction. This imbalanced carrier injection at the interface could lead to unstable rotation of the motor. Additionally, the reduced Zn state (possibly $Zn^{<2+}$) could act as trapping states for the injected electron and hole: it prevents the electric current from flowing smoothly in the motor-circuit. To keep the balance between the both injection barriers, neutral ZnO without any oxygen vacancies must be formed under the motor-operation. In future, we will consider new additives and electrode-structures to achieve such chemical condition.
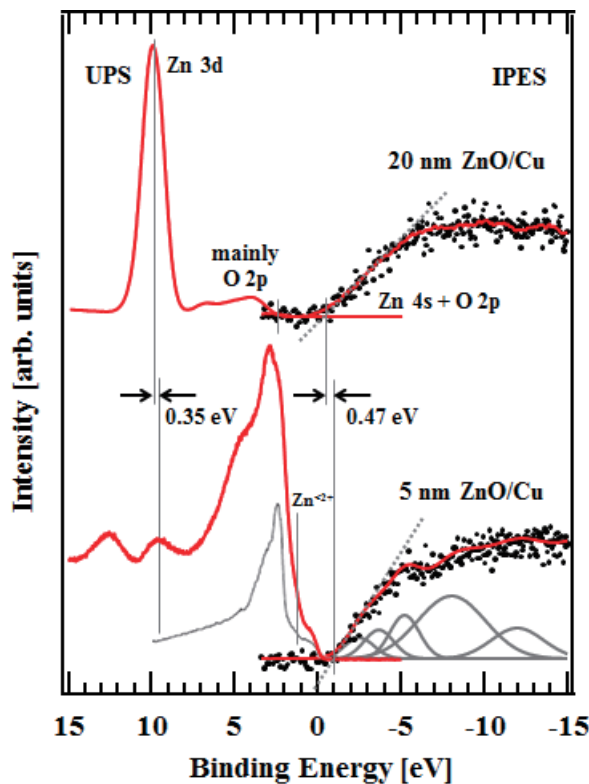
Fig. 1. The combined UPS and IPES spectra of the n-type ZnO films on the Cu substrate.
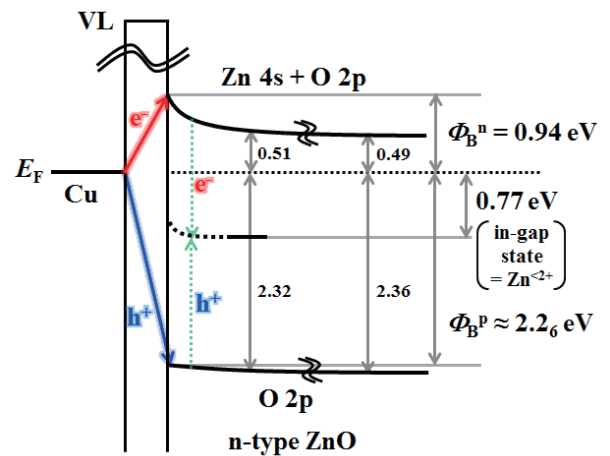
Fig. 2. The energy diagram at the interface between the n-type ZnO and the Cu substrate.

REFERENCES

1. S. Shimizu *et al.*, in-house report (2016).
2. Radix Corporation, http://radixs.biz/ktouroku/private/Radix305.xls
   Kochi University of Technology, http://www.kochi-tech.ac.jp/zno/story/story_01.html
3. S. H. Su *et al.*, *J. Phys. Chem. C* **116**, 9917-9924 (2012).
4. A. Siokou *et al.*, *Appl. Surf. Sci.* **257**, 9785-9790 (2011).
5. R. Viswanatha *et al.*, J. Mater. Chem. **14**, 661-668 (2004).

c-f hybridization strength in various Eu compounds revealed by Eu 4*d*-4*f* resonant photoemission spectroscopy

K. Mimura[a,c], K. Ichiki[a], K. Abe[a], T. Matsumoto[a], Y. Akedo[b], K. Kawakami[b],
T. Uozumi[a], H. Sato[c], A. Rousuli[d], Y. Taguchi[a], H. Namatame[c], M. Taniguchi[c],
Y. Ashitomi[e], H. Akamine[e], A. Nakamura[f], M. Hedo[g], T. Nakama[g], Y. Ōnuki[g],
T. Fujimoto[h], E. Kishaba[h], S. Hamano[h], A. Mitsuda[h], and H. Wada[h]

[a]*Graduate School of Engineering, Osaka Prefecture University, Sakai 599-8531, Japan*
[b]*Faculty of Engineering, Osaka Prefecture University, Sakai 599-8531, Japan*
[c]*Hiroshima Synchrotron Radiation Center (HSRC), Hiroshima University, Higashi-Hiroshima 739-0046, Japan*
[d]*Graduate School of Science, Hiroshima University, Higashi-Hiroshima 739-8526, Japan*
[e]*Graduate School of Engineering and Science, University of the Ryukyus, Okinawa 903-0213, Japan*
[f]*Institute of Materials Research, Tohoku University, Sendai 980-8577, Japan*
[g]*Faculty of Science, University of the Ryukyus, Okinawa 903-0213, Japan*
[h]*Graduate School of Science, Kyushu University, Fukuoka 819-0395, Japan*

Eu ion owes two valence states: divalent Eu state (Eu^{2+}, $4f^7$) having magnetic moment of $J = 7/2$ and nonmagnetic trivalent Eu state (Eu^{3+}, $4f^6$). Some of the Eu compounds exhibit a valence fluctuation between Eu^{2+} and Eu^{3+}. It is well known, furthermore, that its Eu valence significantly changes as a function of temperature, pressure and magnetic field, so called the valence transition. These phenomena originate from the hybridization between Eu 4*f* electrons with conduction electrons (*c-f* hybridization) [1].

Recently, we have observed the bulk-derived Eu 3*d* spectra for $EuPd_2Si_2$ and $EuNi_2(Si_{1-x}Ge_x)_2$ by means of hard x-ray photoemission spectroscopy (HAXPES) and revealed the importance of the *c-f* hybridization in the valence transition [2, 3]. For further understanding of the *c-f* hybridization, the observation of the Eu 4*f* electronic structure is important, but that in the HAXPES experiments is difficult because of the influence of the conduction electronic structure, especially, *s* and *p* electronic states. In this study we have investigated the Eu 4*f* electronic structure by means of Eu 4*d*-4*f* resonant photoemission spectroscopy (RPES) in order to understand the *c-f* hybridization effect for the Eu compounds having various Eu mean valence *v*. The Eu 4*d*-4*f* RPES experiments at 20 K for the Eu compounds, which are listed in Table 1, were performed at BL-7 of HSRC. The overall energy resolution was set to 130 meV. Clean sample surfaces were prepared by *in situ* fracturing.

TABLE 1). Transition temperatures (Néel temperature T_N, Curie Temperature T_C, and valence transition temperature T_v) and Eu mean valence *v* at 20 K, which is evaluated from our Eu 3*d* HAXPES experiments for the samples used in this study. $E_B^{Eu^{2+}}$ and $\Delta E_{Eu^{3+}-Eu^{2+}}$ values obtained in this study are also listed.

Samples	T_N (K)	T_C (K)	T_v (K)	*v* at 20 K from HAXPES	$E_B^{Eu^{2+}}$ (eV)	$\Delta E_{Eu^{3+}-Eu^{2+}}$ (eV)
$Eu_{0.85}Ca_{0.15}Fe_2As_2$ [4]	17	—	—	2	1.62	—
$EuPd_2$ [5]	—	74	—	2	1.20	—
$EuPt_2$ [5]	—	100	—	2	0.93	—
$EuRh_2Si_2$ [6, 7]	23	—	—	2.08	0.71	6.10
$EuNi_2Ge_2$ [8]	—	—	—	2.18	0.69	6.15
$EuNi_2P_2$ [9]	—	—	—	2.63	0.66	6.05
$Eu(Rh_{0.7}Ir_{0.3})_2Si_2$ [7]	24	—	30	2.64	0.64	6.00
$Eu(Rh_{0.5}Ir_{0.5})_2Si_2$ [7]	—	—	88	2.67	0.65	6.00
$Eu(Rh_{0.6}Ir_{0.4})_2Si_2$ [7]	—	—	46	2.73	0.69	6.05
$EuNi_2(Si_{0.18}Ge_{0.82})_2$ [10]	—	—	56	2.75	0.67	5.95
$EuNi_2(Si_{0.30}Ge_{0.70})_2$ [11]	—	—	150	2.80	0.66	5.80
$EuNi_2(Si_{0.21}Ge_{0.79})_2$ [10]	—	—	84	2.83	0.69	5.90
$Eu(Rh_{0.6}Co_{0.4})_2Si_2$ [12]	—	—	—	2.92	0.68	5.80

For example, the Eu $4f$ spectra of Eu(Rh$_{0.7}$Ir$_{0.3}$)$_2$Si$_2$ are shown in Fig. 1(a). The Eu $4f$ spectrum was obtained by the subtraction of the off-resonance spectrum at $h\nu = 136.0$ eV from the Eu^{2+} (Eu^{3+}) on-resonance spectrum at $h\nu = 141.0$ eV (150.5 eV). Multiplet structures ascribed to the bulk-derived Eu^{2+} $4f$ states are clearly found around 0.6 eV in spite of the existence of an intense peak of the surface-derived Eu^{2+} $4f$ states. Multiplet structures to the bulk-derived Eu^{3+} $4f$ state are also observed from 5.5 to 12 eV, reflecting that Eu(Rh$_{0.7}$Ir$_{0.3}$)$_2$Si$_2$ is in the valence fluctuation state at 20 K ($v = 2.64$). Peak position of the Eu^{2+} $4f$ multiplet structures ($J = 6$) $E_{\mathrm{B}}^{\mathrm{Eu}^{2+}}$ and energy difference between the Eu^{3+} $4f$ peak ($J = 3.5$) and the Eu^{2+} $4f$ peak ($J = 6$) $\Delta E_{\mathrm{Eu}^{3+}-\mathrm{Eu}^{2+}}$, which are obtained from the observed all Eu $4f$ spectra, are summarized in Table 1.

Figure 1(b) shows the v dependence of $E_{\mathrm{B}}^{\mathrm{Eu}^{2+}}$ value at 20 K. Among three materials in the pure Eu^{2+} states, $E_{\mathrm{B}}^{\mathrm{Eu}^{2+}}$ of Eu$_{0.85}$Ca$_{0.15}$Fe$_2$As is largest, while that of EuPt$_2$ is getting close to that of EuRh$_2$Si$_2$ with $v = 2.08$. With increasing v, furthermore, $E_{\mathrm{B}}^{\mathrm{Eu}^{2+}}$ becomes smaller and approaches ~0.67 eV at v larger than 2.6. This trend suggests that the c-f hybridization becomes larger in the order of Eu$_{0.85}$Ca$_{0.15}$Fe$_2$As$_2$, EuPd$_2$ and EuPt$_2$, and that EuPt$_2$ verges to the valence fluctuation state even though EuPt$_2$ is in the pure Eu^{2+} states. For the Eu compounds in the valence fluctuation state, on the other hand, it is difficult to say that $E_{\mathrm{B}}^{\mathrm{Eu}^{2+}}$ is an index to discuss the c-f hybridization at present.

Figure 1(c) shows the v dependence of $\Delta E_{\mathrm{Eu}^{3+}-\mathrm{Eu}^{2+}}$ value for the Eu compounds in the valence fluctuation state at 20 K. $\Delta E_{\mathrm{Eu}^{3+}-\mathrm{Eu}^{2+}}$ monotonically decreases from ~6.1 to ~5.8 eV with increasing v from 2.08 to 2.92. The energy separation between the center of gravity of the Eu^{2+} and Eu^{3+} $4f$ structures is roughly given by $\varepsilon_f + U_{ff}$, where ε_f represents the energy level of the $4f$ electron and U_{ff} the averaged Coulomb interaction energy between the $4f$ electrons. That is, the observed change in $\Delta E_{\mathrm{Eu}^{3+}-\mathrm{Eu}^{2+}}$ suggests that the $\varepsilon_f + U_{ff}$ value varies through the increase of v. In order to clarify the relation between $\Delta E_{\mathrm{Eu}^{3+}-\mathrm{Eu}^{2+}}$ (or $\varepsilon_f + U_{ff}$) and the c-f hybridization, we are planning to reproduce the obtained Eu $4f$ spectra by the theoretical analysis based on the single impurity Anderson model and evaluate the physical parameters characterizing the valence states: c-f hybridization strength and charge transfer energy, and so on.
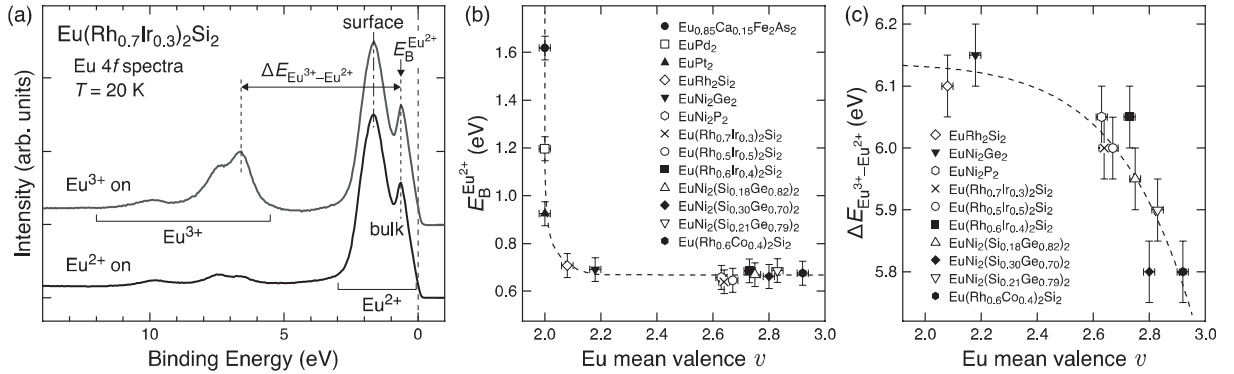

FIGURE 1. (a) Eu $4f$ spectra of Eu(Rh$_{0.7}$Ir$_{0.3}$)$_2$Si$_2$ obtained from the Eu $4d$-$4f$ REPS experiments at 20 K. These spectra were normalized by the maximum spectral intensity. (b) Relationship between the Eu mean valence v and $E_{\mathrm{B}}^{\mathrm{Eu}^{2+}}$ value at 20 K. (c) Relationship between v and $\Delta E_{\mathrm{Eu}^{3+}-\mathrm{Eu}^{2+}}$ value at 20K. Broken lines in (b) and (c) are guides to the eyes.

REFERENCES

1. C. M. Varma, *Rev. Mod. Phys.* **48**, 219-238 (1976).
2. K. Mimura, T. Uozumi, T. Ishizu, S. Motonami, H. Sato, Y. Utsumi, S. Ueda, A. Mitsuda, K. Shimada, Y. Taguchi, Y. Yamashita, H. Yoshikawa, H. Namatame, M. Taniguchi, and K. Kobayashi, *Jpn. J. Appl. Phys.* **50**, 05FD03/1-2 (2011).
3. K. Ichiki, K. Mimura et al., submitted to *Phys. Rev. B*.
4. A. Mitsuda, T. Matoba, S. Seike, F. Ishikawa, Y. Yamada, and H. Wada, *J. Phys. Soc. Jpn.* **80**, SA117/1-2 (2011).
5. A. Nakamura, H. Akamine, Y. Ashitomi, F. Honda, D. Aoki, T. Takeuchi, K. Matsubayashi, Y. Uwatoko, Y. Tatetsu, T. Maehira, M. Hedo, T. Nakama, and Y. Ōnuki, *J. Phys. Soc. Jpn.* **85**, 084705/1-7 (2016).
6. A. Mitsuda, S. Hamano, N. Araoka, H. Yayama, and H. Wada, *J. Phys. Soc. Jpn.* **81**, 023709/1-4 (2012).
7. A. Mitsuda, T. Fujimoto, E. Kishaba, S. Hamano, A. Kondo, K. Kindo, and H. Wada, *J. Phys. Soc. Jpn.* **85**, 124703/1-6 (2016).
8. S. Bud'ko, Z. Islam, T. Wiener, I. Fisher, A. Lacerda, and P. Canfield, *J. Magn. Magn. Mater.* **205**, 53-78 (1999).
9. R. Nagarajan, G. K. Shenoy, L. C. Gupta, and E. V. Sampathkumaran, *Phys. Rev. B* **32**, 2846-2850 (1985).
10. H. Wada, A. Nakamura, A. Mitsuda, M. Shiga, T. Tanaka, H. Mitamura, and T. Goto, *J. Phys.: Condens. Matter* **9**, 7913-7923 (1997).
11. H. Wada, A. Mitsuda, T. Yoshida, T. Yamamoto, and T. Tanaka, *J. Phys. Soc. Jpn.* **72**, 2604-2607 (2003).
12. E. Kishaba, S. Hamano, A. Mitsuda, A. Kondo, K. Kindo, M. Mizumaki, K. Nitta, and H. Wada, *JPS 2013 Autumn Meeting* 25aPS-146.

Valence band structure of the layered oxychalcogenides (LaO)CuCh and (BiO)CuCh (Ch = Se, Te)

K. Takase[a], K. Kanno[a], S. Ishiwata[a], K. Kawamoto[a], A. Rousuli[b], T. Nagasaki[b], S. Nakamura[c], H. Sato[d], and A. Higashiya[e], A. Yamasaki[f]

[a]College of Science and Technology, Nihon University, Chiyoda-ku, Tokyo 101-0062, Japan
[b]Graduate School of Science, Hiroshima University, Kagamiyama 1-3-1, 739-8526, Japan
[c]Faculty of Science, Hiroshima University, Kagamiyama 1-3-1, 739-8526, Japan
[d]Hiroshima Synchrotron Radiation Center, Hiroshima University, Kagamiyama 2-313, 739-0046, Japan
[e]Faculty of Science and Engineering, Setsunan University, Neyagawa, Osaka 572-8508, Japan
[f]Faculty of Science and Engineering, Konan University, Kobe 658-8501, Japan

Keywords: oxychalcogenide, photoemission, thermoelectric power.

The layered oxychalcogenide, which consists of an oxide blocking layer and a conductive chalcogenide layer stacked alternately along the *c*-axis, has been attracted much attention due to relatively large thermoelectric power and superconductivity from the low-dimensionality. In the oxychalcogenide family, bismuth system has been reported to show good performance in the thermoelectric properties [1]. Especially, (BiO)CuTe has a larger thermoelectric power than that of (BiO)CuSe. On the other hand, (LaO)CuSe and (LaO)CuTe don't show good thermoelectric properties in spite of the same crystal structures. In the both system, the difference is a kind of element; i.e. whether the metal atom of the oxide layer is La or Bi.

According to the Mott formula [2], Seebeck coefficient for semiconductors is expressed by the next equation,

$$S = \gamma \left(\frac{1}{D(\varepsilon)} \frac{dD(\varepsilon)}{d\varepsilon} + \frac{1}{f(\varepsilon)} \frac{df(\varepsilon)}{d\varepsilon} - \frac{1}{\mu(\varepsilon)} \frac{d\mu(\varepsilon)}{d\varepsilon} \right)_{\varepsilon = E_F}$$

where $D(\varepsilon)$ is a density of state, $f(\varepsilon)$ is the Fermi distribution function, $\mu(\varepsilon)$ is mobility, and $\gamma = \pi^2 k_B^2 T/3q$ with q (carrier charge), k_B (Boltzmann constant), and T (temperature). So, variation of energy dependence of density of state is expected to provide large contribution to Seebeck coefficient.

In this study, we have carried out photoemission spectroscopy against (LaO)CuSe, (La)CuTe, (BiO)CuSe, (BiO)CuTe to understand the difference of Seebeck coefficients in terms of density of state (DOS) around the Fermi energy.

Samples in this study were polycrystals prepared by solid-state reaction. Temperature dependences of the electrical resistivity were investigated using four-probe method by PPMS from room temperature to 4 K. Synchrotron photoemission spectroscopy measurements were performed at room temperature for all samples at BL7 in HISOR with photon energy ($h\nu$) between 40 eV and 200 eV. The electronic structure of each material was calculated using density functional theory.

The resistivity of (LaO)CuSe, (LaO)CuTe, (BiO)CuSe decreases with decreasing temperature. On the other hand, (BiO)CuTe has a metallic property in the entire temperature range.

Figure 1(1)~(4) shows the valence band spectra consisting of four main structures (A)~(D) with various photon energy. These shows incident $h\nu$ dependence clearly, which mean that the top of valence band composed of the Cu 3d and the Se(Te) 4p(5p) hybridized orbitals. Origin of structure D is unclear now, but this might to be due to a contribution from p orbital, considering the $h\nu$ dependence. The calculated valence bands are depicted in Figure 1 (5)~(8). These results indicate that their valence bands are constituted by the Cu 3d and the Se(Te) 4p(5p) hybridized orbitals. We should note that the calculation well describes change of the band gap qualitatively. In fact, (BiO)CuTe is a metal. In this material, a small finite DOS should be at the Fermi energy.

Figure 2 shows a schematic figure of the electronic structure. In the tetrahedral crystal field, the Cu 3d orbitals split in to the t_{2g} and the e_g orbitals. The Cu 3d and the Se(Te) 4p(5p) orbitals well hybridize and form the bonding state with lower energy and the antibonding state with higher energy, where the e_g orbital is in the

non-bonding state. From the level scheme, the observed structures of A, B, and C are assigned to the Cu 3d and the Se(Te) 4p(5p) antibonding orbitals, the Cu e_g non-bonding orbitals, and the bonding orbitals, respectively.

In summary, we have investigated the valence band structures of the layered oxypnictides (LaO)CuSe, (LaO)CuTe, (BiO)CuSe, (BiO)CuTe through photoemission spectroscopy and first-principles calculations. The top of valence bands of these materials consist of the Cu 3d and chalcogen np bonding, nonbonding, antibonding orbitals. In the Bi system, the band gap narrows, comparing with the La system. Peculiarly, (BiO)CuTe might have a small finite DOS at the Fermi energy from the metallic character of this material.
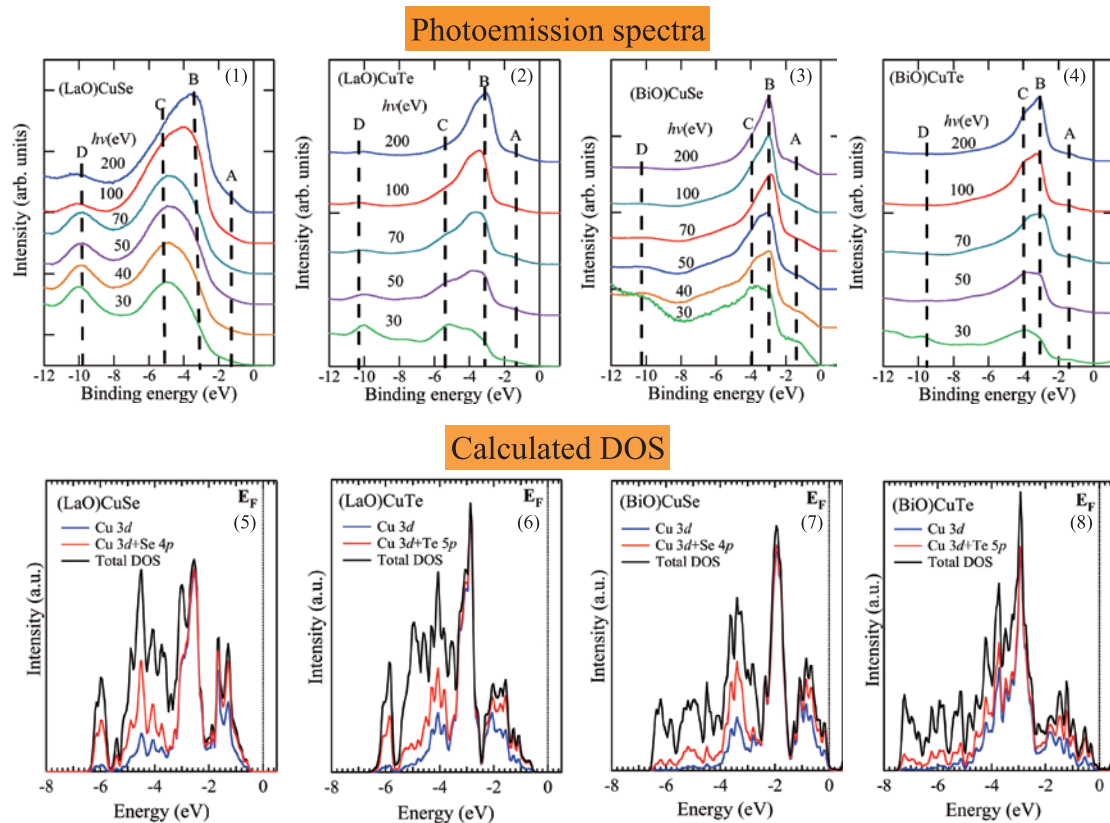

FIGURE 1. Photoemission spectra at various photon energy for (LaO)CuSe (1), (LaO)CuTe (2), (BiO)CuSe (3), (BiO)CuTe (4), and the calculated valence band structures of these samples by density function theory.
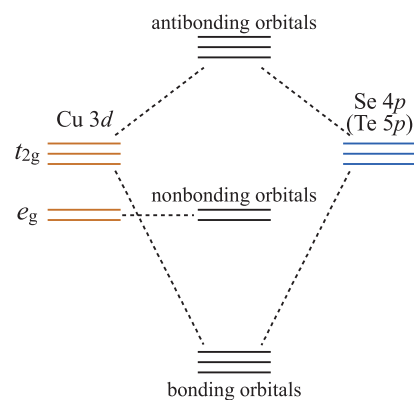

FIGURE 2. Schematic band structure of the layered oxychalcogenides (LaO)CuCh and (BiO)CuCh.

REFERENCES

1. P. Vaqueiro, G. Guelou, M. Stec, E. Guilmeau, and A. V. Powell, *J. Mater. Chem* A **1**, 520-5233 (2013).
2. J. H. Lee, J. Wu, and F. C. Grossman, *Phys. Rev. Letters* **104**, 016602 (2010).

Proving Nontrivial Topology of Pure Bismuth by Quantum Confinement

Suguru Ito[a], Baojie Feng[b], Masashi Arita[b], Akari Takayama[c], Ro-Ya Liu[a],
Takashi Someya[a], Wei-Chuan Chen[d], Takushi Iimori[a], Hirofumi Namatame[b],
Masaki Taniguchi[b], Cheng-Maw Cheng[d], Shu-Jung Tang[d, e], Fumio Komori[a],
Katsuyoshi Kobayashi[f], Tai-Chang Chiang[g], Iwao Matsuda[a]

[a]*Institute for Solid State Physics, The University of Tokyo, Kashiwa, Chiba, Japan*
[b]*Hiroshima Synchrotron Radiation Center, Hiroshima University, Higashi-Hiroshima, Hiroshima, Japan*
[c]*Department of Physics, The University of Tokyo, Bunkyo-ku, Tokyo, Japan*
[d]*National Synchrotron Radiation Research Center (NSRRC), Hsinchu, Taiwan*
[e]*Department of Physics and Astronomy, National Tsing Hua University, Hsinchu, Taiwan*
[f]*Department of Physics, Ochanomizu University, Bunkyo-ku, Tokyo, Japan*
[g]*Department of Physics and Frederick Seitz Materials Research Laboratory, University of Illinois at Urbana-Champaign, Urbana, Illinois, USA*

Keywords: bismuth, topological material, ARPES, quantum confinement

Elemental bismuth (Bi) has been providing an irreplaceable playground to study various quantum phenomena owing to its huge spin-orbit coupling and the three-dimensional Dirac-like dispersion formed in its pure single crystal. Especially the former made Bi a central element in designing topological materials, whose exotic properties have attracted great attention both from a fundamental and application point of view. However, the topology of pure Bi itself has long been controversial [1,2]. The largest obstacle in its experimental detection was the three-dimensional Dirac-like dispersion, which is so sharp against a momentum resolution expected in usual angle-resolved photoelectron spectroscopy (ARPES) that the bulk bands have never been clearly observed [1]. This is a fatal problem because the band gap of Bi is very small (~10 meV [2]) and a slight energy shift in bulk bands can easily transform a topologically nontrivial case into a trivial case. In the present study, we overcame these difficulties by systematically observing evolutions of surface and quantized bulk bands (quantum-well states, QWSs) formed inside Bi thin films with increasing thicknesses. Whereas QWSs possess information on bulk bands, they are two-dimensional states and can be precisely measured with ARPES.

The experiments were performed in HiSOR BL-9A and NSRRC BL-21B1. Photon energies of 21 eV and 8.4 eV were used. The measurement temperature was set to 10 K and the total energy resolution was estimated as 7 meV. A Ge(111) wafer was used as a substrate and cleaned by cycles of Ar^+ sputtering (1 kV) and annealing (600℃). Bi was deposited on it at room temperature with a pressure kept at a very low level (~1×10^{-8} Pa). The thickness was precisely calibrated using a quartz thickness monitor.

Figure 1 (a) shows a wide-range ARPES image measured on a 14 bilayer (BL; 1 BL = 3.9 Å) Bi(111) film along $\overline{\Gamma M}$ direction. We can clearly confirm two surface bands (SS1 and SS2) near Fermi level and QWS bands inside bulk projections. We follow their evolutions against thicknesses from 14 to 202 BL as shown in Fig. 1(b). As the thickness increases, an energy splitting between QWS levels gradually decreases and finally we succeeded in observing QWSs even at ~10 meV scale. Energy levels of QWSs can be analytically formulated considering a phase shift of confined wave functions [3]. By analyzing QWS peak positions shown in Fig. 2(a) and (b), we directly revealed hybridizations between surface and bulk electronic structures in Bi. Finally we followed the evolutions of valence band maximum (VBM) and conduction band minimum (CBM) against an inversed thickness as shown in Fig. 2(c). The solid lines were drawn based on the phase analysis and perfectly reproduced the experimental data. From the fact that VBM and CBM, hybridizing SS1 and SS2 respectively, never cross even in the bulk limit, we can unambiguously confirm that the nontrivial scenario (Fig. 2(d)) is the case. The present study not only proves the fundamental property of Bi but also introduces a powerful method to determine both surface and bulk electronic structures with the highest resolution ever.
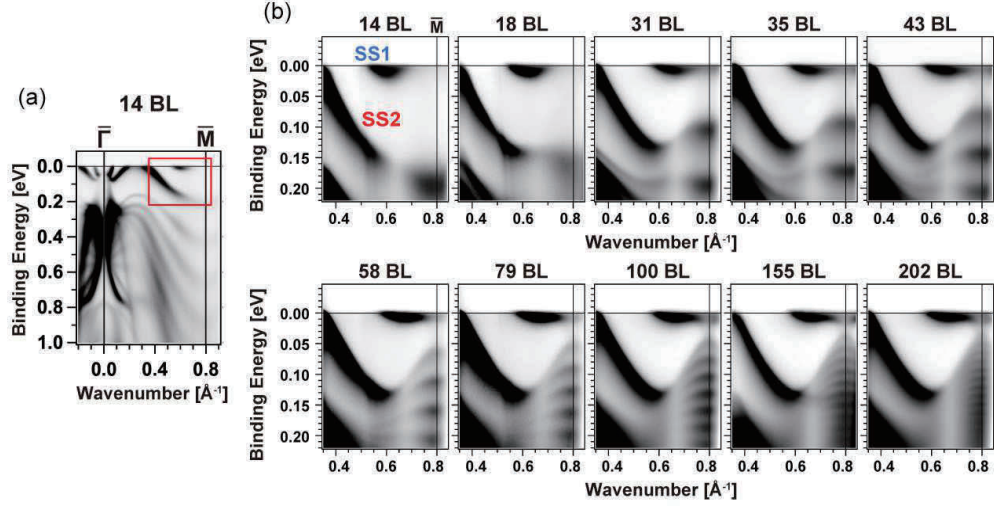
FIGURE 1. (a) A wide-range ARPES image measured on a 14 BL Bi(111) film. Two surface bands (SS1 and SS2) near Fermi level and QWS bands formed inside bulk projections are sharply observed. (b) ARPES images magnified inside a red box in (a) with the thickness systematically increased from 14 to 202 BL.
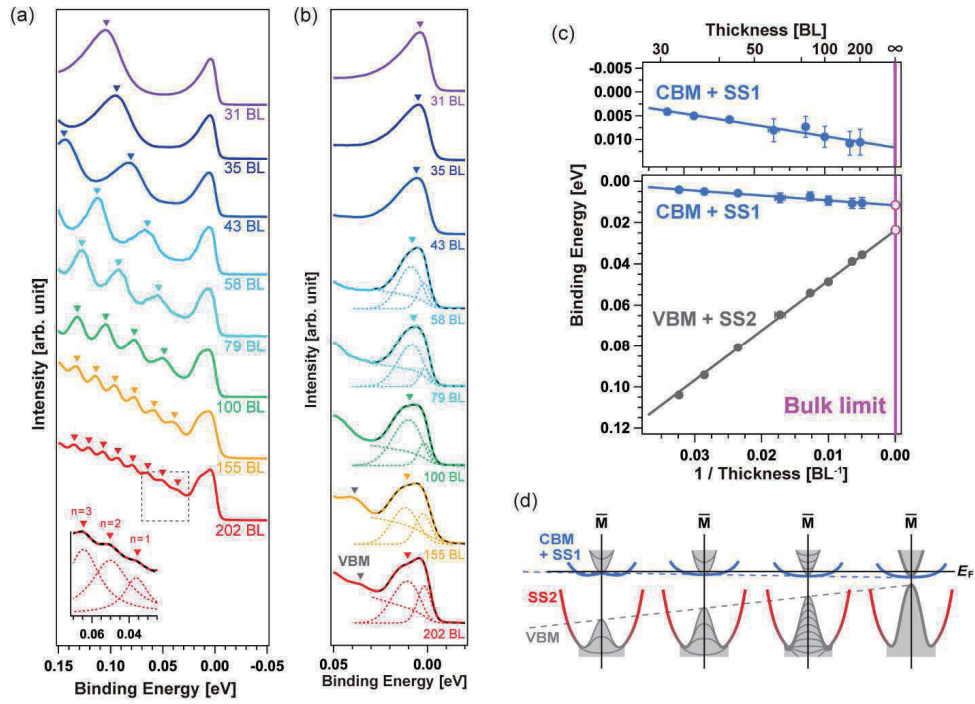

FIGURE 2. (a) Energy distribution curves (EDCs) extracted at $k = 0.8$ Å^{-1} ($\overline{M}$ point) for each thickness in Fig. 1(b). (b) EDCs magnified around Fermi level. (c) Evolutions of peak positions at CBM and VBM, hybridizing with SS1 and SS2 respectively, against an inversed thickness. Solid lines are drawn based on a QWS phase model. (d) Schematic representation of band evolutions in Bi films approaching the bulk limit.

REFERENCES

1. Y. Ohtsubo *et al.*, New Journal of Physics **15**, 033041-033051 (2013).
2. L. Aguilera *et al.*, Physical Review B **91**, 125129-125135 (2015).
3. T.-C. Chiang, Surface Science Report **39**, 181-235 (2000).
4. S. Ito *et al.*, Physical Review Letters **117**, 236402-236407 (2016).

Angle-resolved photoemission study of hybridization gap in the ternary rare-earth compound EuPtP

H. Anzai[a], K. Ichiki[a], Eike F. Schwier[b], H. Iwasawa[b], M. Arita[b], H. Sato[b], K. Shimada[b], H. Namatame[b], M. Taniguchi[b], A. Mitsuda[c], H. Wada[c], H. Ikeda[d], and K. Mimura[a,b]

[a] *Graduate School of Engineering, Osaka Prefecture University, Sakai 599-8531, Japan*
[b] *Hiroshima Synchrotron Radiation Center, Hiroshima University, Higashi-Hiroshima 739-0046, Japan*
[c] *Department of Physics, Graduate School of Science, Kyushu University, Fukuoka 819-0395, Japan*
[d] *Department of Physics, Ritsumeikan University, Kusatsu Shiga 525-8577, Japan*

Keywords: Electronic structure, Eu compound, angle-resolved photoemission spectroscopy.

The ternary rare-earth compound EuPtP shows two first-order valence transitions at $T_1 = 235$ K and $T_2 = 190$ K [1,2]. The mean Eu valence is estimated to be 2.16 ($T > T_1$), 2.30 ($T_2 < T < T_1$), and 2.40 ($T < T_2$) from X-ray absorption and Mössbauer spectroscopy measurements [1,2]. The temperature dependence of the resistivity is anomalous and anisotropic with $\rho_{ab} << \rho_c$ at all temperature. The c-axis resistivity increases at $T_2 < T < T_1$ and approaches the limit of metallic conduction [3]. These unique physical properties in EuPtP provide a good opportunity to understand the origin of the valence transition and its influence on the electronic structure.

Angle-resolved photoemission spectroscopy (ARPES) has played a leading role in the investigating the electronic state. In a previous ARPES study of heavy-fermion compound $EuNi_2P_2$, an energy gap due to hybridization between the Ni 3d and Eu 4f states was observed near the Fermi level (E_F) [4]. Here, we report ARPES studies of EuPtP that reveal the hybridization phenomena below T_2. The ARPES measurements were performed at BL-9A of Hiroshima Synchrotron Radiation Center. Total instrumental energy resolutions were set to 15 meV. The samples were cleaved *in situ* and kept under ultrahigh vacuum better than 5 x 10^{-11} Torr.

Figures 1(a) shows the ARPES spectra taken at 140 K along a momentum cut slightly off the $\overline{\Gamma}-\overline{K}$ direction. The photoemission intensity was normalized by the angle-integrated spectrum. A flat band is visible at $|\omega| \sim 0.9$ eV and is assigned to the bulk Eu^{2+} 4f state [5,6]. A highly dispersive band centered at $|k| \sim 0$ Å^{-1} appears over an energy range of $0.9 < |\omega| < 1.5$ eV and approaches the bulk Eu^{2+} 4f state, as shown in Fig. 1(a). This band originates from the Pt 5d states because the density of states near E_F is dominated by the Pt 5d states except for the localized Eu 4f states [7,8].

The Pt 5d band exhibits a discontinuity at the crossing point with the bulk Eu 4f state. The peak positions of the momentum distribution curves (MDCs) in Fig. 1(b) shift abruptly around $|\omega| \sim 0.8$ eV. A discontinuity in the conduction bands have been observed in SmB_6 and assigned to hybridization phenomena [9]. This similarity implies that the Pt 5d state hybridizes with the localized Eu 4f states.

Figure 1(c) shows the energy distribution curves (EDCs) at $0 < k < 0.8$ Å^{-1}. Three peaks, assigned as δ, ζ, and η bands, were observed in the EDC at $k \sim 0.8$ Å^{-1}. When approaching $k \sim 0$ Å^{-1}, the δ band shifts downward from E_F to $|\omega| \sim 0.8$ eV and possibly overlaps with the ζ band. On the other hand, the peak positions of the η band are well separated from those of the δ and ζ band. The band dispersions obtained from the results in the MDCs and EDCs are shown in Fig. 1(d). We found that the η band connects smoothly with the Pt 5d band and forms a gap-like structure with the δ band.

To quantitatively analyze the band dispersion, we fitted the band points using the periodic Anderson model. In this model, two energy branches (E_k^+ and E_k^-) due to c-f hybridization are described by the forms,

$$E_k^{\pm} = \frac{1}{2}\left\{ \varepsilon_f + \varepsilon_c \pm \sqrt{(\varepsilon_f - \varepsilon_c)^2 + 4V_k^2} \right\},\tag{1}$$

where ε_c and ε_f are the conduction-band and f-band energies, respectively. The gap size in momentum space is described the hybridization energy $2V_k$, as schematically shown in the inset of Fig. 1(d). In the fitting procedure,

we excluded the energy points of the ζ band. Moreover, the hybridization energy V_k is approximated by the momentum-independent parameter ($V_k = V_{eff}$) for simplicity. The fitting results are overlaid as black curves in Fig. 1(d). The simulation reproduces well the lower and upper energy branches with the hybridization energy of $V_{eff} \sim 0.1$ eV. This indicates the hybridization between the Eu $4f$ and the Pt $5d$ electrons in EuPtP below T_2.

In summary, we have revealed the electronic structure near E_F of EuPtP from the ARPES measurements. We observed that the dispersive Pt $5d$ band approaches the bulk Eu^{2+} $4f$ state. From the intensity-normalized ARPES spectra, we demonstrated the existence of an energy gap at the crossing point of these two bands. The observed band dispersions were reproduced well by the periodic Anderson model with the hybridization energy of $V_{eff} \sim 0.1$ eV. Our results suggest that the c-f hybridization effect is likely to play an important role of the valence transition in EuPtP.
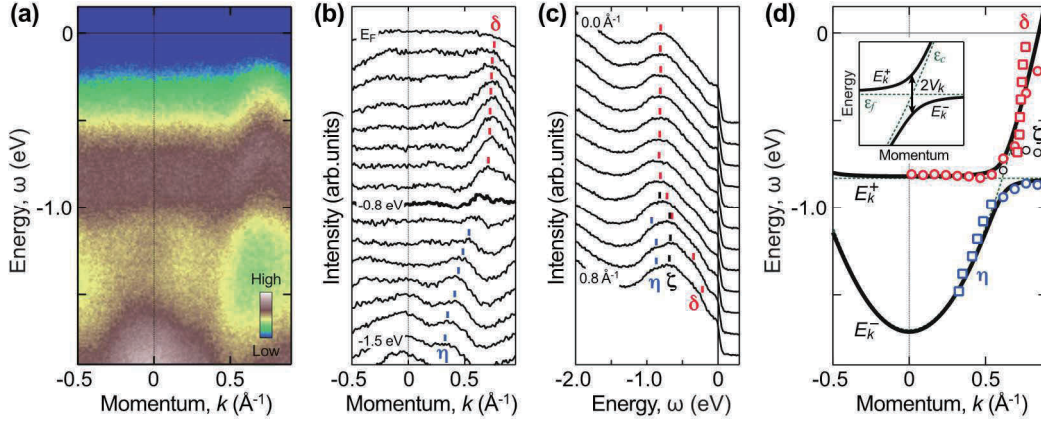

Figure 1 (a) ARPES spectra of EuPtP taken at 140 K with $h\nu = 34$ eV. The photoemission intensity of each EDC is normalized by the angle-integrated ARPES spectrum. (b), (c) The corresponding MDCs and EDCs of (a), respectively. Vertical bars indicate the peak positions. (d) Summary of the experimental band structure. Open squares and circles denote the peak positions of the MDCs and EDCs, respectively. Solid curves indicate the hybridized-band dispersion predicted by periodic Anderson Model. The green dotted lines represent the conduction-band ε_c and f-band energies ε_f. The inset shows a schematic diagram of the hybridized-band dispersions under the periodic Anderson model.

REFERENCES

1. N. Lossau *et al.*, Z. Phys. B **74**, 227 (1989).
2. N. Lossau *et al.*, Z. Phys. B **77**, 393 (1989).
3. A. Nowack *et al.*, Z. Phys. B **77**, 381 (1989).
4. S. Danzenbächer *et al.*, Phys. Rev. Lett. **102**, 026403 (2009).
5. E.-J. Cho *et al.*, J. Electron Spectrosc. Relat. Phenom. **77**, 173 (1996).
6. P. A. Rayjada *et al.*, Phys. Rev. B **70**, 235105 (2004).
7. P. Strasser *et al.*, Nat. Chem. **2**, 454 (2010).
8. Y. Cui *et al.*, J. Phys. Chem. C **120**, 10936 (2016).
9. E. Frantzeskakis *et al.*, Phys. Rev. X **3**, 041024 (2013).

Low-energy Angle-Resolved Photoemission Study of Bi$_{2.1}$Sr$_{1.9}$Ca(Cu$_{1-x}$Ni$_x$)$_2$O$_{8+\delta}$ (x = 0, 0.01, 0.03)

W. Mansuer[a], N. Kishimoto[a], H. Takita[a], T. Kubo[a], M. Arita[b], H. Namatame[b], M. Taniguchi[a,b], Y. Kiguchi[c], T. Sakaidani[c], A. Matsuda[c], A. Ino[a]

[a]Graduate School of Science, Hiroshima University, Higashi-Hiroshima 739-8526, Japan
[b]Hiroshima Synchrotron Radiation Center, Hiroshima University, Higashi-Hiroshima 739-8526, Japan
[c]Department of Physics, Schools of Advanced Science and Engineering, Waseda University, Okubo 3-4-1, Shinjuku, Tokyo 160-8555, Japan

Keywords: angle-resolved photoemission, high-T_c cuprates, superconducting gap, element substitution.

Superconducting transition occurs, when electron pairs are formed in solid. The energy for taking an electron apart from the coherent pairs is directly observed as an energy gap by using photoemission spectroscopy. Thus, unusual behavior of the energy gap provides a clue to understanding the mechanism of the high-critical-temperature (high-T_c) superconductivity. The common structure of the high-T_c cuprate superconductors is a two-dimensional CuO$_2$ plane, where the hybridization of copper $d_{x^2-y^2}$ orbital and oxygen p_x/p_y orbital forms the low-energy electronic band responsible for the superconductivity. Replacing small amount of Cu with another transition-metal element, one can introduce impurities right on the CuO$_2$ planes, namely the stage of high-T_c superconductivity, and consequently reduce the maximum critical temperature T_c^{max}. This provides us with a good opportunity to investigate the relation between the energy gap and the high-T_c superconductivity.

In this study, we performed high-resolution angle-resolved photoemission spectroscopy (ARPES) of Ni-substituted Bi2212 superconductors, Bi$_{2.1}$Sr$_{1.9}$Ca(Cu$_{1-x}$Ni$_x$)$_2$O$_{8+\delta}$ [1]. The ARPES spectra were taken at BL-9A of HiSOR in Hiroshima Synchrotron Radiation Center. Excitation-photon energy and energy resolution were set at $h\nu$ = 8.5 eV and ΔE = 5 meV, respectively. The critical temperatures of the samples of x = 0, 0.01 and 0.03 are T_c = 90, 85 and 70 K, respectively.
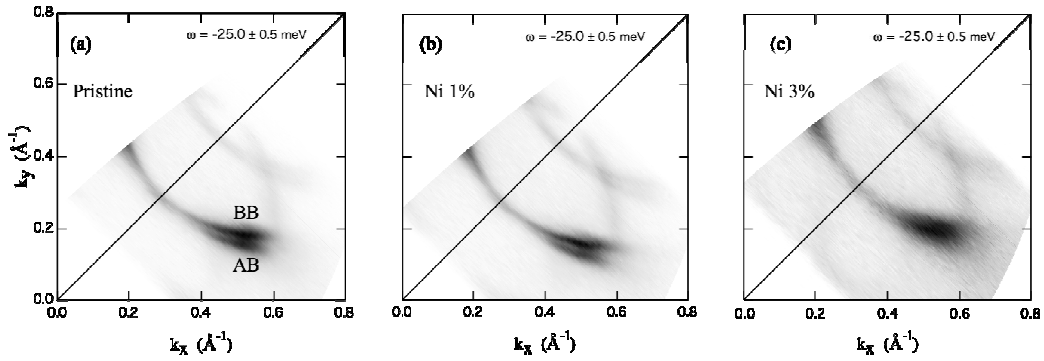

FIGURE 1. (a) Momentum space mapping for pristine Bi2212. The primary bonding band and anti-bonding band are referred to as BB and AB, respectively. (b) Momentum space mapping for 1% Ni substituted Bi2212. (c) Momentum space mapping for 3% Ni substituted Bi2212.

Overview of our ARPES intensity data for Bi$_2$Sr$_2$Ca(Cu$_{1-x}$Ni$_x$)$_2$O$_{8+\delta}$, x = 0, 0.01, 0.03 is shown in Fig. 1. In the superconducting state, we observed the clear bilayer-band splitting despite 1% Ni substitution, indicating the high quality of the samples. However, bilayer-band splitting is not resolved for 3% Ni substituted sample, probably because of the impurity scattering. Finite spectral intensity around node is due to the intrinsic lifetime broadening and experimental resolution.
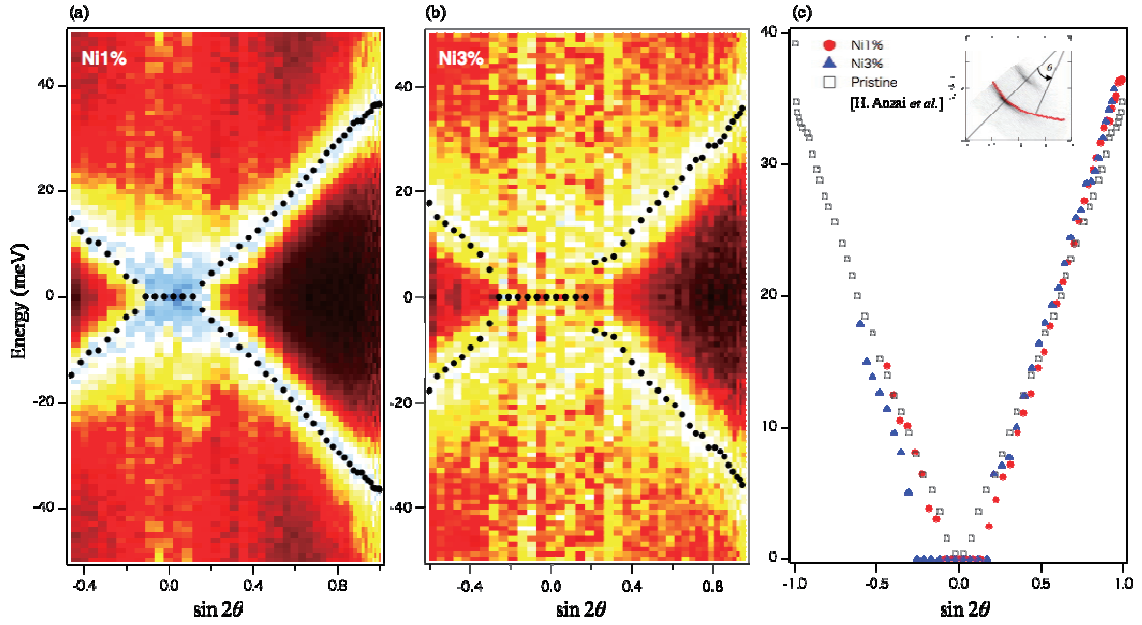
FIGURE 2. (a) Energy gap as a function of Fermi angle θ for 1% Ni substituted Bi2212. (b) Energy gap as a function of Fermi angle θ for 3% Ni substituted Bi2212. (c) Energy gap comparison between pristine [2], 1% Ni substituted and 3% Ni substituted Bi2212 as a function of Fermi angle θ.

As shown in Fig. 2(a) and Fig. 2(b), superconducting gap opens along the off-nodal direction for both 1% and 3% Ni substituted Bi2212 samples. This indicates the general directional dependence of the superconducting gap in cuprate superconductors. However, superconducting gap remain unresolved around nodal region probably because of the energy resolution. As shown in Fig. 2(c), there is no significant change in gap size even though the critical temperature decreases with a quite large step. This result, which is in contrast with our prediction, indicates that impurity doping do not affect the binding energy between the two electrons of a Cooper pair.

REFERENCES

1. Y. Kiguchi, T. Nakazawa and A. Matsuda, *Phys. Procedia* **58**, 54-57 (2014).
2. H. Anzai *et al.*, *Nat. Commun.* **4**, 1815 (2013).

Experimental Realization of Two-Dimensional Dirac Nodal Line Fermions

Baojie Feng[a,b], Suguru Ito[a], Masashi Arita[b] and Iwao Matsuda[a]

[a]*Institute for Solid State Physics, The University of Tokyo, Kashiwa, Chiba 277-8581, Japan*
[b]*Hiroshima Synchrotron Radiation Center, Hiroshima University, 2-313 Kagamiyama, Higashi-Hiroshima 739-0046, Japan*

Topological nodal line semimetals, a novel quantum state of materials, possess topologically nontrivial valence and conduction bands that touch at a line near the Fermi level. The exotic band structure can lead to various novel properties, such as long-range Coulomb interaction and flat Landau levels. Recently, topological nodal lines have been observed in several bulk materials, such as $PtSn_4$, $ZrSiS$, $TlTaSe_2$ and $PbTaSe_2$. However, in two-dimensional materials, experimental research on nodal line fermions is still lacking. Here, we report the discovery of two-dimensional Dirac nodal line fermions in monolayer Cu_2Si based on combined theoretical calculations and angle-resolved photoemission spectroscopy (ARPES) measurements. The Dirac nodal lines in Cu_2Si form two concentric loops centred around the Γ point and are protected by mirror reflection symmetry. Our results establish Cu_2Si as a new platform to study the novel physical properties in two-dimensional Dirac materials and provide new opportunities to realize high-speed low-dissipation devices.
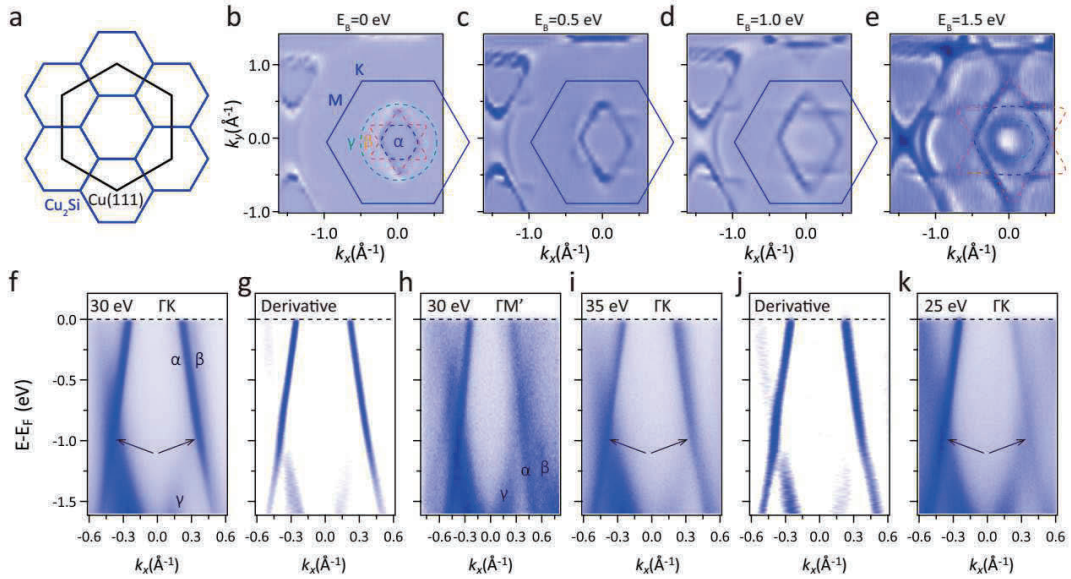
Figure 1. ARPES results for monolayer Cu_2Si on Cu(111). (a) Schematic drawing of the Brillouin zones of Cu_2Si (blue hexagons) and Cu(111) (black hexagon). As the lattice of Cu_2Si is $(\sqrt{3} \times \sqrt{3})R30°$ with respect to the Cu(111)-1×1 lattice, the K point of Cu(111) is located at the Γ point of the second Brillouin zone of Cu_2Si. (b-e) Second derivative CECs measured using 30-eV photons. Three closed contours have been observed: a hexagon, a hexagram, and a circle, as indicated by the dashed lines. (f,i,k) ARPES intensity plots along the Γ-K direction with different photon energies: 30 eV, 35 eV, and 25 eV, respectively. The black arrows mark the position of the crossing points. (g,j) Second derivative ARPES intensity plots of (f) and (i), respectively. (h) ARPES intensity plots parallel to the Γ-K direction. There is a 2° offset from the Γ-M axis.

Monolayer Cu_2Si forms a $(\sqrt{3}\times\sqrt{3})R30°$ superstructure with respect to the Cu(111)-1×1 lattice. A schematic drawing of the Brillouin zones of Cu_2Si and Cu(111) is shown in Fig. 1(a). In Figs. 1(b)-1(e), we show the evolution of constant energy contours (CECs) with binding energies. Several pockets centred at the Γ point can

be seen: one hexagon, one hexagram, and one circle. Because of the matrix element effects, the ARPES intensities are anisotropic, resulting in a rhombic shape at the Fermi level. The hexagon, hexagram and circle become clearer at higher binding energies. These bands agree well with bands α, β, and γ from our calculations [Fig. 1(e) in Ref. 1]. With increasing binding energies, the sizes of the hexagon and hexagram increase, while the size of the circle decreases. In particular, the circle is larger than the hexagon and hexagram at the Fermi level and becomes smaller at binding energies higher than 1.0 eV, indicating the existence of two gapless or gapped nodal loops centred at the Γ point.

In Figs. 1(f) and 1(g), we show the ARPES intensity plots measured along the Γ-K direction. The band crossings, i.e., the nodal lines, are clearly observed at both sides of the Γ point (indicated by the black arrows), in agreement with the evolution of the CECs from Figs. 1(b)-1(e). The band crossing is located at deeper binding energy compared with the freestanding Cu_2Si [Fig. 1(b) in Ref. 1], which might originate from the electron doping of the metallic Cu(111) substrate. Furthermore, linear dispersion is observed near the nodal lines, in agreement with our theoretical calculation results. These results show that the quasiparticles in Cu_2Si are Dirac nodal line fermions. Because of the small separation of α and β bands along the Γ-K direction, the two bands are not clearly resolved in Fig. 1(f). The two bands are well resolved along the cut parallel to the Γ-M direction, as shown in Fig. 1(h).

REFERENCES

1. B. Feng, B. Fu, S. Kasamatsu, S. Ito, P. Cheng, C.-C. Liu, S. K. Mahatha, P. Sheverdyaeva, P. Paolo, M. Arita, O. Sugino, T. -C. Chiang, K. Wu, L. Chen, Y. Yao, I. Matsuda. arXiv:1611.09578 (2016).